Physical Models and Natural Examples of Fold Interference

by

Mary Katherine Johns, B.A., M.S.

Dissertation

Presented to the Faculty of the Graduate School of

The University of Texas at Austin

in Partial Fulfillment

of the Requirements

for the Degree of

Doctor of Philosophy

The University of Texas at Austin

August, 1995

Physical Models and Natural Examples of Fold Interference

Approved by
Dissertation Committee:

[redacted]
Sharon Mosher, Supervisor

[redacted]
William D. Carlson

[redacted]
Mark P. Cloos

[redacted]
Peter Hudleston

[redacted]
Martin P. Jackson

Acknowledgements

A number of people have influenced the development of ideas and techniques presented in this manuscript. I thank Sharon Mosher for her guidance throughout this project. I thank Bruno Vendeville and Martin Jackson for their instruction in the techniques of physical modeling and for many helpful discussions during the study. Mark Cloos, Peter Hudleston, and Bill Carlson composed the remainder of a supportive committee. Bob Krantz and Walt Ring of ARCO taught me to use the CT scanner, and Kris Meisling encouraged me to use it for my research. Pat Dickerson provided helpful comments as a student editor. Peter Cobbold sparked my interest in physical modeling.

The hydraulic ram (Ch. 2) was designed by Martin Jackson. Bruno Vendeville helped design the coeval shortening set-up for the centrifuge (Ch. 3). Eddie Wheeler, Bruno Vendeville, and Sharon Mosher contributed to the design of the 1G deformation rig (Appendix 2). Randy Marrett suggested the eigenvector analysis (Ch. 3). David Stevens and Joe Jarworski gave helpful advice and produced beautiful photographs. R. Allmendinger provided gratis use of the software *Stereonet* and National Institute of Health provided gratis use of the software *NIH Image*, which I used as a digitizer.

I am grateful to the many sources that funded the project. The modeling was carried out at the Applied Geodynamics Lab, Bureau of Economic Geology, University of Texas, which graciously allowed me use of its equipment, modeling materials, and photographic supplies. ARCO Exploration and Production Technology provided use of their CT X-ray scanner and associated imaging software. Phil Bennett allowed liberal use of his computer, Muon. Additional support was provided by the University of Texas Geology Foundation, the Geological Society of America, the Sigma Xi Foundation, a University of Texas Fellowship, numerous teaching assistantships from the Department of Geological Sciences, a research assistantship with the Tight Gas Project (Bureau of Economic Geology), and a timely fellowship and warm reception from the American Association of University Women.

Thanks to Eric Beam for sharing so much laughter over the years.

Physical Models and Natural Examples of Fold Interference

Publication No._____

Mary Katherine Johns, Ph.D.

The University of Texas at Austin, 1995

Supervisor: Sharon Mosher

Fold interference is used to identify areas of polyphase deformation and to evaluate their deformation history. In this study, dynamically scaled physical models were shortened in two orthogonal directions in a centrifuge to test the effects of material properties and deformation history on the style of fold interference.

Models shortened sequentially demonstrate that rheological contrast strongly controlled the interference style. Models with low competence contrast layering had circular to elliptical interference patterns. In addition to folding, the models accommodated strain by significant layer-parallel shortening. Models with high competence contrast layering had folded early hingelines and axial surfaces. In plan view, the second-generation folds were lobate-cuspate to box-style, and the axial traces of the box folds formed conjugate pairs.

Models shortened coevally had distinct structural styles from the sequentially shortened models, as illustrated by serial Computed Tomographic (CT) X-ray scans. High competence contrast models were dominated by irregular elliptical to crescent map-shapes in the center of the models. Near the model edges, folds had straight hingelines, parallel to the boundaries. Coevally shortened models faulted and fractured less commonly than did the sequentially shortened models. Although some of the structures resembled superposed folds, the regionally inconsistent fold orientations and overprinting relationships, as well as the predominance of dome-and-basin over crescent-style interference differentiated coeval from sequential fold interference.

For both deformation histories, gravitational body forces effectively damped the vertical amplification of folds, thereby accentuating the change in fold style with depth.

Comparison of results from these models with regional-scale natural examples demonstrates that buckle-fold interference occurs in a wide range of rock types and tectonic settings. Comparison of the sequentially shortened, high competence contrast models with the Narragansett Basin, Rhode Island, suggests an alternative tectonic model for its third phase (D3) of Alleghenian deformation. According to previous tectonic models, D3 sinistral shear produced both E-W trending folds and sinistral kinematic indicators. I propose that the same features could be caused by N-S shortening, which is locally partitioned into a NE-trending megakink band.

Table of Contents

Chapter 1. Introduction

Fold interference is a common and visually striking structural style in orogenic belts. It characterizes the metamorphic cores of those orogenic belts that have undergone numerous pulses of deformation. It also occurs at lower metamorphic grades and in the foreland regions of orogenic belts, where different deformation mechanisms and structural styles are prevalent. Fold interference is used to identify areas of polydeformation and to interpret their kinematic history. Because the geometry of fold interference depends on the rheology of the rocks deformed as well as their deformation history, such interpretation can be ambiguous.

In this study, physical models are used to test directly the effect of gravitational body forces, competence contrast, degree of shortening and deformation history on the style of fold interference. Models are dynamically scaled to represent structures with wavelengths of approximately 1 km. Accordingly, the models are analyzed using the techniques of the field geologist and are compared to regional field examples in a variety of geologic settings. Results from the models and results from field work are combined to offer a new interpretation of part of the tectonic history of the Narragansett Basin, RI.

Chapter 2. Physical Models of Fold Superposition

INTRODUCTION

Fold interference patterns are used to identify areas of polyphase deformation and to evaluate their kinematic evolution. The geometry of fold superposition has been characterized as Type 1, 2, or 3, based on the angle between the first fold axial surface and the superposed displacements (Ramsay 1962, 1967 p. 521). Field analyses and computer simulations of interference patterns have concentrated on similar folds, the fold style characteristic of layering with little competence-contrast (Ramsay 1962, 1967 p.422, Thiessen & Means 1980, Thiessen 1986, Perrin *et al.* 1988, Watkinson & Thiessen 1988). Such interference patterns have been reproduced in card-deck experiments where passive line markers were deformed by heterogeneous simple shear (O'Driscoll 1962, 1964) and in plasticine models (Reynolds & Holmes 1954).

Folds are also superposed in rocks with mechanically active layering, where there is significant competence-contrast and buckling is the important fold mechanism (Hudleston 1973, Julivert & Marcos 1973, Julivert 1986, Stewart 1987, Stauffer 1988, Fowler 1989, Schwerdtner & van Berkel 1991, Stewart 1993). The interference style of superposed buckle folds is distinct from that of superposed passive folds.

Geometrical analyses assuming deformation by isometric bending (i.e. folding without thickness changes) predict that a competent layer cannot refold as a simple dome or basin structure (Lisle *et al.* 1990). Instead, crenulations with axes

oblique to the major fold trends, termed curvature-accommodation folds, are necessary to accommodate the polyphase buckling of a competent layer. The curvature-accommodation folds produce closed interference map patterns with multiple inflections of curvature. Stauffer (1988) has mapped such structures in the field.

Experimental studies have demonstrated that superposed buckling of single layers or of multilayers with high competence-contrast produces distinctive structural styles, fold mechanisms, and strain accommodation (Ghosh & Ramberg 1968, Ghosh 1974, Skjernaa 1975, Watkinson 1981, Raj 1984, Dubey 1984, Odonne & Vialon 1987, Ghosh *et al.* 1992, 1993, Grujic 1993), as recently summarized by Grujic (1993).

In this study multilayers with either negligible or significant (approximately two orders of magnitude) competence-contrast were shortened sequentially in two orthogonal directions. The models were designed to compare the interference formed by non-coaxial, superposed folds that formed under the same boundary and deformation conditions, for materials of different rheologic contrasts. Unlike some previous experiments where the first generation folds were pre-formed (e.g. Watkinson 1981, Ghosh *et al.* 1992, 1993, Grujic 1993), in this study folds of both generations formed experimentally. In this manner, we test the effect of F_1 fold heterogeneities on F_2 style and contrast the fold styles of both generations. To test the effect of gravitational body forces on the structural style of both generations of folds, models were deformed in a centrifuge. Previous models of superposed buckle folds had gravitational body forces that were insignificant with respect to lateral surface forces and are thus comparable to natural folds with wavelengths less

than about 200 m (Ramberg 1967 p.75). In this study, physical models deformed in a centrifuge are analogs of km-scale fold interference. Accordingly, models were analyzed using methods common to the field geologist. Models were analyzed by comparing the models' surface structures and horizontal sections, representing map views, fold axial traces, structure contours, and the orientation of layering and fold axes.

METHODS

Stratigraphy

Laminates with negligible competence-contrast are represented by differently colored layers of a single material. Laminates were made of relatively incompetent silicone bouncing-putty (Dow Corning dilatant compound #3179, abbreviated hereafter as DC), relatively strong Harbutt's Plasticine modeling clay (PL), or a homogeneous mixture of equal parts of the two. Both the modeling clay and silicone putty are power-law visco-elastic materials, and the modeling clay has an effective viscosity of approximately two orders of magnitude times that of the silicone putty under the experimental conditions in this study (Table 2.1, Table 2.2, McClay 1976, Dixon & Summers 1985, Weijermars 1986). Layers were stacked and rolled together. Although no obvious rheologic contrast existed between the layers, a layer-parallel, planar anisotropy may have been induced by rolling and by trapping air bubbles between the layers. The base of each model was a 1 mm layer of DC, which acted as a weak detachment layer, except where the laminate was itself entirely DC (models c223 and c226). The PL laminate (models c215)

Table 2.1 Centrifuge run time

Exp#	time (minutes)			rpm max	gmax
	D1	D2	total		
c223	28.58	28.67	57.25	2000	940
c226	26.87	28.69	55.56	2000	940
c215	5.51	40.10	45.62	2000	940
c224	37.67	15.06	52.73	2000	940
c216	12.00	18.24	30.24	2000	940
c222	42.08	31.61	73.69	2000	940
c218	52.68	55.95	108.64	2000	940
c217	33.18	61.10	94.28	2000	940
c220	27.54	62.63	90.17	2000	940
c221	32.54	95.03	127.57	2000	940
c213	6.51	13.03	19.54	2000	940

comprised 16 layers, with a total thickness of 4 mm. The laminates of DC or the DC-PL mixture comprised 12 layers, with a total thickness of 3 mm.

Laminates with significant competence-contrast were represented by alternating layers of DC and PL. The layers were stacked and quickly rolled together to form multiple, uniform thickness layers, using the microlaminate technique described by Dixon & Summers (1985). Air bubbles trapped in stacking may have served as perturbations that initiated buckling. Each model comprised a 12 or 16 layer multilaminate of total thickness 3 mm, over a 1 mm DC basal detachment.

A square grid with 5 mm spacing and grid lines parallel to the shortening directions was printed (using the photocopier technique of Dixon & Summers 1985) on the top surface of all the models before deformation. To reduce boundary effects, the base and vertical faces of all models were lubricated (National Wax Co., Paxwax 6364-1A) before deformation.

Deformation

Models were deformed in a 12 cm by 12 cm cavity in a digitally controlled centrifuge with a 21 cm radius. All models were deformed at 25°C at maximum angular velocity of 2000 rpm, equivalent to a centrifugal acceleration 940 times normal gravitational acceleration. The time between the starting and stopping of the centrifuge rotor was clocked with a stop watch. Because the rate of change of angular velocity is a known, reproducible function, the total time each model deformed under steady-state rotation can be computed and compared (Table 2.1).

During deformation the model layering was parallel to the centrifuge walls, so that the centrifugal acceleration was directed normal to the layering (Fig. 2.1a).

Shortening was driven by a polyethylene ram with a stainless steel base that was designed by M.P.A. Jackson, Applied Geodynamics Lab, Bureau of Economic Geology, University of Texas (Fig. 2.1). The ram was displaced by a spreading reservoir of dense putty (ρ = 1880 kgm^{-3}), a technique based on the spreading wedge of putty shown in Dixon & Summers (1985). The shortening rate depends on the hydraulic head of putty in the reservoir and on the angular velocity. Shortening typically began before the centrifuge reached a steady-state rotation rate. The shortening rate decreased with additional time in the centrifuge, as the hydraulic head diminished. Negligible shortening occurred as the centrifuge decelerated to a stop. No relaxation of the structures occurred following their deformation in the centrifuge. The reservoir was filled with either a dense silicone putty or a homogeneous mixture of 50% dense silicone putty and 50% Plasticine, which spread more slowly. The centrifuge was periodically stopped, at approximately 5 minute intervals, to photograph intermediate stages of deformation and to refill the reservoir.

Superposed shortening was achieved by using two hydraulic rams (Fig. 2.1b). The rams had different basal curvatures to allow sliding in different directions over the curved base of the model. The model was first shortened (D_1) parallel to the centrifuge axis by a ram with a curved base. The model was then carefully extracted from the centrifuge. The model was trimmed as it rested on a base with curvature equal to that of the equipotential surface. The first ram was removed and replaced by a smaller, flat-based ram, positioned perpendicular to the

Figure 2.1. Schematic setup of deformation apparatus used in the centrifuge. For all models, layering is parallel to the centrifuge's equipotential surface. (a) The centrifuge's rotation axis is normal to the page. The centrifugal acceleration (g) causes dense putty to spread and displace a plastic ram. (b) The centrifuge's rotation axis is parallel to the page. After D_1, a strip of undeformed laminate was inserted to fill space in the centrifuge cavity. For plan views in the following figures, the D_2 shortening direction is oriented north.

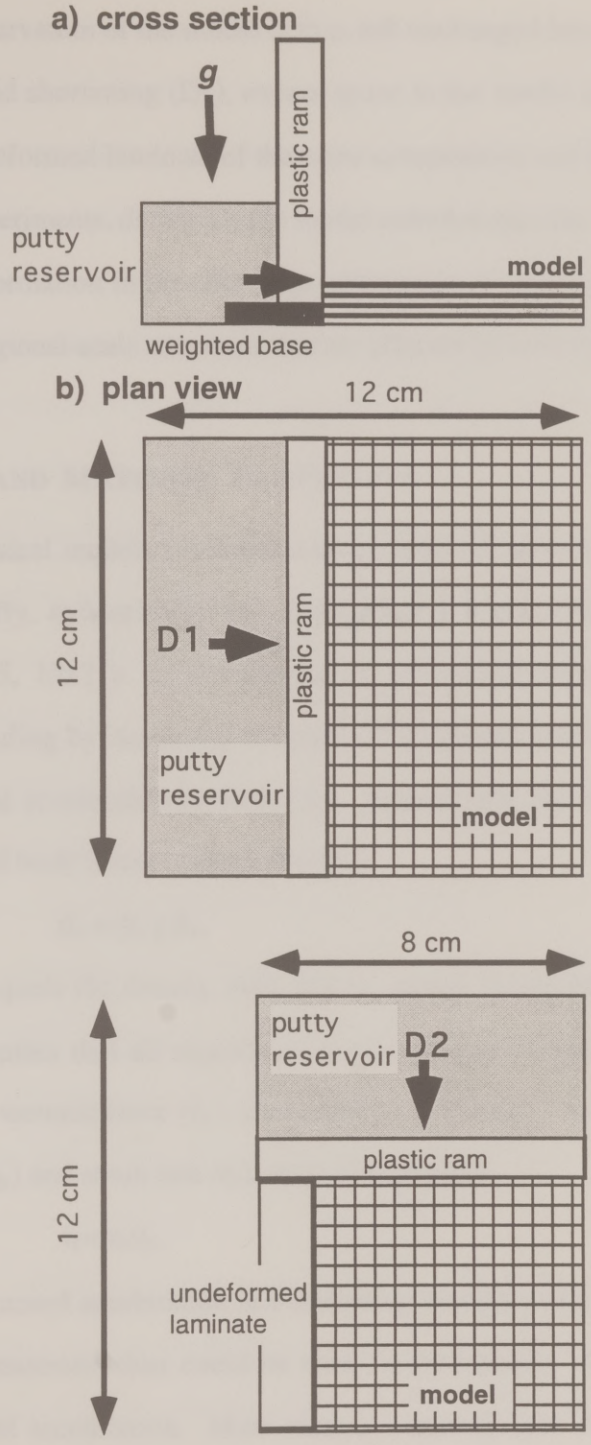
a) cross section
g
plastic ram
putty
reservoir
model
weighted base
b) plan view
12 cm
12 cm
D1
plastic ram
putty
reservoir
model
8 cm
putty
reservoir
D2
plastic ram
12 cm
undeformed
laminate
model

first. The curvature of the model is thus left unchanged between D_1 and D_2. Prior to the second shortening (D_2), excess space in the model cavity was filled with a strip of undeformed laminate of the same composition and thickness as the model. In some experiments, during D_2 the model extruded into this inserted laminate.

Deformation in the centrifuge allows use of relatively viscous materials to represent regional-scale structures that are affected by both tectonic and gravitational forces.

Scaling and Material Properties

Physical models are reasonable analogs of natural phenomena if they are geometrically, dynamically, and rheologically scaled (Hubbert 1937, Ramberg 1967 p. 2-5, 1981 p. 2, Weijermars & Schmeling 1986). A centrifuge aids dynamic scaling by increasing the ratio of centrifugal acceleration in the model to gravitational acceleration in nature (g). Accordingly, the model-to-nature ratio of gravitational body forces (σ_r) is increased:

$$\sigma_r = \rho_r \, g \, h_r, \qquad (2.1)$$

where ρ_r equals the density ratio and h_r equals length ratio. Because dynamic scaling requires that all significant forces are proportional, the ratio of surface resistive or tectonic force (τ_r), controlled by the model-to-nature ratios of effective viscosity (η_r) and strain rate (ε_r), must also increase.

$$\tau_r = \varepsilon_r \eta_r, \qquad (2.2)$$

Increased acceleration in a centrifuge therefore allows use of more viscous modeling materials than could be used in dynamically scaled models at normal gravitational acceleration. More viscous materials have the advantages of being

easier to roll into fine layers, and they are easier to cut and photograph without inducing further deformation.

Rheologic similarity requires that the model and natural materials follow a similar flow law, and that the viscosity ratios between strata are equal in model and nature (Weijermars & Schmeling 1986). Dow Corning silicone bouncing putty and Plasticine modeling clay are both non-Newtonian visco-elastic fluids (McClay 1976, Dixon & Summers 1986, Weijermars 1986), a reasonable rheologic choice to represent buckling (e.g. Smith 1977, Neurath & Smith 1982, Lan & Hudleston 1991). Their viscosity ratio, dependent on the strain rate, is approximately two orders of magnitude for these experiments (Dixon & Summers 1985) (Table 2.2). At high strains, high strain rates, and high viscosity contrasts, Plasticine fractures and occasionally faults. Therefore the deformation of the models does not represent the purely ductile processes of the lower crust. These materials have been used as analogs of unmetamorphosed, interbedded limestone and shale in previous models deformed in a centrifuge (Dixon & Summers 1985).

To apply the scaling equations, model parameters such as length, strain, and density are easily measured; viscosity, centrifugal acceleration, and strain rate are estimated. Values for the natural parameters of viscosity, strain rate, and density are also estimated. Substituting these values into equations (2.1) and (2.2) yields the model-to-nature ratio of lengths (Table 2.2).

The centrifugal acceleration varied throughout the experiment; thus several different values were compared for scaling purposes. The maximum acceleration, 940 times normal gravitational acceleration, is constant for all experiments (*g*max in Table 2.1). The average *g* (*g*mean) was computed using a linear approximation of

Table 2.2 Parameters used for scaling calculations

		unit	material	model		nature		model/nature	
density	ρ	kg/m^3	DC	$1.1x10^3$	a	$2.2x10^3$	e	$5.0x10^{-1}$	
			PL	$1.9x10^3$	a				
eff. viscosity	η	Pa s	DC	$1.0x10^5$	c	$1.0x10^{19}$	b	$1.0x10^{-14}$	
			PL	$1.0x10^7$	c	$1.0x10^{21}$	f	$1.0x10^{-14}$	
strain rate	ε	s^{-1}		$2.0x10^{-3}$	a	$1.0x10^{-14}$	d	$2.0x10^{-11}$	
accel.	gmax	m/s^2		$9.2x10^3$	a	9.8		$9.4x10^2$	
	gmean			$5.2x10^3$	a	9.8		$5.4x10^2$	
	g'			$7.1x10^3$	a	9.8		$7.2x10^2$	
resistive force	$\tau=\varepsilon\eta$	Pa	DC	$2.0x10^2$	b	$1.0x10^5$	b	$2.0x10^3$	
			PL	$2.0x10^4$	b	$1.0x10^7$	b	$2.0x10^3$	
body force	$\sigma=\rho gh$	Pa			b			$2.0x10^3$	
length	$h=\sigma/\rho g$	km		**$1.0x10^{-5}$**		**2.4**	b	**$4.3x10^{-6}$**	calc. from gmax
				$1.0x10^{-5}$		**1.3**	b	**$7.5x10^{-6}$**	calc from gmean
				$1.0x10^{-5}$		**1.8**	b	**$5.5x10^{-6}$**	calc. from g'

DATA SOURCE:

- a Measured in this study
- b calculated from other parameters
- c Weijermars & Schmeling 1986 and references therein
- d Pfiffner & Ramsay 1982
- e Turcotte & Schubert 1982
- f Marble at approx. 500°C, Carter 1976

the rate of centrifuge acceleration and deceleration. The mean equals the area under the acceleration versus time curve, divided by the total time (an analogous technique for computing normalized time in the centrifuge is described by Jackson *et al.* 1988). An additional value (g') was computed in a similar manner by disregarding the centrifuge deceleration period (because little deformation occurred then). For example, experiment c217 had a maximum gravitational acceleration equal to $940g$, mean equal to $524g$, and g' equal to $725g$.

The exact strain rate is difficult to measure in the centrifuge because the ram velocity is affected by the centrifugal acceleration and by the hydraulic head of the reservoir. Much of the deformation took place during the first two minutes of centrifuge rotation, before its maximum, steady-state rotation rate. As the hydraulic head declined, ram displacement diminished during the period of steady-state rotation and was negligible during the period of deceleration. Because the centrifuge was stopped and restarted several times for photography, each model underwent several cycles of variable strain rate. The strain rates were calculated for several experiments, using the total strain and the total time in the centrifuge, the incremental strain and the period for each strain increment, or incremental strain and the period discounting the centrifuge deceleration. A value of $2 \times 10^{-3} s^{-1}$ was chosen from these results as a representative strain rate to compute the scaling parameters.

The known and estimated experimental parameters yield a ratio of lengths (model to nature) of approximately 5×10^{-6} (Table 2.2). For example, 1 cm length in the model is analogous to about 2 km in nature. Individual layers in the microlaminate are approximately 0.025 cm thick, analogous to strata 50 m thick in nature. In summary, use of the centrifuge allows use of relatively viscous materials

to represent regional-scale structures that are affected by both tectonic and gravitational forces.

ANALYSIS

Structural evolution was studied from photographs of the model surface taken after each time step of centrifugal deformation. For select models, anticlinal hinges of the first generation folds were marked on the model surface after D_1 (heavy ink lines on model surfaces Figs. 2.3d, 2.8a, and 2.8c) for comparison with the deformed F_1 hinges after D_2. After D_2 deformation was complete, the models were removed from the centrifuge, frozen, and horizontally sectioned at 2 mm intervals. Profiles at the model boundaries were photographed for most models; however, no serial vertical sections were cut. Layer thicknesses were measured from the profiles. Because strain is most heterogeneous at the model boundaries, these measurements should be considered approximations. Crest-to-crest wavelengths of first (F_1) and second (F_2) generation folds were measured from photographs of plan views of the models' surfaces. The three-dimensional geometry of the structures was qualitatively evaluated by comparing the variation with depth of horizontal sections and by comparing horizontal sections and profiles.

To reconstruct the fold geometry more quantitatively, structure contour maps and stereograms were constructed (cf. Skjernaa 1975). Layer contacts of select models were digitized from photographs taken at successive depths. The digitized data volume was gridded using a kriging algorithm and contoured for individual deformed surfaces with the software Spyglass Transform. Comparison of the contours, a reconstructed three-dimensional surface, the digitized layer

contacts, and photographs of the model surface confirms that the reconstruction technique accurately reproduces the major structural trends, but may smooth some of the minor folds. Strikes and dips were calculated from a finite difference estimation of the first derivatives in the grid directions. They were plotted and contoured using the method of Kamb (1959) on lower hemisphere, equal area projections representing the entire model or select domains. Trend and plunge of fold hinges were measured at even intervals directly from the structure contours.

RESULTS

Preliminary Experiments

Several models were deformed in the centrifuge to test whether the basal and confining materials were appropriate. The results of the preliminary experiments confirmed the necessity of having a basal detachment layer, the appropriateness of using DC as a detachment material, and the value of deforming the models with an unconfined upper surface.

To test the necessity of a basal detachment, three models were constructed with the laminate placed directly on a rigid, lubricated base. Laminates of different colors of DC (model c223, D_1=34%, D_2=39%; model c226 D_1=65%, D_2=56%) thickened rather than buckled. No surface topography developed after either the first or second deformation; however, the surficial grid strain is heterogeneous. The deformation is associated with perturbations around air bubbles, in both profile and map view. No periodic structures resembling folds formed. Layer-parallel shortening is approximately 200% for model c223, and 500% for model c226. For high competence-contrast layering without a detachment, tight chevron folds

formed preferentially at the boundaries of the model, adjacent to the moving ram and the opposite wall. Few folds developed in the center of the model, away from the boundaries. A thicker detachment unit was used to help distribute the deformation away from the model boundaries.

Fold theory predicts that the dominant fold wavelength (i.e. the wavelength which amplifies at the fastest rate) increases for a viscous system with inverted density stratification under the influence of gravity (Ramberg 1970). Dow Corning silicone putty has a lower density than Plasticine or the PL-DC mixture (ρ = 1450 kgm^{-3}). To test whether the folding was affected by the buoyancy of the basal DC layer, one model was constructed with a dense basal detachment (ρ=1800 kgm^{-3}), made of a mixture of powdered galena with Rhodorsil gomme, a silicone bouncing putty. Folds were found to have the same style and mean wavelength as models with the less dense DC detachment. Apparently under these experimental conditions, buckling is more strongly controlled by the viscosity contrast of the laminate than by the density of the matrix. Because it was more readily available, DC was used as the detachment material.

To test whether the laminate needed its upper surface confined, two models were constructed with different confining materials. A 3 mm layer of PL was used as the strong confining layer above a 3 mm bilaminate with a 1 mm DC basal detachment. When shortened 30% in one direction, the PL buckled with an average wavelength of approximately 17 mm, more than twice the wavelength of the unconfined bilaminate. In the inner arc of the PL folds, the laminate deformed as short wavelength, tight folds . In the outer arc, the laminate folded with the same wavelength as the PL confining unit. Although this stratigraphy may represent

some geologic occurrences, this study seeks to model the multilayer folding without the influence of adjacent, strong units. When a 3 mm layer of DC was tested as a weak confining layer, the DC supported no surface topography, and thickened uniformly. Vertical slices through the model revealed concentric fold profiles in the bilaminate, insignificantly different in style, wavelength, or amplitude from the unconfined models. The scaling parameters calculated above suggest that the laminates represent a section of unconfined crust less than 1 km thick. At such shallow depths, dominantly brittle deformation is expected, but not observed in the models. Accordingly, the models are better analogs for depths where ductile processes dominate than for thrust belt structures. Because confinement of the models insignificantly affected their structural style, and to allow observation of the evolution of the top surface, the laminates were deformed unconfined.

Low Competence-contrast

Low competence-contrast stratigraphy was deformed in five models (Table 2.3, Figs. 2.2, 2.3). The rheologic contrast between the basal detachment and laminate controlled deformation, such that the laminate buckled as well as thickened. The rheology of the laminate controlled the differences in amplitude and wavelength between the PL laminates (Fig. 2.2, model c215) and the DC-PL mixtures (Fig. 2.3, models c216 and c224, Table 2.3). The degree of strain controlled differences between amplitude, wavelength, and layer-parallel shortening of the two DC-PL mixture models (Fig. 2.3, Table 2.3). After D_2, the high-strain DC-PL laminate (c224) thickened by approximately 230% and its basal detachment

Table 2.3. Models with low competence-contrast

model #	materials	#layers	% shortening		mean wavelength (cm)	
			D1	D2	F1	F2
c223	DC	12	34	39	N/A	N/A
c226	DC	12	65	56	N/A	N/A
c215	PL	16	44	31	1.30	2.25
c216	DC-PL mix	12	36	31	1.76	1.25
c224	DC-PL mix	12	52	44	1.03	1.70

Table 2.4. Models with high competence-contrast

model #	materials	#layers	% shortening		mean wavelength (cm)	
			D1	D2	F1	F2
c222	DC&PL	12	18	17	0.83	1.01
c218	DC&PL	12	54	20	0.64	1.30
c217	DC&PL	12	44	33	0.63	1.20
c220	DC&PL	12	37	37	0.68	1.14
c221	DC&PL	12	33	33	0.70	1.90
c213	DC&PL	16	28	38	0.61	0.69

Figure 2.2. Model c215, low competence-contrast PL laminate, D_1=44%, D_2=31%. The strips of laminate inserted post-D_1 and pre-D_2 were cropped from most of these and subsequent photographs. For all the photographs, the surface grid was initially square with 5 mm spacing, the lightest colored material is DC silicone putty, and the scale bar is in millimeters. (a) Top surface. (b) Horizontal section 12 mm deep.

a)

b)

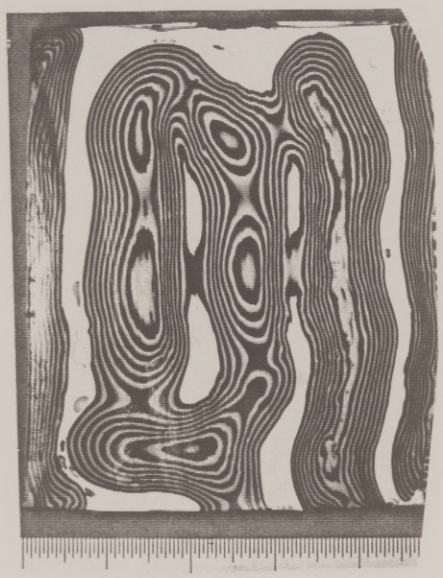

Figure 2.3 Models with low competence-contrast DC-PL mixture. (a) Model c216, D_1=36%, D_2=31%, oblique view with profile of F_1's in the foreground. (b) Model c216, horizontal section 10 mm deep. (c) Model c224, D_1=52%, D_2=44%, profiles of F_1 folds before D_2. (d) Model c224, top surface. F_1 crests were inked prior to D_2. (e) Model c224, horizontal section 6 mm deep.

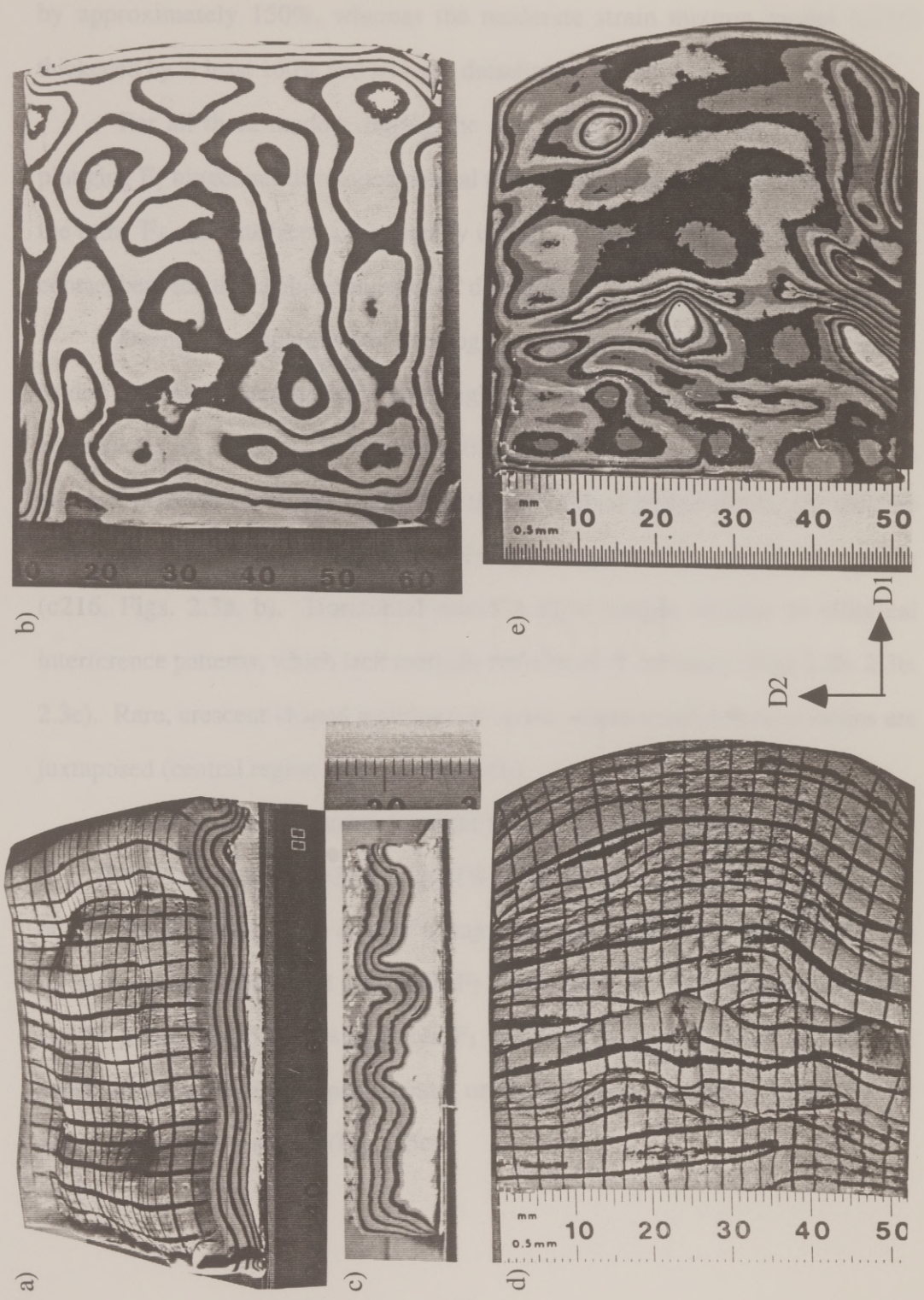
b)
e)
D1
D2
a)
c)
d)
mm
0.5mm
10
20
30
40
50

by approximately 150%, whereas the moderate strain mixture model (c216) thickened by at least 160% and its basal detachment by approximately 200%.

For all three models, during the first phase of shortening (D_1) doubly-plunging F_1 hingelines developed normal to the shortening direction and parallel to the ram. F_1 axial surfaces are generally upright. Parasitic folds are present at the contact between the laminate and the DC detachment.

During D_2, regardless of rheology or degree of shortening, F_1 hingelines folded into domes and basins with upright, approximately planar F_1 and F_2 axial surfaces (Figs. 2.2, 2.3). In models with differential shortening (c215, Fig. 2.2), domes and basins are elongate normal to the direction of greater shortening; they are equant for the model with approximately equal degrees of D_1 and D_2 shortening (c216, Figs. 2.3a, b). Horizontal sections show simple circular to elliptical interference patterns, which lack multiple inflections of curvature (Figs 2.2b, 2.3b, 2.3e). Rare, crescent-shaped interference occurs where small domes or basins are juxtaposed (central region of c216, Fig. 2.3b).

Structure contours and poles to the top surface were reconstructed for model c216 (DC-PL mixture, D_1=36%, D_2=31%)(Figs. 2.4 & 2.5a). Data from transects on individual limbs and the crest of a major anticline yield the orientations of local F_1 axes, and the combined data yield F_2 axes (Fig. 2.5b). The orientation of F_1 and F_2 hinges demonstrates that both F_1 and F_2 hingelines are curved, but lie on approximately planar, steeply dipping, orthogonal axial surfaces, as expected for dome-and-basin structures (Fig. 2.5c).

Figure 2.4. Structure contours of the top surface of c216 (compare with Fig. 2.3a).

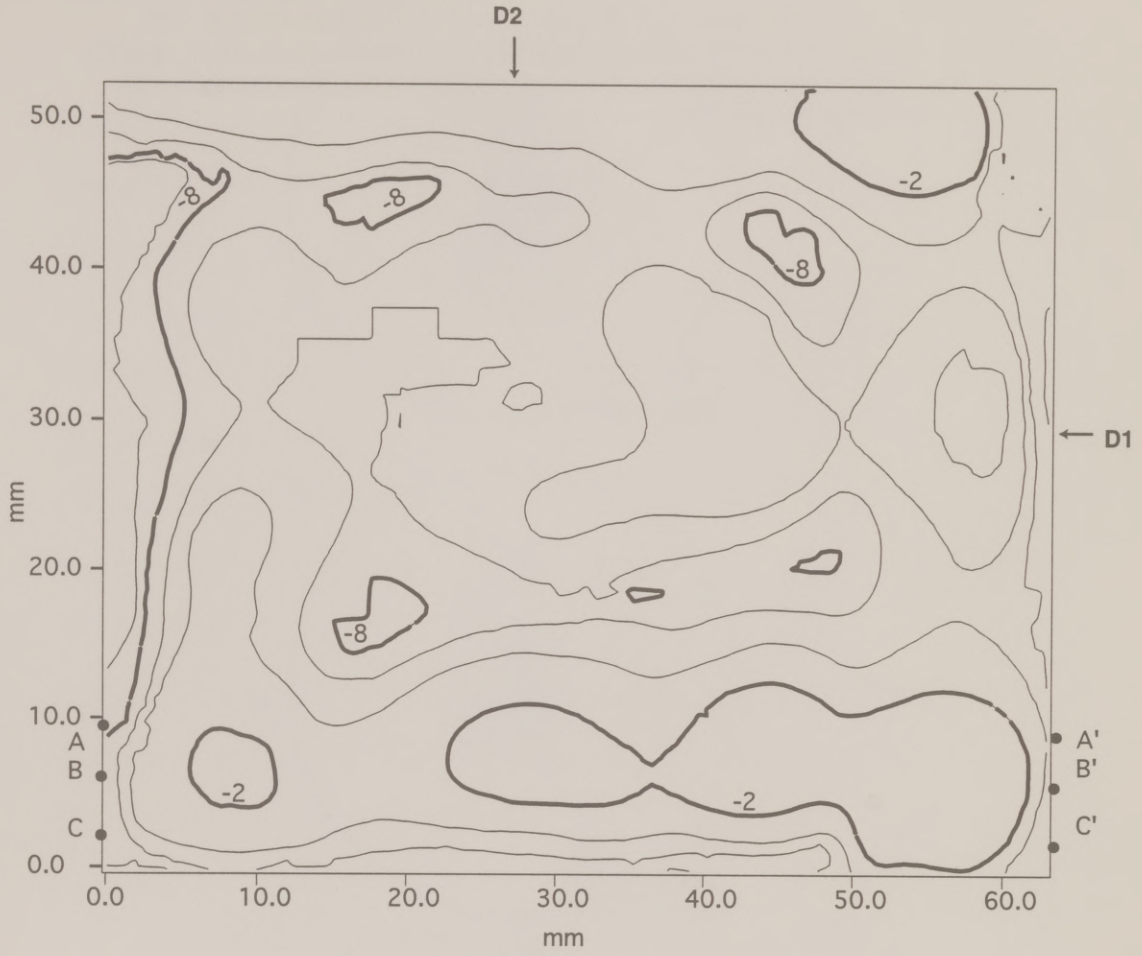

C.I.=2mm, bold contours @ -2 and -8mm

Figure 2.5. (a) Equal-area projections of 2500 equally distributed poles to upper surface of the model, contoured according to Kamb (1959). (b) Equal-area projections of poles to bedding for domains A-A', B-B', and C-C'. (c) Equal area projections of F_1 and F_2 hingelines measured directly from the structure contours.

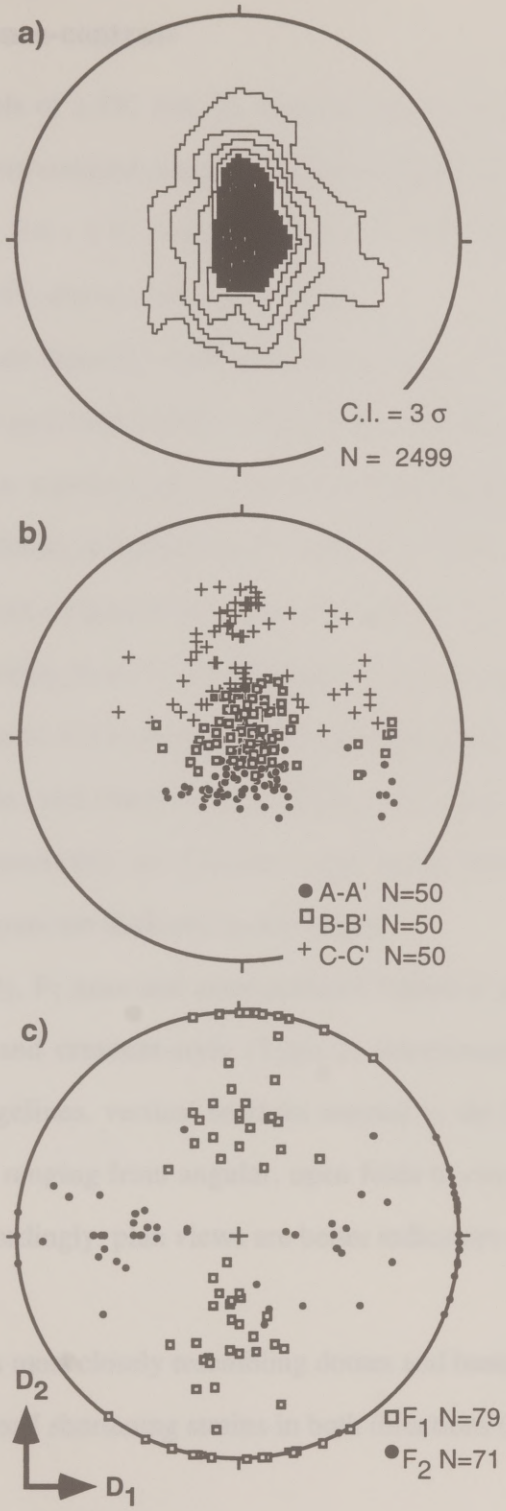
a)
C.I. = 3 σ
N = 2499
b)
A-A' N=50
B-B' N=50
C-C' N=50
c)
D2
D1
F1 N=79
F2 N=71

High Competence-contrast

Six models of a DC and PL multilaminate demonstrate that buckle fold interference is more complex where the stratigraphy has a high competence-contrast (Table 2.4, Figs. 2.6 - 2.8). All models in this series were made of alternating layers of DC and PL above a basal detachment.

F_1 folds are typically doubly-plunging (Fig. 2.6a). With progressive D_1 shortening, these periclines linked to form folds with apparently curved hingelines and axial surfaces, a process also observed in other buckle fold models (Ghosh & Ramberg 1968, Dubey & Cobbold 1977, Blay *et al.* 1977, Guterman 1980). Folds in models with high competence-contrast have shorter F_1 wavelengths for the same amount of shortening than F_1 wavelengths in low competence-contrast models (Table 4). In profile, the F_1 fold styles are predominantly lobate-cuspate, but also include box style, and chevron (Fig. 2.6a). PL layers tend to maintain their thickness and commonly are fractured and rarely faulted in the inner-arc of anticlines. DC layers are thickened in the hinges.

During D_2, F_1 axes and axial surfaces folded to produce both dome-and-basin (Type 1) and crescent-style (Type 2) interference. Because of steeply plunging F_2 hingelines, vertical sections normal to the D_2 shortening direction show fold styles ranging from angular, open folds to circular interference shapes (Fig. 2.6b). Accordingly, plan views are better indicators of fold interference style and F_2 fold style.

Structures most closely resembling domes and basins characterize the model with relatively small shortening strains in both directions (c222, Fig. 2.7). F_2 folds

Figure 2.6. Models with high competence contrast. Laminates in all models are alternating layers of DC (lightest colored layers) and PL (dark layers). (a) Oblique view of periclinal F_1 folds (model c217, D_1=44%, D_2=33%). (b) Typical F_2 profiles (model c218, D_1=54%, D_2=20%). Because F_2 plunge varies with depth, the vertical section lacks a characteristic fold style.

a)

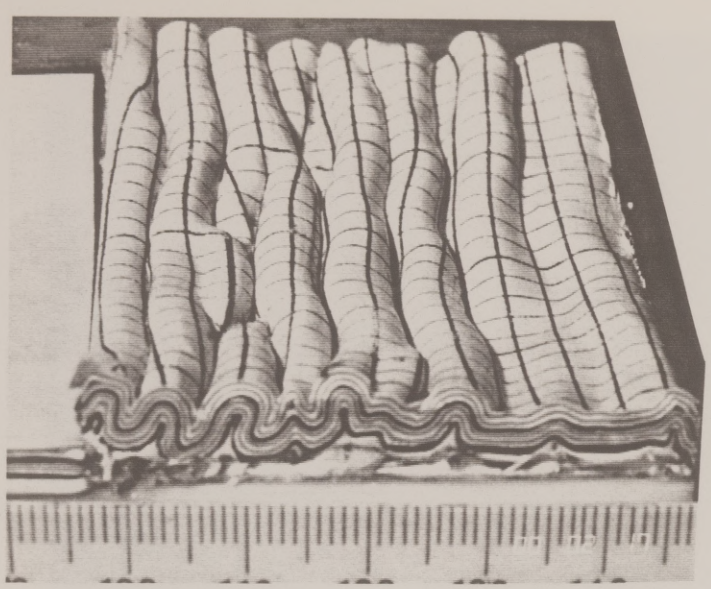

b)

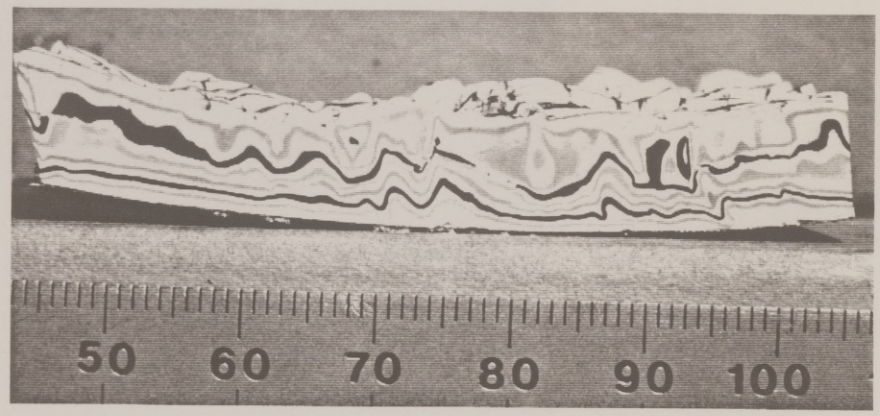

Figure 2.7 Model c222, D_1=17%, D_2=18%. (a) Top surface. (b) Horizontal section 10 mm deep. (c) Axial traces from horizontal section 10 mm deep.

a)

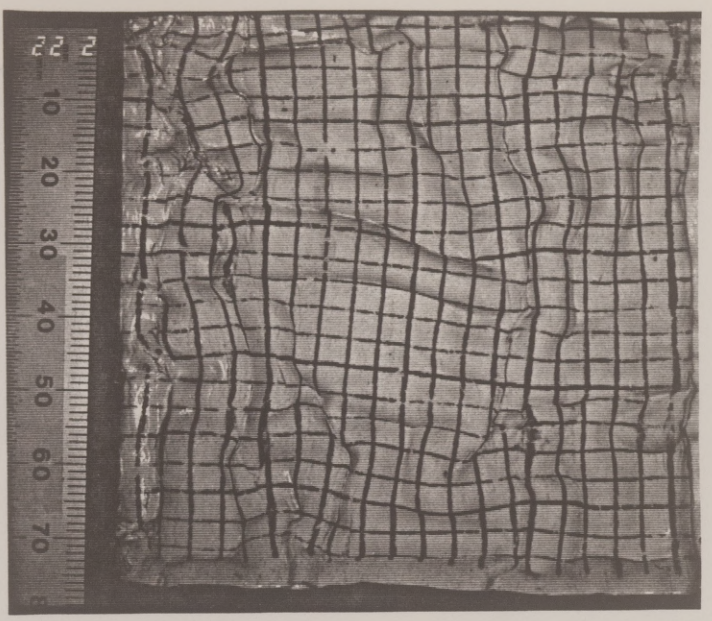

b)

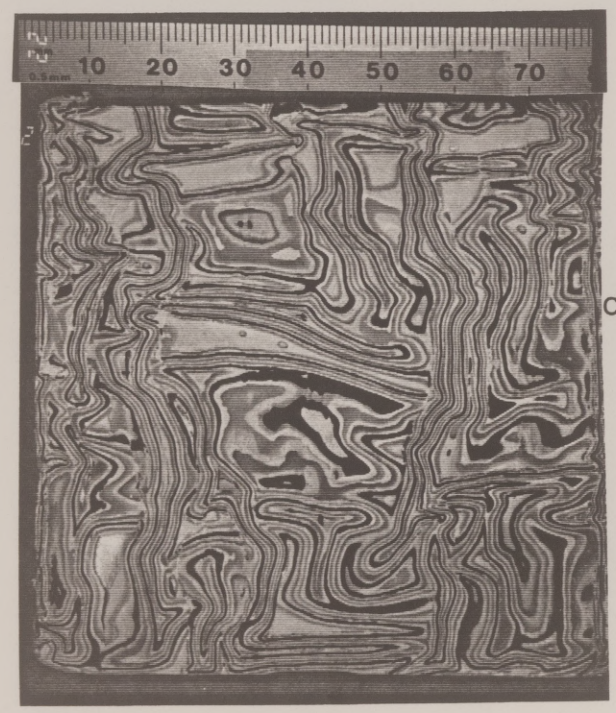

c)

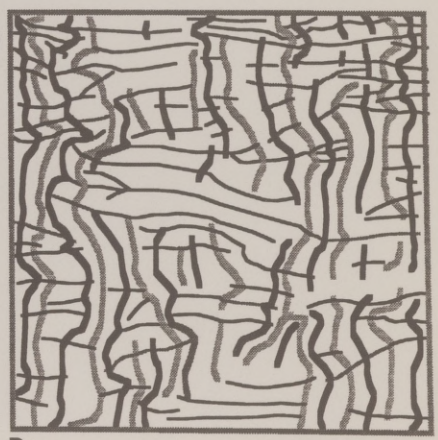

Figure 2.8. Models with high competence contrast layering. (a) Model c218, upper surface. (b) Model c218, D_1=54%, D_2=20%, horizontal section at 10 mm depth. (c) Model c217, D_1=44%, D_2=33%, upper surface. Hinge migration is evident in the difference between inked pre-D_2 F_1 crests and the present F_1 crests. (d) Model c217, horizontal section at 14 mm depth.

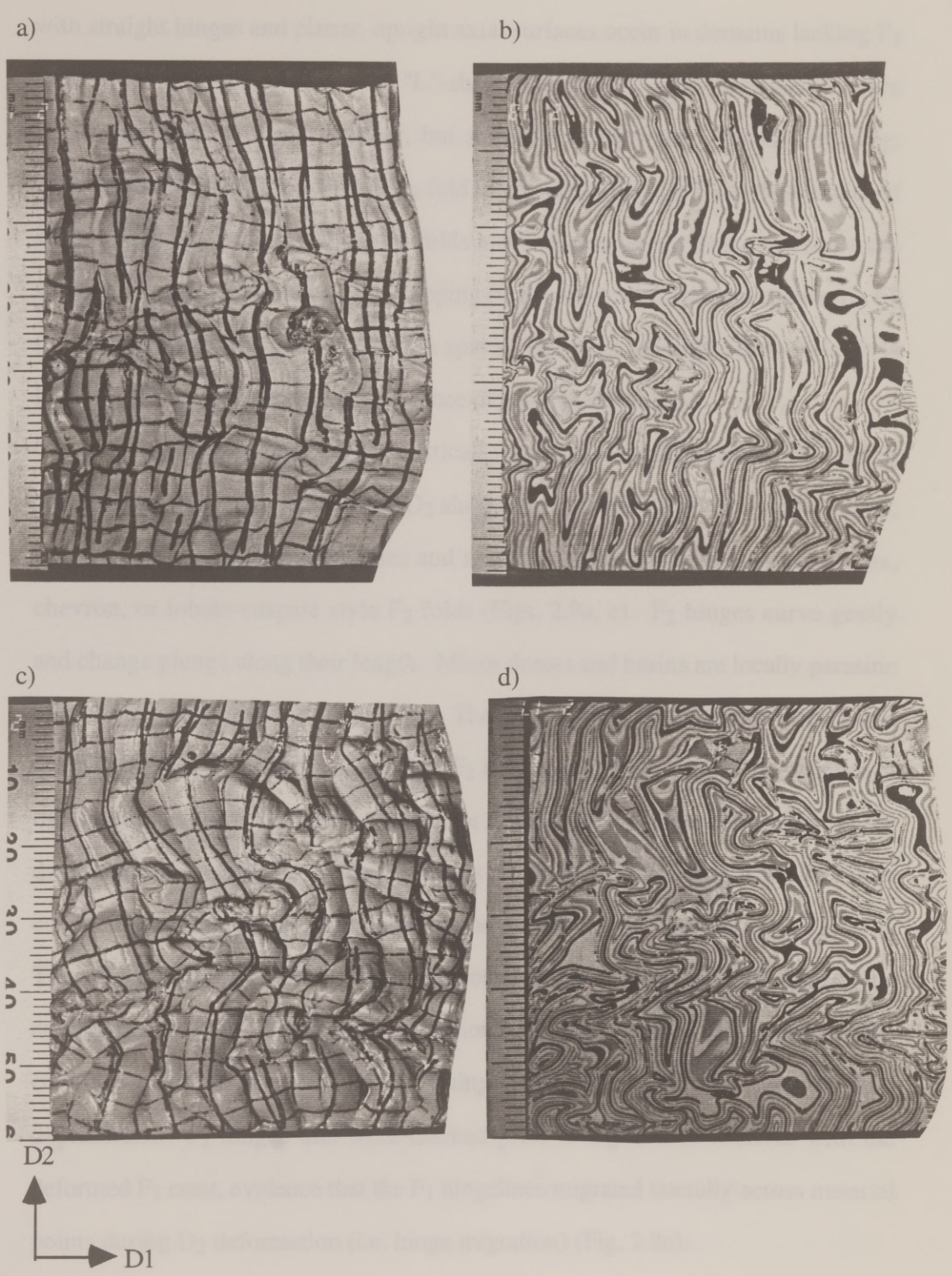
a)
b)
c)
d)
D2
D1

with straight hinges and planar, upright axial surfaces occur in domains lacking F_1 folds (central region of Fig. 2.7). "L"-shaped and "T"-shaped folds occur where F_1 and F_2 folds abut one another, but show no overprinting relationship (Fig. 2.7b)(cf. Skjernaa 1975). F_1 and F_2 fold intersections locally form the corners of square domes or basins. Where F_1 folds are well developed, their axes and axial surfaces are refolded about steeply dipping F_2 axes as open, lobate-cuspate style F_2 folds (Figs. 2.7b, c). Because of the spatial variation in interference style, it is locally difficult to determine the sequence of fold superposition.

Fold interference is characteristically Type 2 for models with D_1 shortening >20%, regardless of the amount of D_2 shortening (models c213, c217, c218, c220, c221). In plan view, F_1 hingelines and axial surfaces are refolded as broad box, chevron, or lobate-cuspate style F_2 folds (Figs. 2.8a, c). F_2 hinges curve gently and change plunge along their length. Minor domes and basins are locally parasitic upon larger crescent-shaped structures. The hinges of minor domes and basins and the grid lines commonly fan around the F_2 axial trace (Fig. 2.8c). Narrow zones of tightly refolded F_1 folds occur in conjugate sets that are oblique to either shortening direction and parallel to the axial traces of the box folds (Fig 2.8a, c). The conjugate sets are distributed throughout the model, and thus are not corner effects. The grid markers are offset with an opposite sense of shear on either set of the conjugate zones, and the zones are commonly structural crests. Intersection of the conjugate strain zones and change in F_2 hinge orientation coincide with F_1 periclinal depressions. F_1 hinges that were marked prior to D_2 do not coincide with the deformed F_1 crest, evidence that the F_1 hingelines migrated laterally across material points during D_2 deformation (i.e. hinge migration) (Fig. 2.8c).

Horizontal sections of models with >20% D_1 shortening show a combination of complex elliptical and crescent map patterns and a change of structural style with depth (Figs. 2.8b, d). Shallow depths show simple crescents at F_2 crests and ellipses elongate parallel to the axial traces of box-folds and minor domes. Deeper horizontal sections show F_1 axial traces refolded into chevron, cuspate-lobate and box-style folds. PL layers tend to be faulted, fractured, and boudinaged in the conjugate zone traces. The conjugate zone intersections are loci of the most complex interference shapes. The progression from inner to outer-arc of a F_2 fold is typically expressed as a change in interference style from ellipses elongate normal to the D_2 shortening direction, to tight crescents, to broad crescents elongate normal to the D_1 shortening direction. Axial traces at different depths show a change in folded F_1 axial traces from cuspate to lobate, or from single- to double-hinged (c217, Figs. 2.9 & 2.10). Note that the fold style of F_1 axial traces is similar to the style of F_1 folds in profile (compare Figs. 2.9 and Fig. 2.6a). Additionally, F_2 axial traces branch or bifurcate at different depths. Axial traces from different depths projected onto the same plane demonstrate that both F_1 and F_2 axial surfaces dip steeply (Fig. 2.10).

Differences between the interference styles in models with >20% D_1 shortening are related to the amount of shortening in each direction. Increased degree of D_1 shortening relative to D_2 shortening generally correlates with the development of the conjugate strain zones. For a high ratio of D_1 to D_2 shortening, F_2 folds have a pronounced box-style in plan view (c218, D_1: D_2=2.7, Figs. 2.8a, b). An approximately equal ratio of D_1 and D_2 shortening favors the development of rounded, lobate-cuspate style F_2 folds (c221, D_1: D_2=1 ; c220, D_1: D_2=1; c217

Figure 2.9. Axial traces of model c217 (compare with Fig. 2.8c). F_1 axial traces are refolded into lobate-cuspate and box-style folds. F_2 axial traces are defined by the maximum curvature of F_1 axial traces, small domes and basins superimposed upon the broader refolded F_1 folds, and the conjugate traces of box-style F_1 folds. (a) 10 mm deep, (b) 14 mm deep, (c) 18 mm deep.

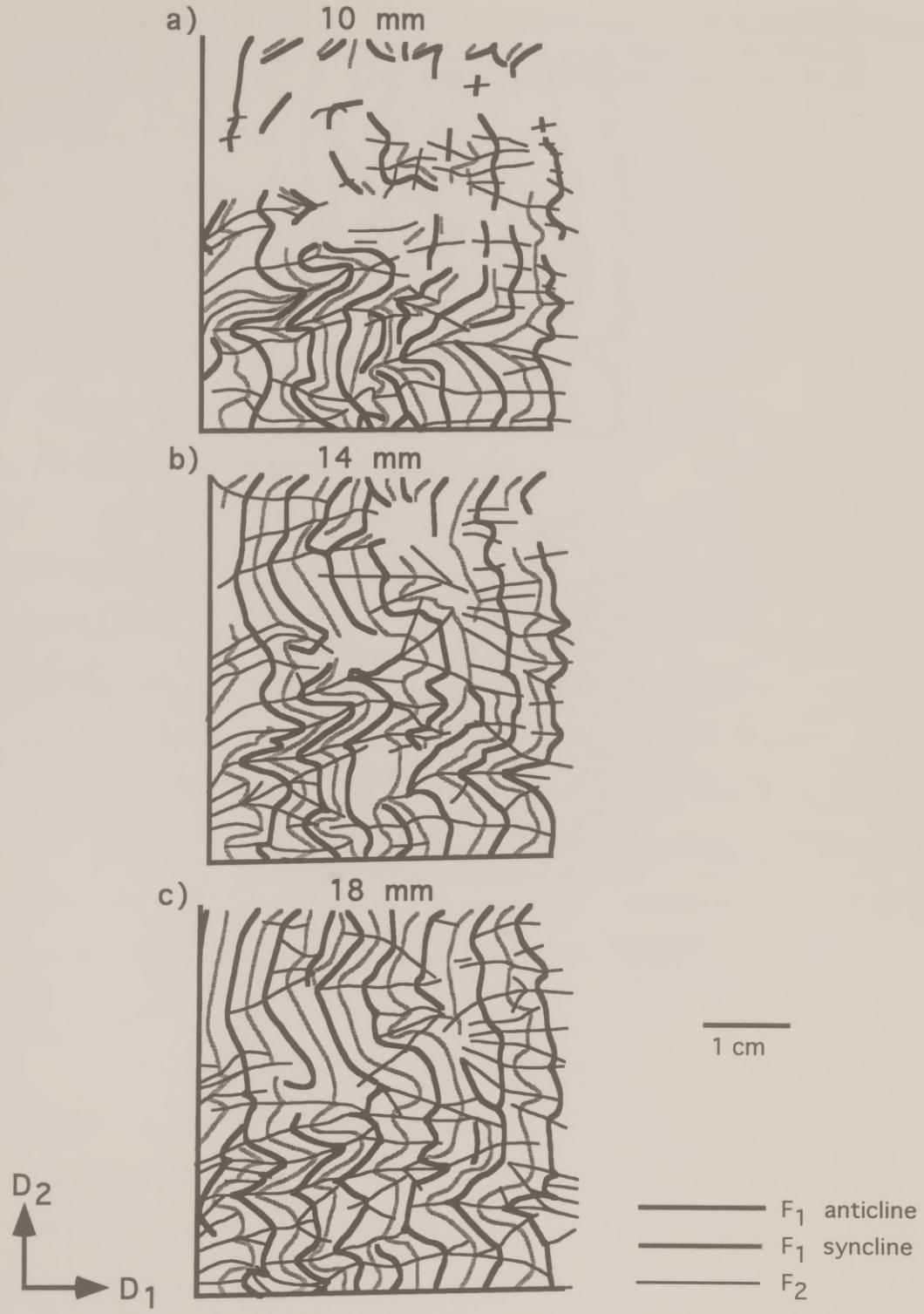
a)
10 mm
b)
14 mm
c)
18 mm
1 cm
D2
D1
F1 anticline
F1 syncline
F2

Figure 2.10. Axial traces of model c217. (a) Traces of F_1 anticlines, projected onto a single plane to illustrate change in fold style with depth. (b) F_2 axial traces projected onto a single plane.

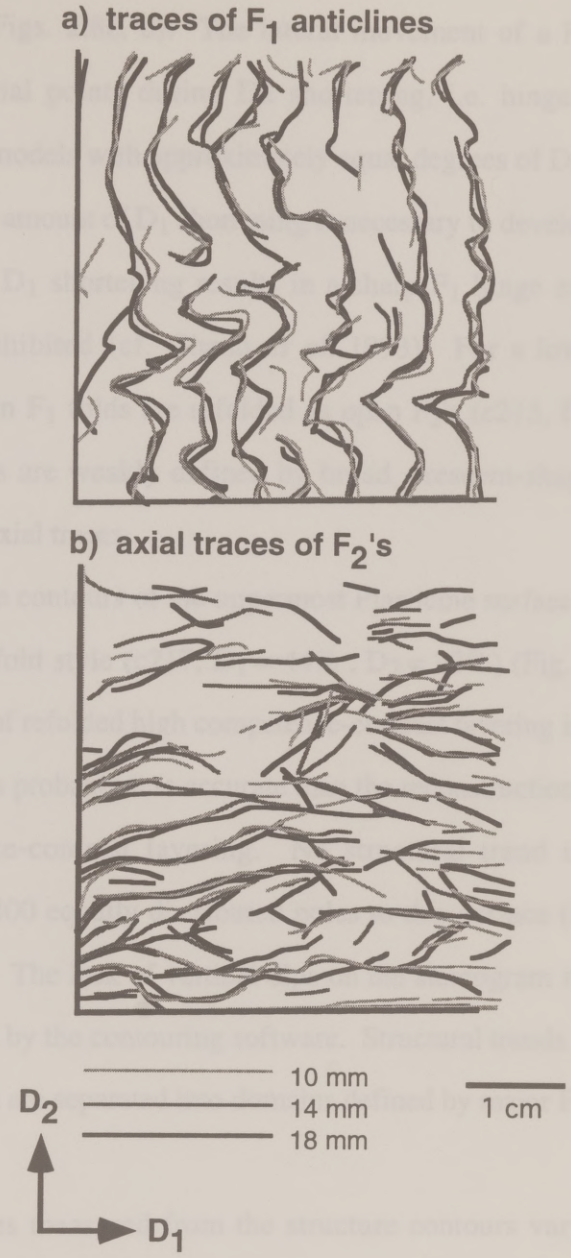
a) traces of F_1 anticlines
b) axial traces of F_2's
10 mm
14 mm
18 mm
1 cm
D_2
D_1

D_1: D_2=1.33; Figs. 2.8c, d). The lateral movement of a F_1 crestline through different material points during D2 shortening, i.e. hinge migration, is most pronounced in models with approximately equal degrees of D_1 and D_2, suggesting that a minimum amount of D_1 shortening is necessary to develop the F_1 hinge, yet a high degree of D_1 shortening results in a sharp F_1 hinge zone where fold axis migration is inhibited (cf. Ghosh *et al.* 1993). For a low ratio of D_1 to D_2 shortening, open F_1 folds are refolded as open F_2's (c213, D_1: D_2 = 0.73). The conjugate zones are weakly defined by broad, crescent-shaped map patterns or folds in the F_1 axial traces.

Structure contours of the uppermost Plasticine surface illustrate the highly noncylindrical fold style (c217, D_1 = 44% , D_2 = 33%) (Fig. 2.11). Because the structural style of refolded high competence-contrast layering is more complex, this reconstruction is probably less accurate than the reconstruction for the models with low competence-contrast layering. No structural trend is evident from the projection of 2400 equally distributed poles to this surface (Fig. 2.12a, compare with Fig. 2.5a). The lack of vertical dips on the stereogram may be an artifact of smoothing done by the contouring software. Structural trends are more apparent if some of the data are separated into domains defined by major F_1 and F_2 axial traces (Fig. 2.12b).

F_1 hinges measured from the structure contours vary in both trend and plunge, but are predominantly horizontal (Fig. 2.12c). Thus the primary effect of D_2 shortening is the refolding of originally subhorizontal F_1 hinges within the horizontal plane, about steeply plunging F_2 axes. A secondary population of F_1 hinges varies in plunge along a north-south trending girdle, indicative of a Type 1

Figure 2.11. (a) Structure contours of the upper PL surface of c217. (b) Enlargement of boxed area in (a). F_1 and F_2 axial traces bound the structural domains in Fig. 2.12.

a)

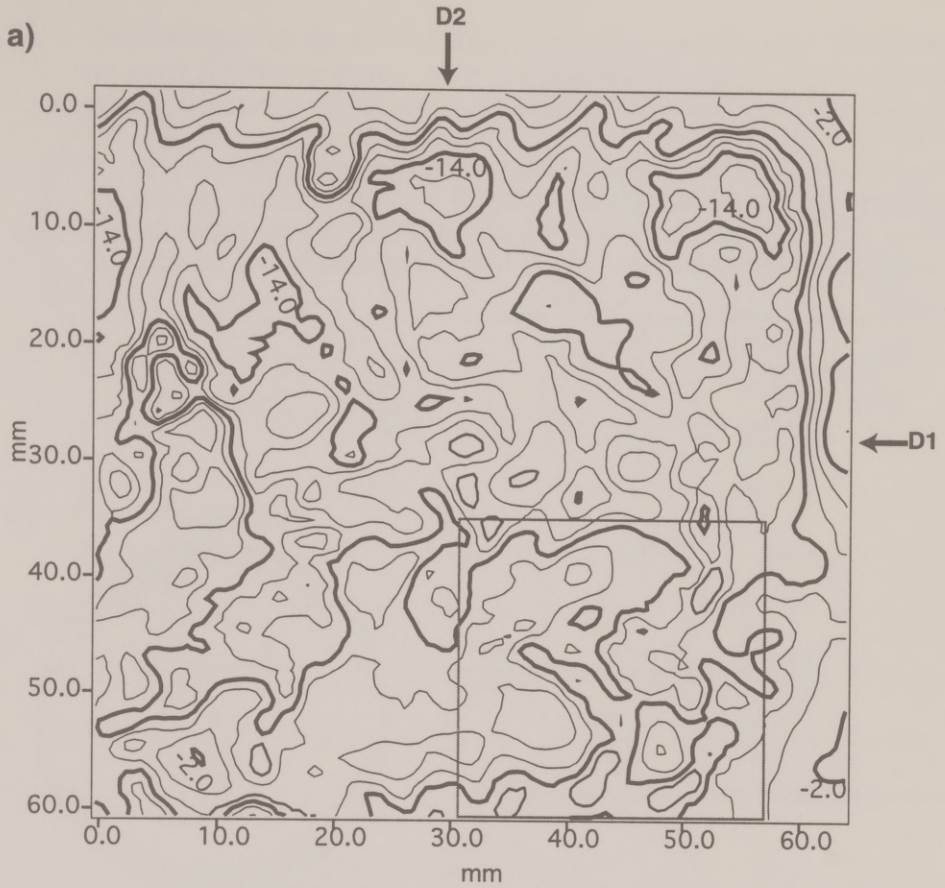

C.I.=2mm, bold contours @ -2, -8, & -14

b)

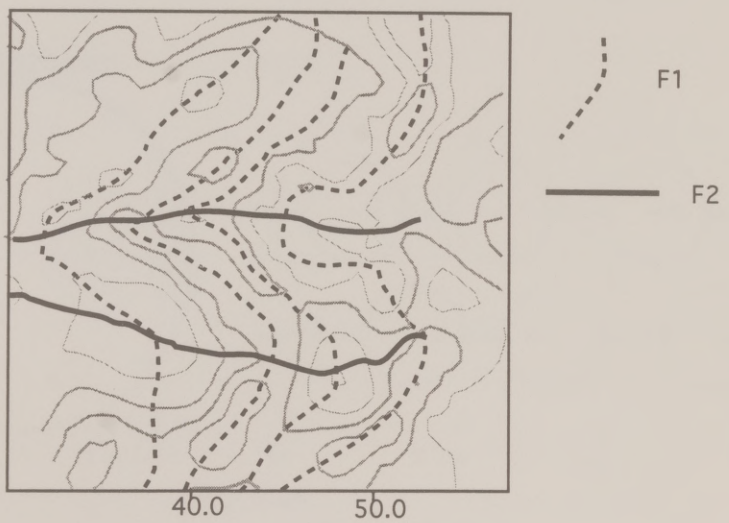

Figure 2.12. Orientations of bedding and fold axes for the surface contoured in Fig. 2.11. Fold hingelines were measured directly from the structure contours. Schematic axial traces illustrate the relationship between the domains and the local structures. Contoured stereograms use the method of Kamb (1959). (a) Bedding poles over entire surface. (b) Bedding poles subdivided by domains. (c) F_1 hinge lines of the entire surface. (d) F_1 hinge lines subdivided by domain. (e) F_2 hinge lines measured from entire surface. (f) F_2 hinge lines subdivided by domain.

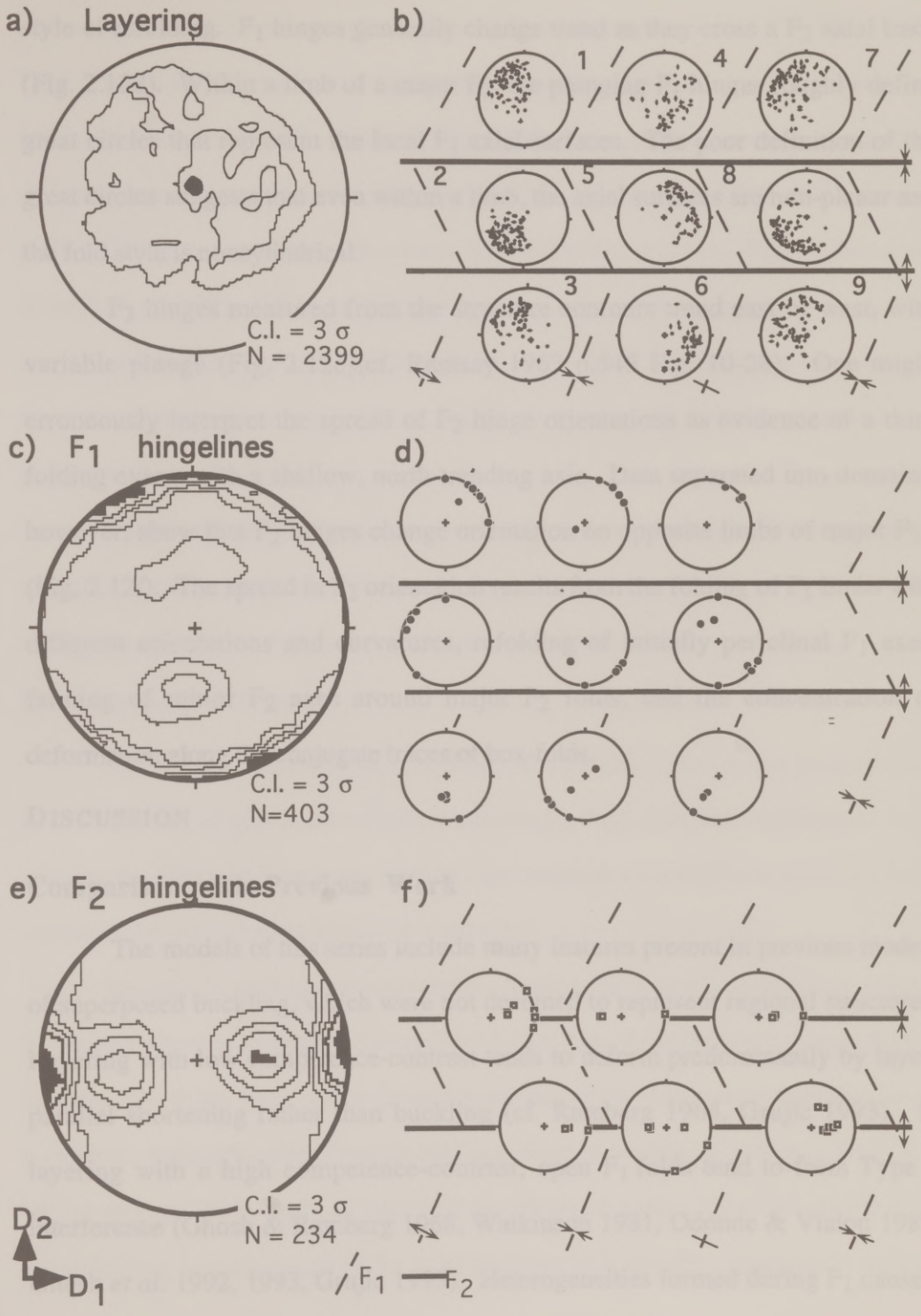
a) Layering
C.I. = 3 σ
N = 2399
b)
1
2
3
4
5
6
7
8
9
c) F1 hingelines
C.I. = 3 σ
N=403
d)
e) F2 hingelines
C.I. = 3 σ
N = 234
f)
D2
D1
F1
F2

style of refolding. F_1 hinges generally change trend as they cross a F_2 axial trace (Fig. 2.12d). Within a limb of a major F_2, the plunging F_1 hinges roughly define great circles that represent the local F_1 axial surfaces. The poor definition of the great circles suggests that even within a limb, the axial surfaces are non-planar and the fold style is noncylindrical.

F_2 hinges measured from the structure contours trend east or west, with variable plunge (Fig. 2.12e)(cf. Ramsay 1967 p.545 Fig. 10-28). One might erroneously interpret the spread of F_2 hinge orientations as evidence of a third folding event, with a shallow, north-trending axis. Data separated into domains, however, show that F_2 hinges change orientation on opposite limbs of major F_1's (Fig. 2.12f). The spread in F_2 orientation results from the folding of F_1 limbs with different orientations and curvatures, refolding of initially periclinal F_1 axes, fanning of minor F_2 axes around major F_2 folds, and the concentration of deformation along the conjugate traces of box-folds.

DISCUSSION

Comparison with Previous Work

The models of this series include many features present in previous models of superposed buckling, which were not designed to represent regional structures. Layering with low competence-contrast tends to deform predominantly by layer-parallel shortening rather than buckling (cf. Ramberg 1964, Grujic 1993). In layering with a high competence-contrast, open F_1 folds tend to form Type 1 interference (Ghosh & Ramberg 1968, Watkinson 1981, Odonne & Vialon 1987, Ghosh *et al.* 1992, 1993, Grujic 1993). Heterogeneities formed during F_1 cause a

heterogeneous interference style (Ghosh & Ramberg 1968, Skjernaa 1975). Both Type 1 and Type 2 interference patterns are found in the same model (Watkinson 1981, Ghosh *et al.* 1992, 1993, Grujic 1993). F_1 hingelines migrate across different material points during D_2 (Ghosh 1974, Ghosh *et al.* 1992, 1993, Grujic 1993). Different amplitude structures have different styles of fold interference (Ghosh *et al.* 1992, 1993). Additionally many of the mechanisms, or modes, of superposed buckling as defined by Ghosh *et al.* (1992, 1993) can be identified. Models in this study have no evidence of Mode 4, where F_1 folds are isoclinal and there is no hinge migration.

The results that are common to models with either insignificant (previous work) or significant (this study) body forces, therefore, should be qualitatively analogous to both outcrop- and regional-scale fold interference.

Gravitational Effects

Some differences between this study and previous studies can be attributed to the influence of gravitational body forces on the fold style. The differences may account for differences between outcrop- and regional-scale fold interference where the initial fold-enveloping surface is horizontal.

During D_1, centrifugal acceleration (analogous to gravitational acceleration in nature) opposes F_1 amplification (Fig. 2.1a). Gravity effectively damps the F_1 shapes. F_1 folds have more pronounced box-style outer-arcs than the first-generation folds of previous buckle-fold interference models, so gravity contributes to the change with depth of the fold interference style. Gravity opposes F_2 amplification parallel to upright F_1 axial surfaces, so it aids F_2 amplification normal

to F_1 axial surfaces, enhancing Type 2 interference. Because of the influence of gravitational body forces, the pronounced folding of F_1 axial surfaces might be more easily developed in regional-scale than in outcrop-scale superposed folds in nature.

Boundary Effects

In the models, the fold style and orientation are affected by the presence of rigid boundaries. For example, structure contours have higher amplitudes near the boundaries (Figs. 2.4 & 2.11). F_1 fold hingelines developed parallel to the moving rams; however, initially straight F_1 axial traces show no evidence of differential displacement due to adherence to the sidewalls. During D_2 the models extruded slightly into the strip of undeformed laminate (curved right-hand boundary of Figs 2.3 - 2.8). The upper, free surface provided a rheologic interface that affected the deformation, especially of the low competence-contrast models.

The effects of near-field, rigid boundaries are not ideal but may not be entirely artificial, given that natural structures depend on the presence and orientation of natural boundaries such as continental margins or preexisting basement faults (e.g. Braun 1993; natural examples which were influenced by natural boundaries are described in Ch. 4). In this study, the boundary conditions are not systematically varied, so their influence is difficult to quantify. Nonetheless, the boundary conditions are equivalent between the two model series, making the results comparable. Differences between the models are thus dominantly controlled by variables other than boundary conditions.

Strain Accommodation

Unlike previous work where F_1 fold style was the primary determinant of interference style (Ghosh & Ramberg 1968, Watkinson 1981, Odonne & Vialon 1987, Ghosh *et al.* 1992, 1993, Grujic 1993), in this study competence-contrast was the important variable. Low competence-contrast stratigraphy accommodates shortening by a thickening and folding of the entire multilaminate package during both shortening events, rather than by buckling of individual competent layers. The fold interference is expressed as simple, laterally homogeneous Type 1 map patterns, generally lacking curvature-accommodation folds, regardless of the ratio of D_1 to D_2 shortening or the amplitude of F_1 folds (compare Figs. 2.3e and 2.7b). High competence-contrast stratigraphy accommodates shortening by buckling of the more competent PL layers and thickening of the DC silicone putty layers in the fold hinge zones. The interference patterns are complex hybrids between Type 1 and Type 2 interference, with Type 2 interference dominant. Both F_1 folds in profile and F_2 folds in plan view include cuspate-lobate, chevron, and box-style folds, fold styles consistent with a buckling mechanism. The style of fold interference is heterogeneous laterally and with depth. F_2 fold wavelength is generally greater than F_1 wavelength, regardless of percent shortening in either direction, suggesting that the corrugation of the model during D_1 establishes a structural anisotropy (Watkinson & Cobbold 1981), which strengthens the model (Ramsay 1967 p. 548).

The presence of a basal detachment controls the shortening of both high and low competence-contrast laminates. The rheologic contrast between the detachment

and the laminate provides a localized, planar anisotropy, which buckles during D_1. Consequently, models with low competence-contrast layering do not strictly represent passive folding. Shortening of the high competence-contrast layering is accommodated by the buckling of the multilaminate package, which is more competent than the basal detachment, as well as by the buckling and fracture of individual PL layers and interlaminar flow of the less competent DC layers. This leads to different orders of folding and of fold interference (cf. Ramberg 1964, Ghosh *et al.* 1993).

The development of a structural anisotropy subparallel to F_1 axial surfaces facilitates the development of Type 2 fold interference. High competence-contrast laminates that were shortened by more than 20% deformed in a lobate-cuspate F_1 fold style, so that the DC basal detachment flowed into the cusps of the F_1 anticlines. The resultant alternation of steeply dipping laminate with the less competent detachment defined a steep, planar anisotropy that is roughly parallel to F_1 axial surfaces. For example, deep horizontal sections show lobate-cuspate F_2 folds cored by DC cusps. Field examples of analogous steeply dipping detachments associated with km-wavelength refolding are described by Schwerdtner and van Berkel (1991) and Schwerdtner *et al.* (1989). In models with low competence-contrast, and in models with high competence-contrast but low D_1 shortening, Type 2 interference is rare because the D_1 anisotropy is weakly developed.

The D_1 structural anisotropy also facilitates the development of box-style F_2 folds and the partitioning of the D_2 shortening strain into the conjugate high-strain zones. The pronounced box-style F_2 folds in map view that characterize models

with a high degree of D_1 shortening (Fig. 2.8a) are thus broadly analogous to kink folds that develop in profile in highly anisotropic rocks (e.g. Dewey 1965, Cobbold *et al.* 1971).

Although for similar folds the bulk shortening and elongation directions control the style of fold interference (Ramsay 1962, 1967 p. 521), in this study the bulk strain axes were not the chief control. Indeed, Grujic (1993) demonstrated experimentally that D_2 extension direction is a minor influence on interference type of superposed buckle folds. In this study, the bulk strain axes were not systematically varied. The D_2 direction of maximum shortening was fixed, but the D_2 extension direction may not have been. During D_2, rigid walls parallel to the F_1 axial surfaces impeded significant horizontal extension, normal to the F_1 axial surfaces. Slight extrusion into the strip of undeformed laminate inserted prior to D_2 (Figs. 2.3 & 2.8), however, is evidence of a component of D_2 extension normal to the F_1 axial surfaces. Accordingly, the F_1 axial surfaces did fold, with an amplification direction normal to the rigid sidewall. Thus the models' boundary conditions did not impose bulk plane strain for D_2, allowing the simultaneous development of both Type 1 and Type 2 interference. Although the highly strained, low competence-contrast model extruded into the undeformed laminate strip, it lacked Type 2 interference (c224, Fig. 2.3d), further evidence that rheology rather than boundary conditions controlled the interference style.

Implications for Field Analysis of Regional Fold Superposition

Low competence-contrast

The models predict that in rocks with low competence-contrast, folds

recognized as simple map patterns without curvature-accommodation folds, with planar foliation, and with a variety of plunges, but consistent trends for both F_1 and F_2 axes. The sequence of folding is ambiguous from the geometry of the structures alone.

Both Type 1 and Type 2 fold interference have been described for high-grade metamorphic rocks with a similar fold-style, where little competence-contrast is expected (e.g. Ramsay 1962). In such cases, the style of fold interference is more likely controlled by variables not tested in the present study, such as kinematic directions (Ramsay 1967 p. 520) or the presence of axial-planar schistosity.

High competence-contrast

The models predict that superposed folds in strata with high competence-contrast interfere as a complex hybrid of Type 1 and Type 2 deformation. Just as buckle folds have a more heterogeneous strain distribution than passive folds, buckle fold superposition in the models produces a characteristically heterogeneous interference style. In the field, fold generations are differentiated on the basis of orientation, style, and overprinting relationships (e.g. Ramsay 1967 p. 520-553, Williams 1985). Because the models represent regional-scale fold superposition, the lateral and depth variation of F_1 and F_2 trends and interference style are analogous to map-scale heterogeneity. Recognition of the factors that affect the local style and orientation of structures formed by superposed buckling may help regional correlation of fold generations in rocks.

In the models where D_1 shortening is less than 20%, the initial F_1 fold distribution affects the interference style (Fig 2.7)(cf. Ghosh & Ramberg 1968,

Skjernaa 1975). If domains of different initial F_1 style and distribution were mapped independently, the regional fold sequence might be misinterpreted and only one fold generation identified. Where the F_1 and F_2 folds abut without overprinting, the map patterns resemble Type 2 crescent-shapes, and the axes of symmetry of the "L"-shaped folds could be misinterpreted as a fold axis unrelated to either fold generation.

The initial F_1 fold orientation affects the F_2 fold style. In the models, F_1 periclinal depressions coincide with complex F_2 fold style (cf. Ghosh & Ramberg 1968 Fig. 8 p.98, Skjernaa 1975). In the field, discontinuous F_1 or F_2 axial traces, intersection of box-fold axial traces, irregular interference patterns with multiple inflections of curvature, or a distinct, localized change in fold style of deformed F_1 axial traces could be evidence of variation in the initial plunge of F_1 axes. Additionally, in some of the models adjacent or bifurcating F_1 periclines have axial traces that appear to be coaxially refolded (e.g. left, central portion of Fig. 2.8b). Buckling of these axial traces could be misinterpreted as a third phase of folding in the absence of crosscutting cleavages or refolded lineations (Fig. 2.13).

Refolded F_1 hinges show a spread in orientation that is difficult to interpret from the stereograms alone. The equal-area projections of folded F_1 hinges form neither a great-circle distribution expected for shear folding nor a small-circle distribution expected for flexural slip folding (Fig. 2.12c) (Weiss 1959, Ramsay 1967 p. 550). Perhaps the data do not fit either of these end-member models because the F_1 hinges do not rotate as passive lineations (cf. Ghosh 1974). Hinge migration with respect to grid markers is further evidence of non-passive behavior of early fold hinges (Ghosh 1974, Ghosh *et al.* 1993, Grujic 1993). Hinge

Figure 2.13. An interference map pattern (part of Fig. 2.8b) with two interpretations that could be differentiated by cleavage traces (S_1, S_2, S_3) axial planar to each fold generation. (a) Trace of layering (S_o). (b) Interpretation from known surface structure (Fig. 4a). Two phases of folding produce two distinct, nearly orthogonal, axial-planar foliation traces (S_1 and S_2). (c) Cleavage traces if three fold generations formed the same map pattern.

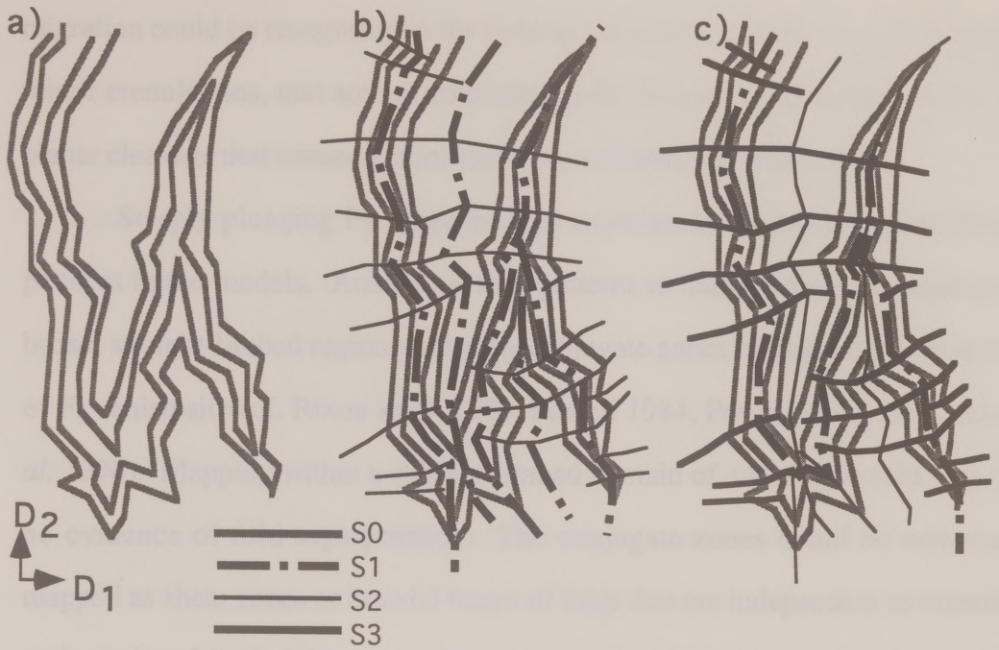
a)
b)
c)
D2
D1
S0
S1
S2
S3

migration could be recognized in the field as lineations, such as veins or the axes of minor crenulations, that are not coincident with the present fold hinge, or by axial planar cleavage that transects refolded F_1 axes (Odonne & Vialon 1987).

Steeply plunging F_2 hingelines are associated with box-style interference patterns in the models. Analogous map patterns in nature would be expressed as broad, straight-limbed regions offset by conjugate zones of high strain, or as kinks of F_1 schistosity (cf. Rixon *et al.* 1983, Powell 1984, Powell *et al.* 1985, Kano *et al.* 1990). Mapping within a straight-limbed domain of a box-style fold may yield no evidence of fold superposition. The conjugate zones could be erroneously mapped as shear zones or as axial traces of folds that are independent in orientation and origin of both fold generations, especially if only one of the zones were exposed. The presence of box-style F_2 folds in plan view could be used to infer a strong anisotropy developed during D_1.

Cuspate-lobate style F_2 folds in plan view show a progressive change in interference style from inner to outer-arc (e.g. model c217, Fig. 2.8c). Grid markers and axes of minor folds fan around the major F_2 axis. In the field, these features correspond to fanning cleavage and radiating minor hinges (cf. variation in "radial" fold orientation, Fig. 1 Julivert & Marcos 1973). The dispersion of D_2 structural elements could be misinterpreted as evidence for additional phases of shortening. This style differs markedly from interference of similar folds where the F_2 fold morphology and orientation is spatially constant (e.g. card-deck models of O'Driscoll 1962, 1964).

The models show variation of fold style with depth. Locally, small Type 1 interference patterns, elongate normal to the D_2 shortening direction, are

superimposed on the crests of larger-wavelength Type 2 patterns (Figs. 2.8b, d). Sections at different depths show that F_1 axial traces change fold style from cuspate to lobate or from single-to-double hinged (Figs. 2.9 & 2.10). In the field, different erosional levels may expose a change from Type 1 to Type 2 interference map patterns or different styles of refolded axial traces or schistosity. Because of such local variation in the interference style, the outcrop-scale fold style does not necessarily represent the regional-scale interference style (Watkinson & Thiessen 1988, Ghosh *et al.* 1993).

The complex interference style of superposed buckle folds seen in the models underscores the necessity of dividing a region into domains with constant fold styles and orientation for analyses of equal-area projections. The projection of fold axes and poles to bedding and the separation of data by domain are well-established techniques for the analysis of polydeformed regions (e.g. Weiss 1959, Ramsay 1967 p.551). This study predicts that data may need to be divided into smaller domains for regions of superposed buckle folds than for superposed passive folds because buckle-fold interference produces more local variation in structural style and orientation (compare domains used to construct stereograms, Figs. 2.4 & 2.11).

CONCLUSIONS

Physical models deformed under conditions of significant gravitational body forces show many of the same features as previous physical models of fold superposition, deformed under conditions of insignificant gravitational body forces. Thus the results are qualitatively comparable to both outcrop and regional-scale

natural fold interference. Gravitational body forces effectively damp the vertical amplitude of both the first and second generation folds, thereby enhancing the formation of Type 2 interference.

Physical models demonstrate that rheology is an important control of fold interference style. For low competence-contrast layering, fold interference is characterized by simple, homogeneous domes and basins. For high competence-contrast layering, dominantly Type 2 fold interference is heterogeneous laterally and with depth. The presence of initially periclinal F_1 folds, box-style F_2 folds with conjugate zones of high strain, minor F_2 folds that fan around major F_2 traces, change in F_2 style from the inner- to outer-arc, and change in F_2 style with depth produce a wide variety of style and orientations of fold interference, which could be mistaken for evidence of more than two fold generations.

Chapter 3. Comparison of Physical Models of Coeval and Superposed Shortening

INTRODUCTION

Folds are commonly assumed to be cylindrical or easily decomposed into cylindrical domains. The geometry of cylindrical folds is described by the orientation of the fold axis and the axial plane and by the profile shape (e.g. interlimb angle, curvature, wavelength, amplitude). For cylindrical folds, the significance of fold style has been well-studied analytically, numerically, and experimentally (e.g. Hudleston 1973, Cobbold 1976, Honea & Johnson 1976, Parrish *et al.* 1976, Smith 1979, Lan & Hudleston 1991). Highly noncylindrical folds are more enigmatic, however, in both their description and interpretation (Williams & Chapman 1980). Noncylindrical folds may form due to a variety of mechanisms: (1) shortening in more than one direction during a single event (e.g. Treagus & Treagus 1981); (2) shearing (Campbell 1958, Wilcox *et al.* 1973, Ghosh & Sengupta 1984); (3) heterogeneous shortening across noncylindrical obstacles or natural boundaries oblique to the shortening direction (e.g. Dubey & Cobbold 1977, Marshak *et al.* 1992, Braun 1993, Marques & Cobbold 1995); (4) gravitational inversion in the case of salt domes and some gneiss domes (Ramberg 1967 p. 87-105); or (5) polydeformation (Ramsay 1962). Previous theoretical, experimental, and field studies of noncylindrical folds have yielded an incomplete set of criteria that would allow their genesis to be inferred from their geometry.

In particular, the dome-and-basin style of fold interference could form in either a single, constrictive event or from the superposition of two non-coaxial phases of shortening (Ramsay 1967 p. 520-521). Such a duality of structural genesis has been demonstrated for domes and basins produced by heterogeneous shear in card deck models (O'Driscoll 1962). For a competent layer buckled in the field of constriction, Ramsay (1967 p. 113) predicted a complex, irregular "crumpling". It is unclear how this structural style would differ from that caused by superposed shortening. If present, foliations could be used to diagnose deformation history: a single foliation would indicate folds produced in a single shortening event, and two foliations would indicate two shortening events (Ramsay 1962). In rocks lacking foliation, however, the relationship between structural style and sequence of shortening remains ambiguous.

In this study, physical models were shortened simultaneously in two orthogonal directions under the same boundary and deformation conditions to determine the differences between coeval and sequential buckle-fold interference.

Previous Analytical Studies of Noncylindrical Folds

Numerical analyses predict different geometries of noncylindrically folded layers with different rheological properties. For an elastic plate in an elastic matrix, simultaneous buckling in two orthogonal directions produces folds with equal arc-lengths in both directions only if the applied stresses are equal in both directions. If the stresses are unequal, cylindrical folds develop with their axial surfaces normal to the direction of greater stress (Ghosh 1970). For the simultaneous buckling of a thin viscous layer in a viscous matrix, the arc-lengths are proportional to the

shortening rates in different orientations (Ghosh 1970). Simultaneous shortening with unequal shortening rates thus forms domes and basins elongate in the direction of the slower shortening rate. Conversely, simultaneous shortening with equal shortening rates in two orthogonal directions yields domes and basins with equal arc-lengths in orthogonal directions. Further, the arc-length produced by coeval, orthogonal shortening is greater by a factor of $\sqrt{2}$ than the arc-length of a fold produced from a single direction of shortening (Ghosh 1970). Fletcher (1991) analyzed the coeval shortening in two orthogonal directions of a *thick* viscous plate. For unequal shortening rates in different directions, the cylindrical perturbation with its axis normal to the direction with the highest shortening rate is preferentially amplified. For equal shortening rates, cylindrical perturbations in different orientations grow at the same rate. Significantly, the noncylindrical, symmetrical "egg-carton" fold form (Ramsay 1967 p. 521) is *not* preferentially amplified. Neither Ghosh's nor Fletcher's analysis includes significant gravitational body forces, so their predictions are valid for folds of wavelengths less than about 100 m (Ramberg 1967 p. 75).

Previous Physical Models of Coeval Fold Interference

Results from previous physical models illustrate some differences between the style of buckle-fold interference of sequentially and coevally shortened materials. Sequential shortening of competent layers resulted in refolded early hingelines and axial surfaces (Ch. 2; Skjernaa 1975, Watkinson 1981, Ghosh *et al.* 1992, 1993, Grujic 1993). Constrictive buckling of a single competent layer resulted in variably trending, shallowly plunging, upright folds with locally curved

hingelines and axial surfaces (Ramberg 1959, Ghosh & Ramberg 1968). Hingelines from adjacent folds locally radiate from a central point (Ghosh & Ramberg 1968). Two-dimensional interference patterns normal to the axis of constriction show closed map patterns with curvature-accommodation folds (Ramberg 1959).

The apparent differences between sequential and coeval buckle fold interference may be the result of the boundary conditions rather than the shortening history. In plan view, previous sequentially shortened models had rectangular boundaries parallel to the shortening directions (Ch. 2; Skjernaa 1975, Watkinson 1981, Ghosh *et al.* 1992, 1993, Grujic 1993), whereas the constrictional models had circular boundaries (Ramberg 1959, Ghosh & Ramberg 1968). Because structural orientation is commonly controlled by the orientation of rigid boundaries, it is not surprising that irregular curvature and radial fold orientation are associated with curved boundaries.

In this study, multilayered models were shortened simultaneously in two orthogonal directions. The models were designed with the same materials, deformation conditions, and rectangular boundary conditions used for the sequentially shortened models described in Chapter 2. Unlike previous analytical and experimental work (Ramberg 1959, Ghosh & Ramberg 1968, Ghosh 1970, Fletcher 1991), these models were deformed with significant gravitational body forces and are thus analogous to km-wavelength folds (Ch. 2).

METHODS

Seven models were shortened coevally in two orthogonal directions. Model materials, number of layers and thickness of the laminate, experimental duration, centrifugal acceleration (in rotation per minute and multiples normal gravitational acceleration), and amounts of shortening parallel to the ram (Dx) and the sidewalls (Dy) are listed in Table 3.1.

Stratigraphy

In a single experiment (c225), stratigraphy with negligible competence contrast was deformed. Stratigraphy consisted of different colored layers of a homogeneous mixture of equal parts DC and PL (Ch. 2). High competence-contrast stratigraphy, represented by alternating layers of the DC and PL, was deformed in the remaining experiments. For all models, a 1 mm layer of DC acted as a weak detachment at the base of each laminate.

A square grid with 5 mm spacing and grid lines parallel to the shortening directions was printed (using the photocopier technique of Dixon & Summers 1985) on the top surface of all the models before deformation. The base and vertical faces of all models were lubricated (National Wax Co., Paxwax 6364-1A) before deformation.

Deformation

Deformation was driven by centrifugal acceleration (Ch. 2). Coeval shortening was achieved by simultaneous movement of three hydraulic rams (Fig. 3.1b). As the dense putty in the reservoir spread, a plastic ram both shortened the model in one direction and displaced faulted Plasticine sidewalls. Shortening of the

Table 3.1 Model Parameters

Coevally shortened models

EXP	Stratigraphy*			Time	rpm	gmax	% Strain		
	materials	layers	h (mm)	(min)			Dx	Dy	Dy/Dx
c225	DC-PL mix	12	3	25.1	2000	940	17	27	1.6
c214	DC & PL	16	3	2.5	2000	940	19	29	1.5
c227	DC & PL	12	3	12.2	2000	940	17	26	1.5
c211	DC & PL	16	5	4.2	2000	940	25	29	1.1
c228	DC & PL	12	3	18.0	2000	940	23	23	1.0
c212	DC & PL	11	5	4.0	2000	940	29	29	1.0
c237#	DC & PL	6	4	30.1	2000	940	26	27	1.0

Sequentially shortened models

EXP	Stratigraphy*			Time	rpm	gmax	% Strain		
	materials	layers*a	(mm)	(min)			D1	D2	D1/D2
c216	DC-PL mix	12	3	30.2	2000	940	36	31	1.2
c217	DC & PL	12	3	94.3	2000	940	44	33	1.3
c235#	DC & PL	6	5	37.5	2000	940	33	24	1.4

h=thickness
*excluding the detachment layer
#models that were CT scanned

Figure 3.1 Schematic setup of deformation apparatus used in the centrifuge. For all models, layering is parallel to the centrifuge's equipotential surface. (a) The centrifuge's rotation axis is normal to the page. The centrifugal acceleration (g) causes dense putty to spread and displace a plastic ram. (b) The centrifuge's rotation axis is parallel to the page. As the plastic ram is displaced, faulted Plasticine sidewalls are extruded in an orthogonal direction. Dy and Dx are reference directions used in subsequent figures.

a) Cross section

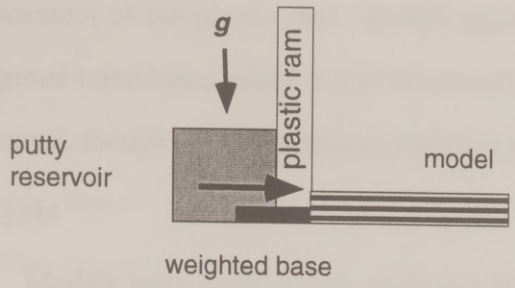

b) Plan view

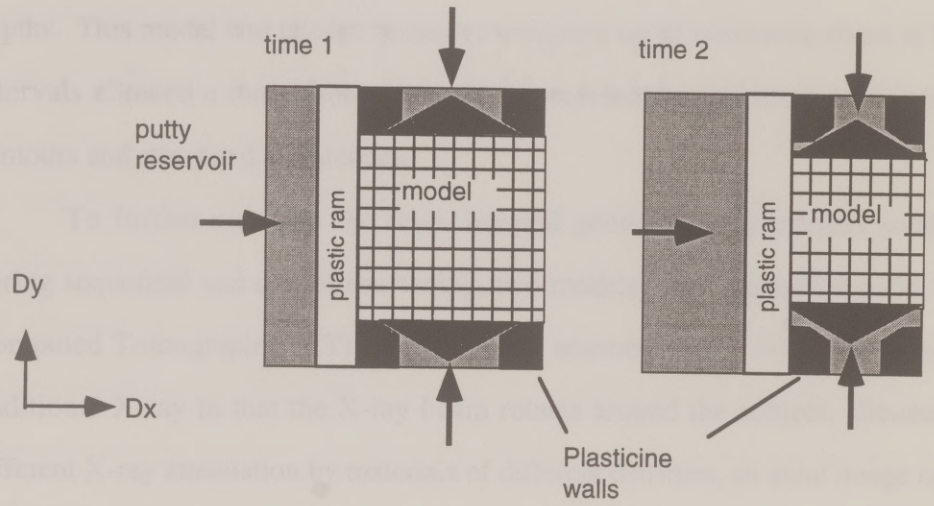

sidewalls caused triangular fault blocks to extrude in a direction perpendicular to the displacement of the plastic ram. In this manner, the model maintained straight, orthogonal boundaries while it was shortened in two directions. The shortening was coeval, though not necessarily at identical strain rates.

Analysis

Models were qualitatively analyzed from photographs (see methodology, Chapter 2). To reconstruct the fold geometry more quantitatively, layer contacts of a representative model (c214) were digitized from photographs taken at successive depths. This model was chosen because a complete set of horizontal slices at 2 mm intervals allowed a more thorough three-dimensional reconstruction of structure contours and structural orientations.

To further compare the final, internal geometry of structures produced during sequential and coeval shortening, two models were scanned in a GE 9800 Computed Tomographic (CT) medical X-ray scanner. A CT scan differs from a traditional X-ray in that the X-ray beam rotates around the subject. Because of different X-ray attenuation by materials of different densities, an axial image can be reconstructed from the cumulative attenuation of each ray-path (Wellington & Vinegar 1987). For this study, a 1.5 mm wide X-ray beam rotated around the model in a vertical plane, perpendicular to the initial model layering. A series of adjacent scans at 1.5 mm intervals was taken for each model. In the resultant images, the Plasticine layers (ρ=1.8 g/cm^3) appear white and silicone putty layers (ρ=1.1 g/cm^3) appear black. The ISG Camra Allegro software package was used to convert the volume of data to planar images in different orientations and to

graphically reconstruct the deformed surfaces. Because the axial scans were adjacent to one another, the software automatically reconstructed planar images with minimal interpolation. Reconstruction of three-dimensional surfaces, however, required manually digitizing the layer contacts in each serial image, and thus required a degree of interpretation. After X-ray imaging was complete, the models were also cut horizontally at 2 mm intervals and photographed.

There are several differences between CT imagery and photography of model sections. The primary advantage of CT image analysis is that it is a non-destructive technique (cf. Coletta *et al.* 1991, Wilkerson *et al.* 1992). Whereas a model is difficult to physically section in more than one orientation, serial X-ray data allow cross sections, map views, and deformed surfaces to be graphically reconstructed and viewed simultaneously. The primary disadvantage of the CT scanning technique is its resolution, approximately 1 mm. The models that were CT scanned were constructed with thicker layers than is ideal, considering the scaling relationships discussed in Chapter 2. Additionally, because the CT value primarily records density contrast, different layers of the same material are locally difficult to correlate, especially in map view. Finally, because the X-ray beam is 1.5 mm in width, the image represents an average CT signal for each x-y coordinate. Consequently, where the layering changes orientation within the 1.5 mm sampled, the image is poorly resolved. The best-resolved images are profiles of locally cylindrical structures.

RESULTS

Experimental Results

Seven models were shortened coevally in orthogonal directions (Table 3.1). Although the models vary in stratigraphy and amount of deformation, all the models formed noncylindrical folds in varying orientations. None of the models formed simple, symmetrical dome-and-basin folds.

Layering with negligible competence contrast (c225, Dx=17%, Dy=27%, Fig 3.2), deformed predominantly by thickening, without the development of surface topography (Fig 3.2a). In the central region of the model, the grid is nearly homogeneously deformed, without a periodic pattern of domes and basins on the surface, or periodic circular interference map-patterns (Fig. 3.2b). Near the corners of the Plasticine sidewalls, surface grid strain is most heterogeneous. Straight-hinged folds that are parallel to the rectangular boundaries formed near the edges. In horizontal section, they are expressed as narrow, elliptical interference patterns. More circular interference shapes superposed on the elliptical shapes indicate that the folds have local culminations and depressions. For all other coeval shortening models, significant competence-contrast layering was deformed.

High competence-contrast layering deformed by buckling in noncylindrical folds (Figs. 3.3 -3.6). Straight-hinged folds initiated near the boundaries. During subsequent shortening, the folds propagated toward the center of the model. Folds with orthogonal trends intersected to form a "log-cabin" pattern, without a consistent orientation of the apparently younger fold set (e.g. Fig. 3.4a). The length of the hingelines tends to decrease from the outer edge to the center of the

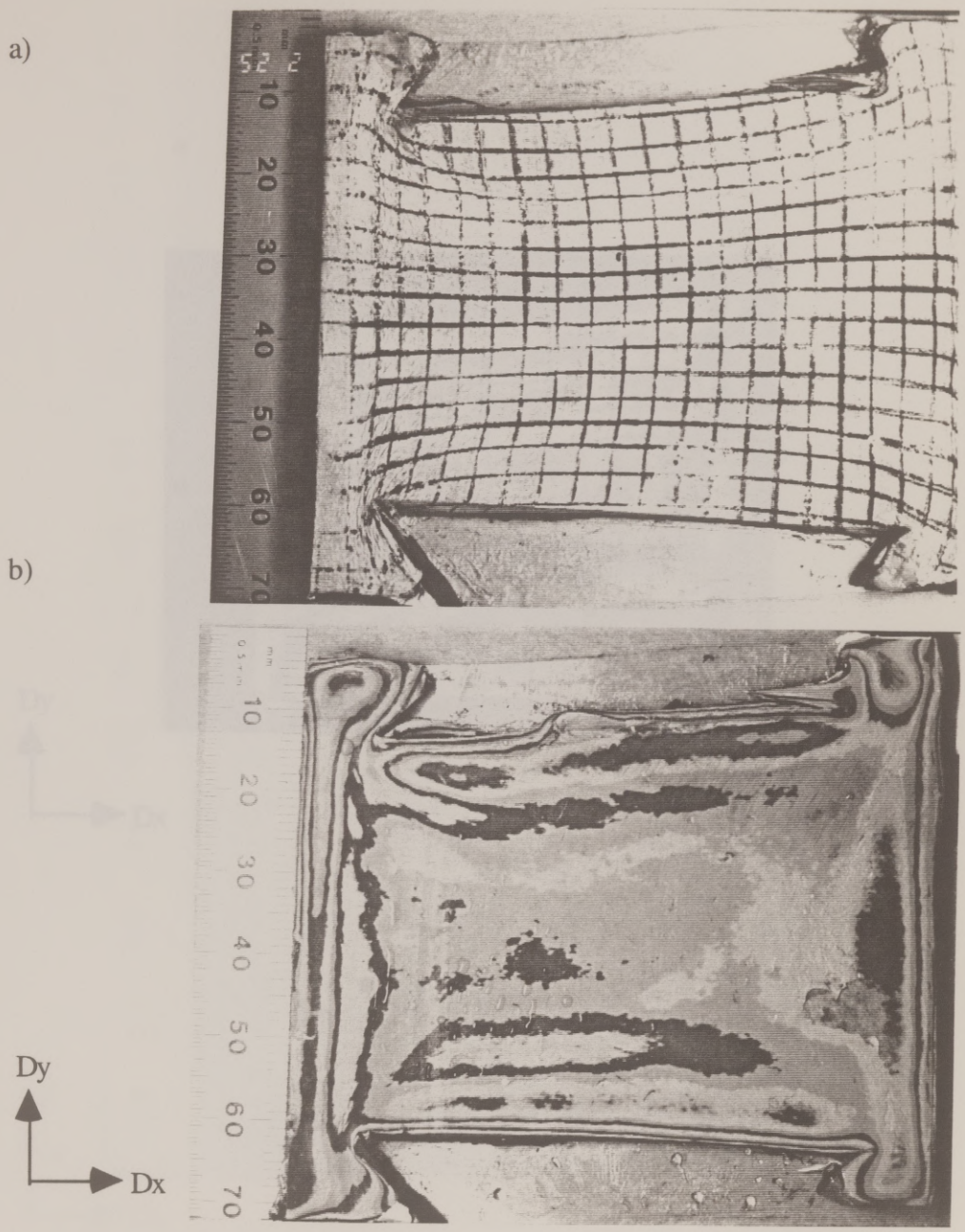

Figure 3.2 Coevally shortened, low competence-contrast (c225, Dx=16.7%, Dy=26.5%). An initially square grid with 5 mm spacing was printed on the model. Scale in millimeters. (a) Top surface. No surface topography developed during shortening. (b) Horizontal section, 2 mm depth. No interference patterns developed in central region of the model.

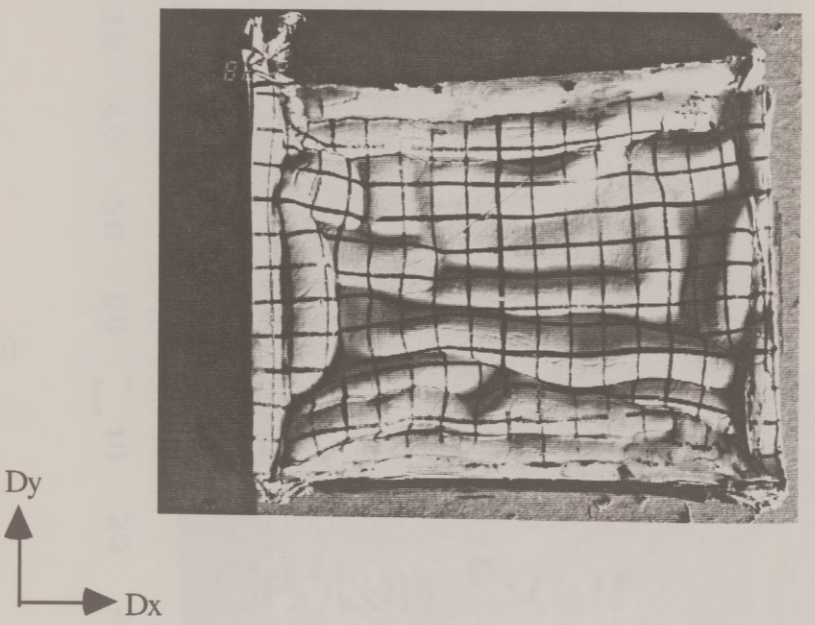

Figure 3.3 Coevally shortened, high competence-contrast (c228, Dx=Dy=23%). An initially square grid with 5 mm spacing was printed on the model. Scale in millimeters. Top surface. Two sets of folds developed parallel to the two shortening directions. Note that some regions of the model are dominated by a single fold set.

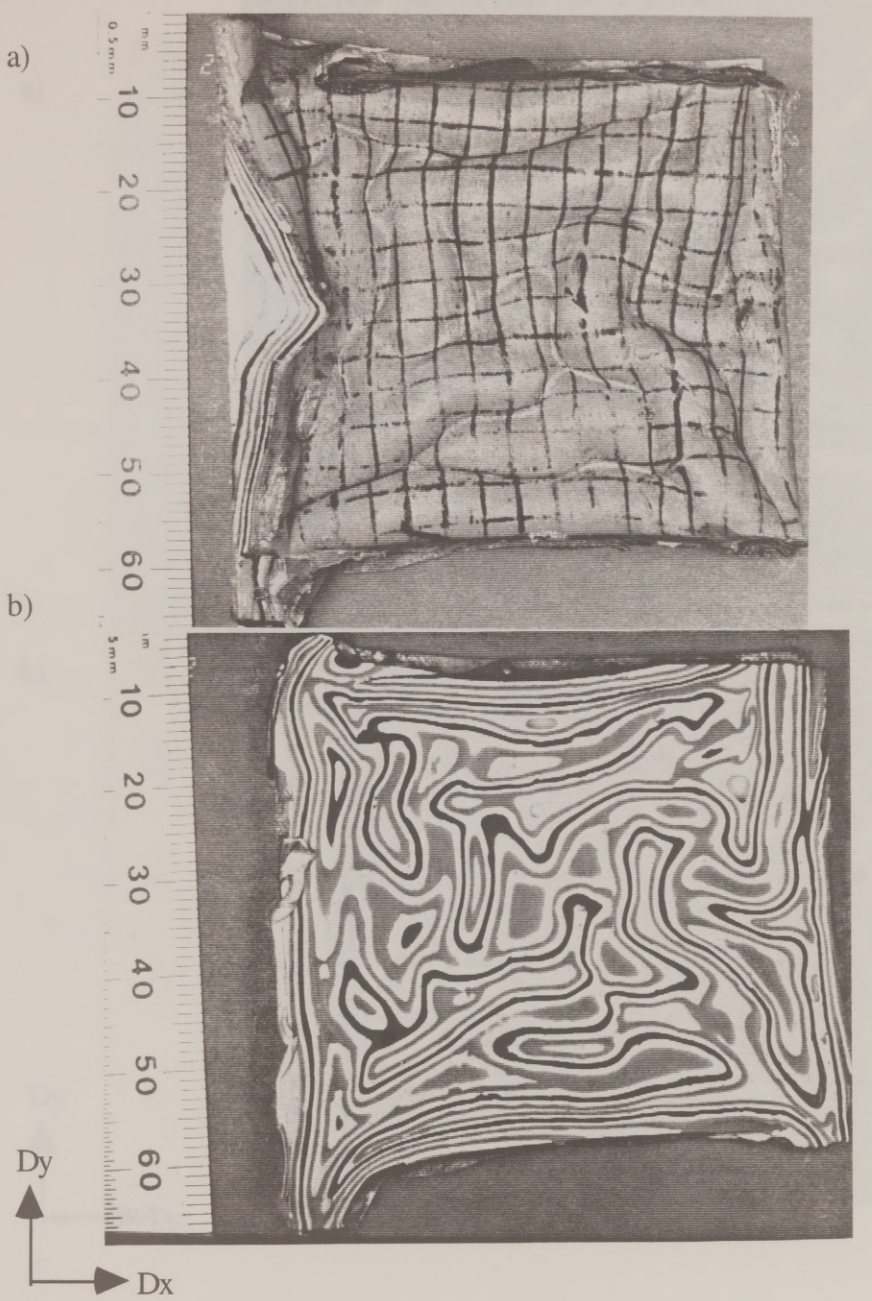

Fig. 3.4 Coevally shortened, high competence-contrast (c212, Dx=Dy=29%). An initially square grid with 5 mm spacing was printed on the model. Scale in millimeters. (a) Top surface. Note that on the left-hand boundary, the laminate deformed by vertical slip along the face of the ram. This anomalous deformation style did not propagate throughout the model. (b) Horizontal section, 10 mm depth.

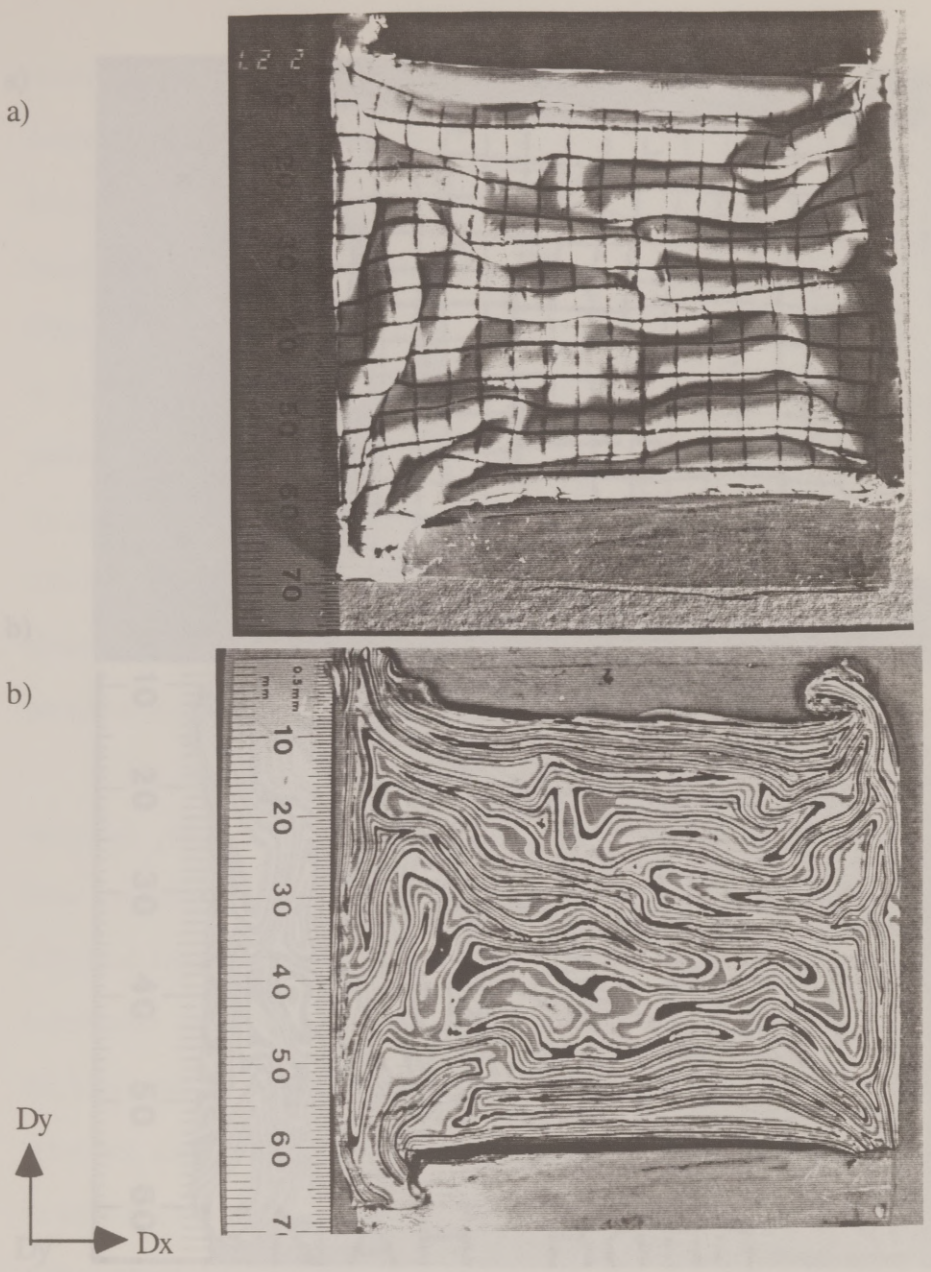

Figure 3.5 Coevally shortened, high competence-contrast (c227, Dx=17, Dy=26%). An initially square grid with 5 mm spacing was printed on the model. Scale in millimeters. (a) Top surface. The folds preferentially trend parallel to Dx. These folds resemble periclines produced by shortening in a single direction (compare with Fig. 2.3a). (b) Horizontal section, 8 mm depth.

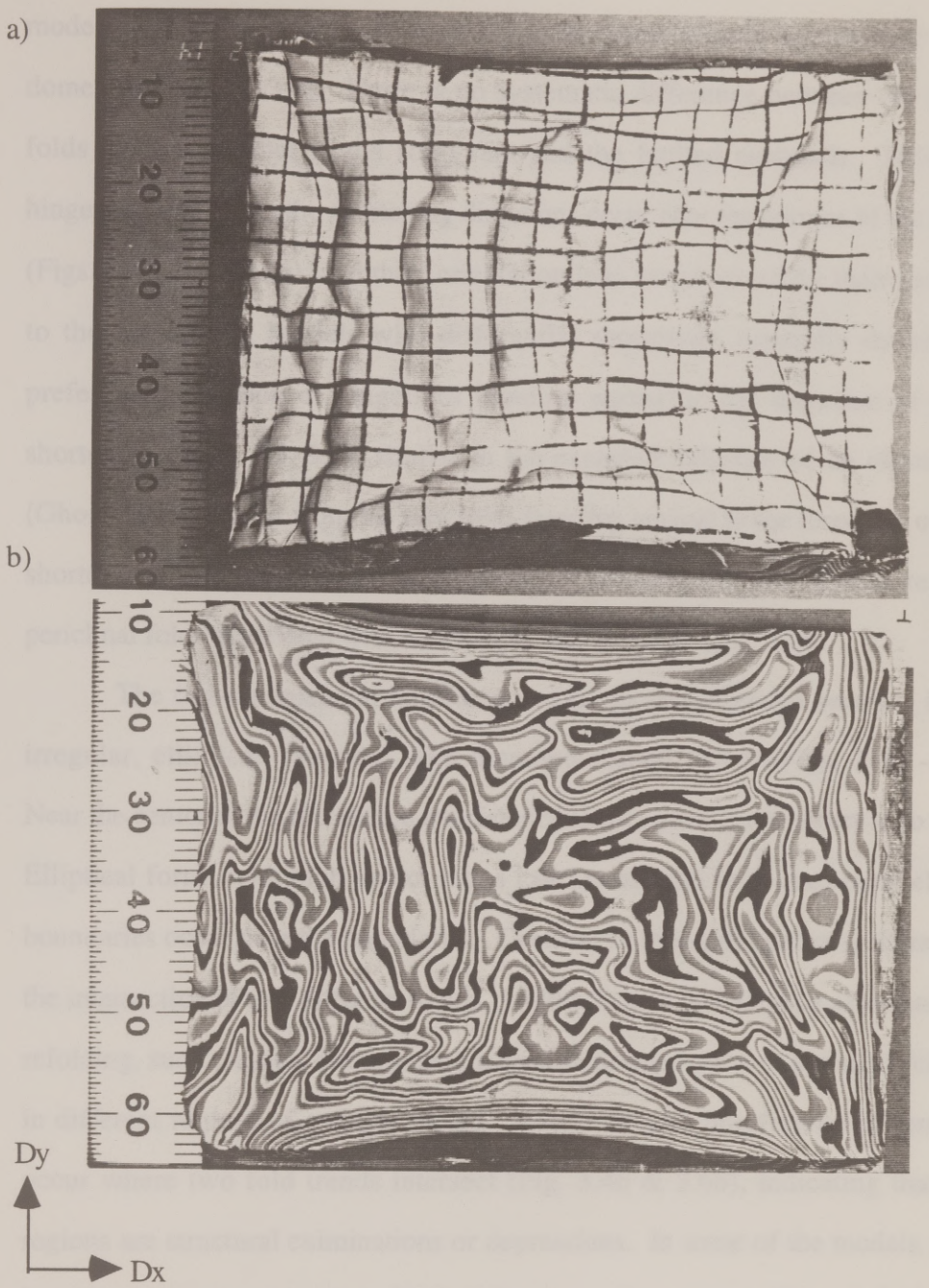

Figure 3.6 Coevally shortened, high competence-contrast (c214, Dx=19, Dy=29%). An initially square grid with 5 mm spacing was printed on the model. Scale in millimeters. (a) Top surface. (b) Horizontal section, 10 mm depth.

model, so that folds in the center of the model more closely approximate equant domes (Fig. 3.4 & 3.6). There is no systematic difference between the style of folds formed parallel to the solid ram and the faulted sidewalls. Folds with hingelines oblique to the shortening directions occur near the corners of the models (Figs. 3.4a, 3.5a, 3.6a), and their orientation may be governed by their proximity to the boundary. Models with differential shortening generally developed a preferred orientation of hingelines trending normal to the direction of greater shortening (Figs. 3.5, 3.6), similar to the expected behavior of an elastic plate (Ghosh 1970). Apart from the rare folds trending normal to the direction of lesser shortening, the structures in the differential-shortening, coeval models resemble periclinal folds associated with buckling in one direction (Fig. 2.6a).

The two-dimensional interference patterns of horizontal sections include irregular, elliptical, crescent-, and diamond-shaped forms (Figs. 3.4b - 3.6b). Near the center of the model, the interference shapes have a low aspect ratio (<2:1). Elliptical forms with high aspect ratios (>4:1) and with long axes parallel to the boundaries occur near the boundaries. Crescent or triangular patterns characterize the intersection of two different trends. Unlike Type 2 interference associated with refolding, such crescent patterns lack a consistent orientation of apparent refolding in different regions of a single model. Nearly circular interference patterns also occur where two fold trends intersect (Fig. 3.4b & 3.6b), indicating that these regions are structural culminations or depressions. In some of the models, closed interference patterns have multiple inflections of curvature (Figs. 3.4b & 3.6b), indicative of curvature-accommodation folding (Lisle *et al.* 1990). Axial traces are gently curved, without a consistent sense of concavity (Fig. 3.7). Hingelines of

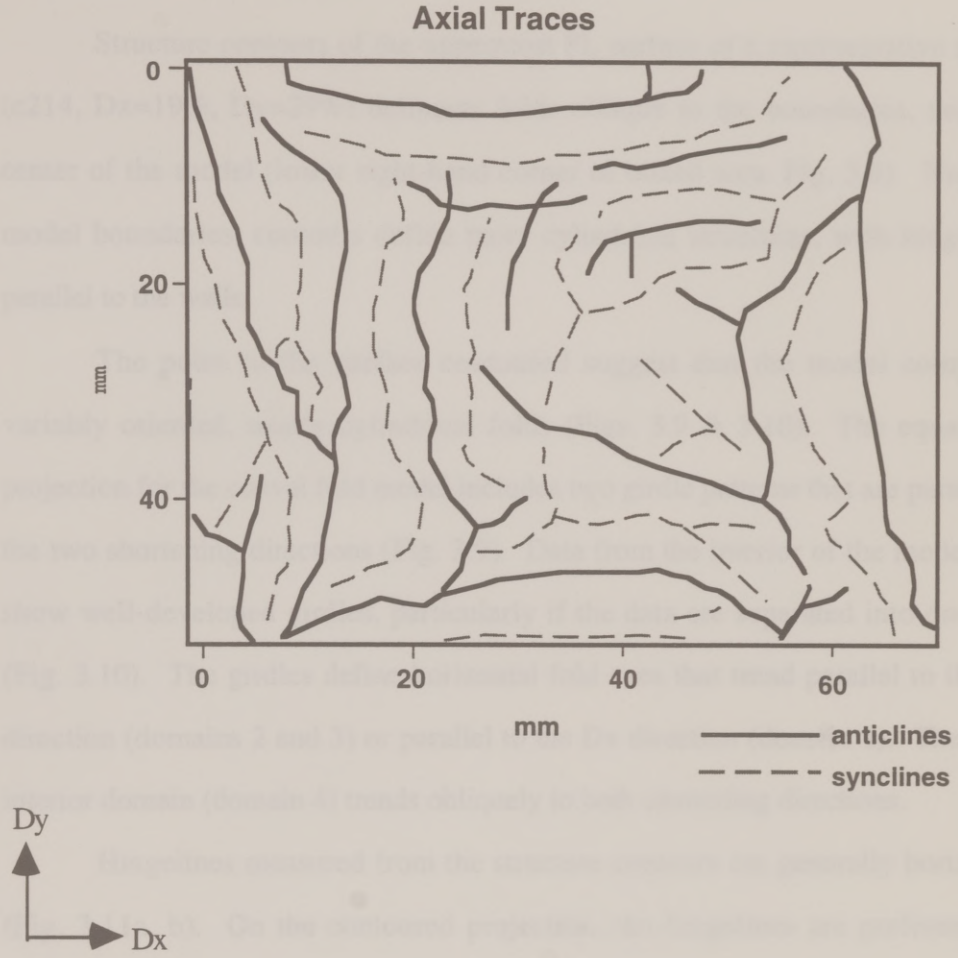

Figure 3.7 Axial traces mapped from the surface contoured in Fig. 3.8a.(c214, Dx=19% Dy=29%).

different orientations intersect at a high angle, in "T" or "Y" shaped patterns. Hingelines do not radiate about a central point.

Structure contours of the uppermost PL surface of a representative model (c214, Dx=19%, Dy=29%) delineate folds oblique to the boundaries, near the center of the model (lower right-hand corner of boxed area, Fig. 3.8). Near the model boundaries, contours define more cylindrical structures, with hingelines parallel to the walls.

The poles to the surface contoured suggest that the model comprises variably oriented, nearly cylindrical folds (Figs. 3.9 & 3.10). The equal-area projection for the coeval fold model includes two girdle patterns that are parallel to the two shortening directions (Fig. 3.9). Data from the interior of the model also show well-developed girdles, particularly if the data are separated into domains (Fig. 3.10). The girdles define horizontal fold axes that trend parallel to the Dy direction (domains 2 and 3) or parallel to the Dx direction (domain 1). The most interior domain (domain 4) trends obliquely to both shortening directions.

Hingelines measured from the structure contours are generally horizontal (Fig. 3.11a, b). On the contoured projection, the hingelines are preferentially oriented parallel to the Dx and Dy shortening directions (Fig. 3.11b). The data maximum is parallel to the Dx direction, normal to the direction of maximum shortening. Unlike the F_1 hingelines of the sequentially folded models (Figs. 2.5c & 2.12c), hingelines of the coevally folded model lack a girdle distribution defined by a spread in hingeline plunge.

Figure 3.8. (a) Structure contours for the uppermost Plasticine layer of model c214. (b) Detail of boxed area in (a). Structural lows (dashed lines) delineate domains plotted in Fig. 3.10

Structure Contours, c214

a)

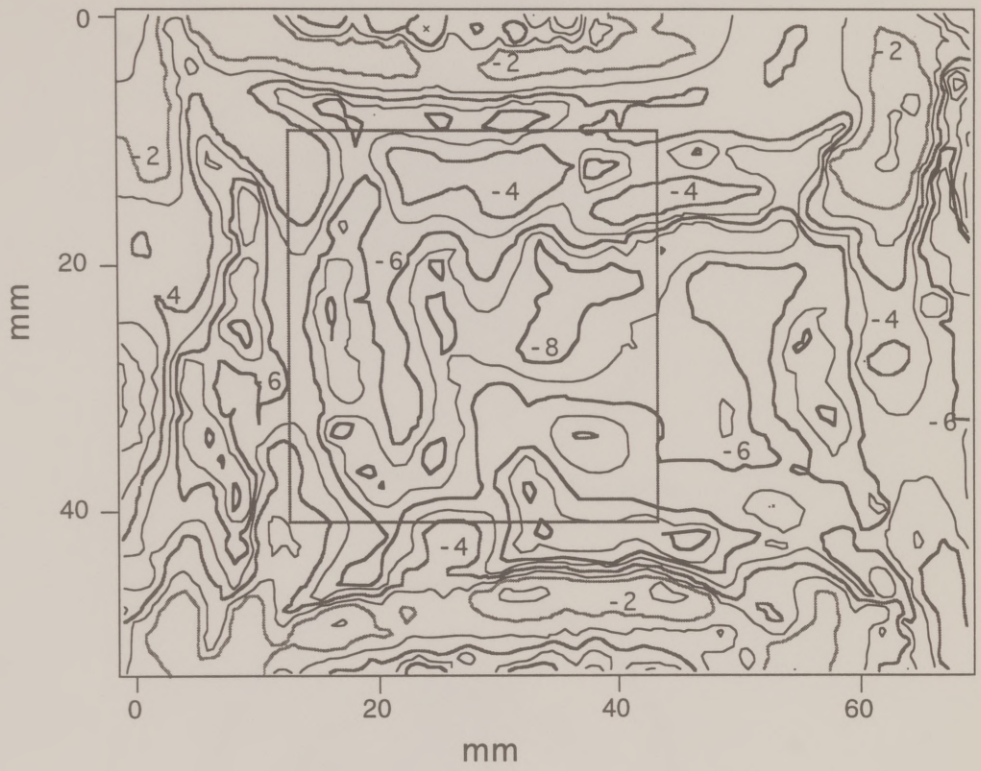

C.I.=1mm, bold contours @ -2, -4, -6, -8 mm

b)

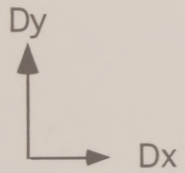

Figure 3.9 Lower-hemisphere, equal-area projections of orientations of the uppermost Plasticine layer of model c214. (a) Poles to layering. (b) Data contoured according to the method of Kamb (1959).

Poles to Layering

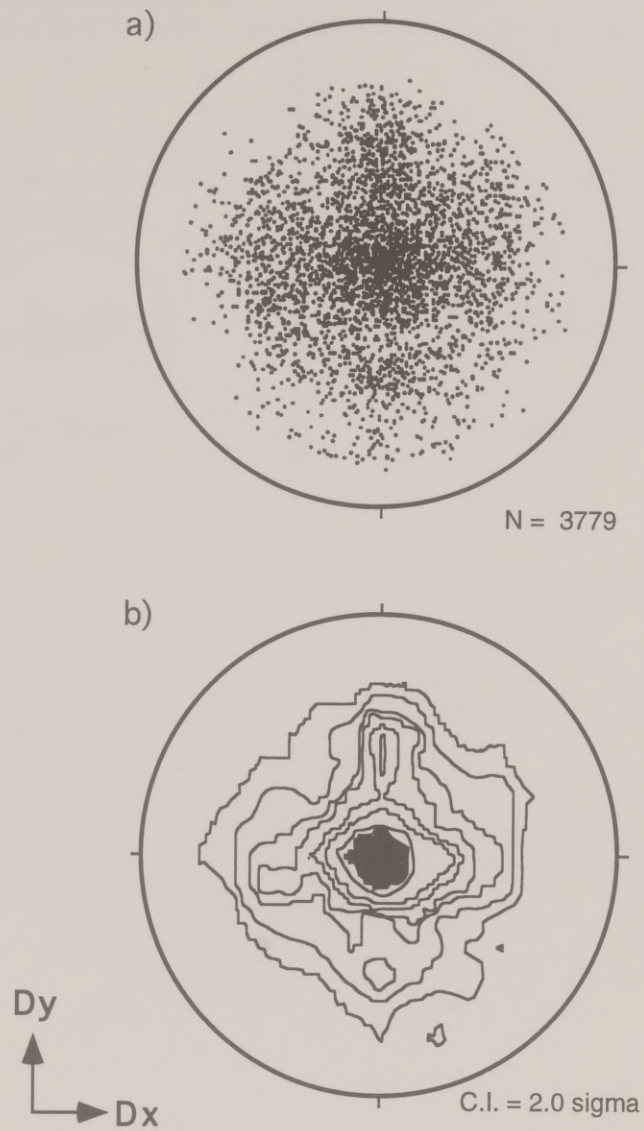

Figure 3.10 Lower-hemisphere, equal-area projections of poles to the uppermost Plasticine layer of model c214. Domains, shown in Fig 3.8b, are separated by major structural lows (dashed lines). Best-fit fold axis to each domain is shown as a box.

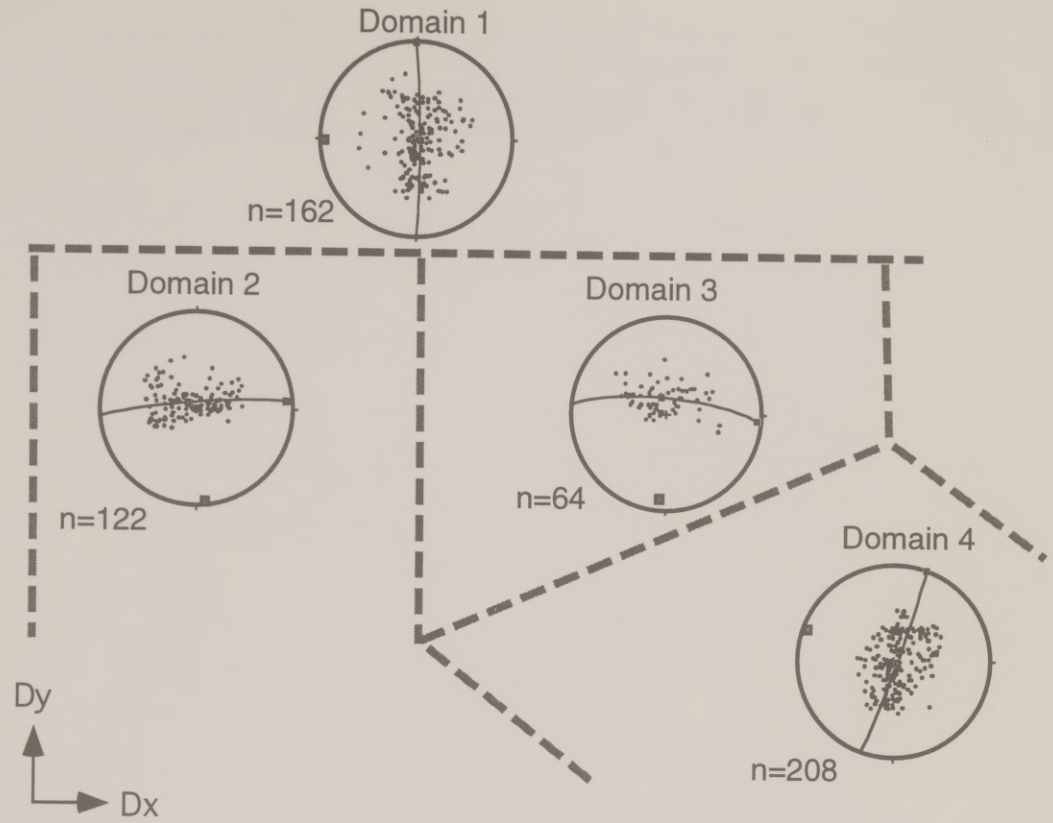
Domain 1
n=162
Domain 2
n=122
Domain 3
n=64
Domain 4
n=208
Dy
Dx

Figure 3.11 Lower-hemisphere, equal-area projections of orientations of anticlinal hingelines, measured from the structure contour map of the uppermost Plasticine layer of model c214 (Fig. 3.8). (a) Hingeline orientations. (b) Data contoured according to the method of Kamb (1959).

Hingeline Orientations

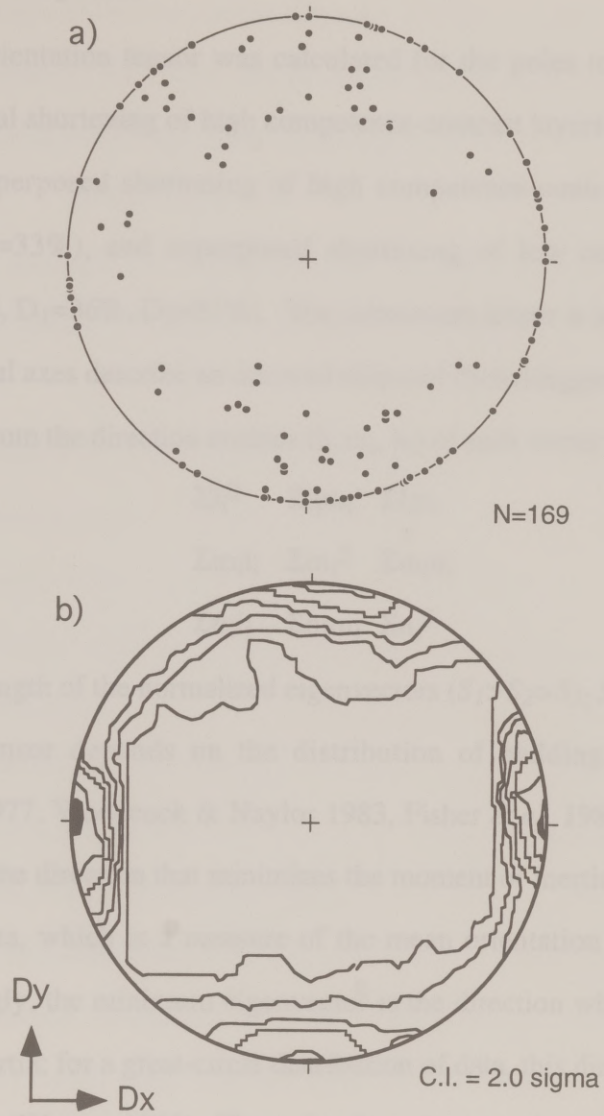

Orientation Ellipsoids

The orientation tensor was calculated for the poles to layering for three models: coeval shortening of high competence-contrast layering (c214, Dx=19%, Dy=29%), superposed shortening of high competence-contrast layering (c217, D_1=44%, D_2=33%), and superposed shortening of low competence-contrast layering (c216, D_1=36%, D_2=31%). The orientation tensor is a second rank tensor whose principal axes describe an oriented ellipsoid (Scheidegger 1965). The tensor is calculated from the direction cosines (l_i, m_i, n_i) of each vector (i) of a population:

$$\begin{matrix} \Sigma l_i^2 & \Sigma l_i m_i & \Sigma l_i n_i \\ \Sigma m_i l_i & \Sigma m_i^2 & \Sigma m_i n_i \\ \Sigma n_i l_i & \Sigma n_i m_i & \Sigma n_i^2 \end{matrix}$$

The relative length of the normalized eigenvectors ($S_1>S_2>S_3$; $S_1+S_2+S_3=1$) of the orientation tensor depends on the distribution of bedding pole orientations (Woodcock 1977, Woodcock & Naylor 1983, Fisher *et al.* 1987). The maximum eigenvalue is the direction that minimizes the moment of inertia of a population of orientation data, which is a measure of the mean orientation of the population. Correspondingly, the minimum eigenvector is the direction which maximizes the moment of inertia; for a great-circle distribution of data, this direction corresponds to the fold axis (Watson 1966). The ratio of maximum to intermediate eigenvalues (S_1/S_2) of each tensor was plotted against the ratio of intermediate to minimum eigenvalues (S_2/S_3) (as summarized by Woodcock & Naylor 1983, Fisher *et al.* 1987, Woodcock 1987). The plot is analogous to the Flinn (1962) diagram for the strain tensor. The statistic

$$K = \ln(S_1/S_2)/ \ln (S_2/S_3) \qquad (3.1)$$

measures the shape of the orientation ellipsoid, and the line K=1 separates the fields representing prolate (K>1) and oblate orientation ellipsoids (K<1) (Woodcock 1987). The ratio of maximum to minimum eigenvalues

$$\xi = \ln(S_1/S_3) \qquad (3.2)$$

represents the strength, or degree of preferred orientation, of a population of orientations (Woodcock 1977). Increased ξ corresponds to a stronger orientation fabric.

These statistics are used to measure fold style. For example, flat-lying layers have a strong point-clustering of bedding-poles on a stereogram. The axial ratios of their eigenvalues would plot in the prolate field (K>>1) on Figs. 3.12a-c. Cylindrically folded layering, which has a girdle distribution on a stereogram, would plot in the oblate field (K<<1). Randomly oriented layering with a nearly uniform distribution on a stereogram would plot near the origin (low ξ). Conical folds are expected to plot in the prolate field. I predict symmetrical, dome-and-basin style folds to project on a stereogram as a diffuse, symmetrical cluster of bedding poles, and their orientation tensors to plot as weakly developed (low ξ) , prolate orientation ellipsoids (K>1). Multimodal data resulting from polydeformation would have isotropic orientation ellipsoids, which plot near the origin (Woodcock & Naylor 1983).

Using the software *Stereonet,* magnitudes of the eigenvectors (S_1,S_2,S_3), trends and plunges of S_3 (the best-fit fold axis), the semi-axes (in degrees) of cones of error for S_1 and S_3, K, and ξ were calculated for the entire gridded surface of

Figure 3.12 Eigenvalue ratios of orientation tensors for three models. Data represent the surfaces contoured in Figs. 2.5, 2.9, 3.8, a region of the surface comprising several domains, or the individual domains. Heavy line, where K=1, separates the fields of oblate and prolate orientation ellipsoids. (a) Superposed shortening, low competence-contrast model (c216, D_1=36%, D_2=31%). All data fall in the prolate field, indicating noncylindrical folds. Domains shown in Fig. 2.5. (b) Superposed shortening, high competence-contrast model (c217, D_1=44%, D_2=33%). Domains can be chosen which fall in the oblate field, indicating cylindrical folds. Domains shown in Figs. 2.9 & 2.10. (c) Coeval shortening, high competence-contrast model (c214 Dx=19% Dy=29%). All data are prolate, but the domains have lower K, indicating a more cylindrical fold style. Domains shown in Fig. 3.8.

Axial Ratios of Orientation Tensors

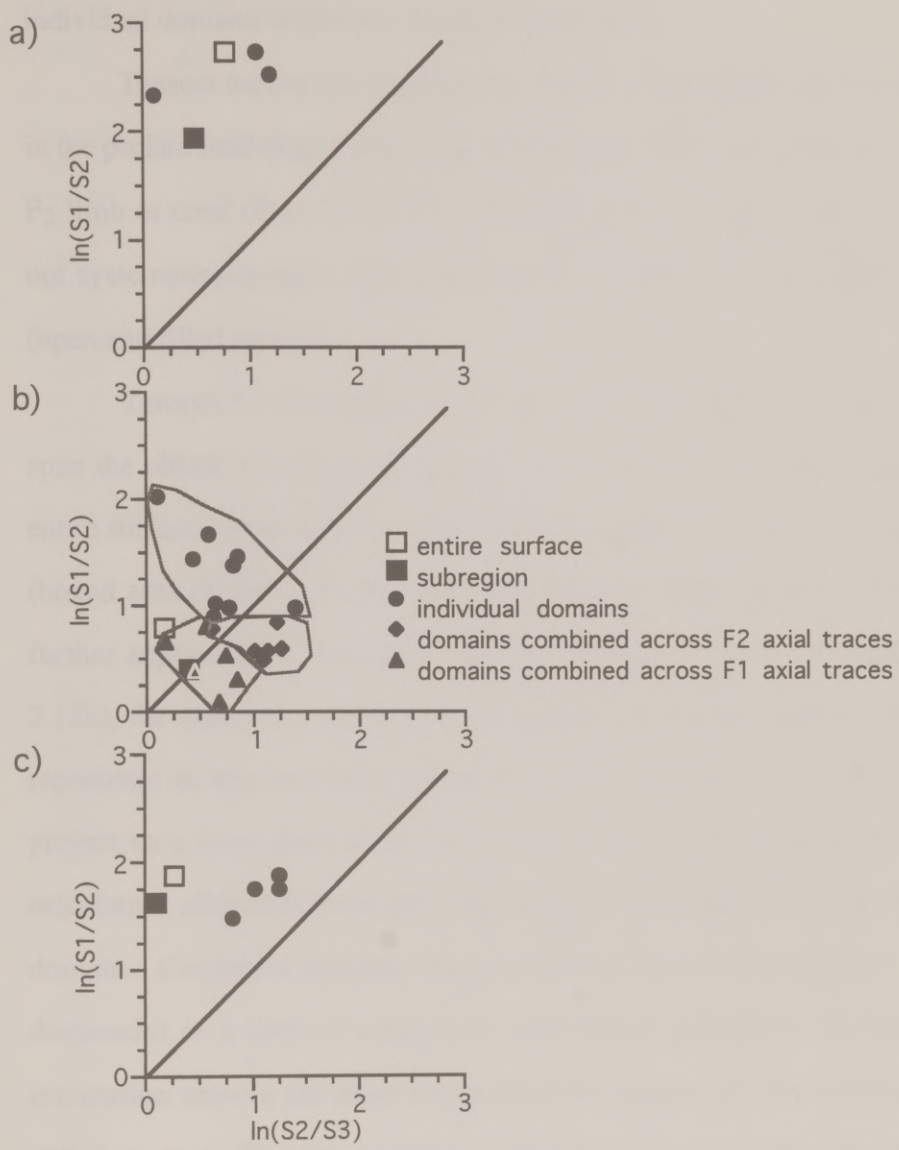

each model, a subregion of each model comprising several domains, and the individual domains within the subregion (Table 3.2).

Tensors for the low competence-contrast, sequentially shortened model plot in the prolate field (Fig. 3.12a). The data from domains represent transects along a F_2 limb or crest (Figs. 2.4 & 2.5). Unexpectedly, the data from F_2 limbs are all not systematically more oblate (lower K) than data from the combined domains (open and filled squares).

Tensors for the high competence-contrast, sequentially shortened model span the oblate and the prolate field (Fig. 3.12b). The tensor calculated for the entire surface (open square) yields a weakly prolate ellipsoid. A subset of the data (boxed area of Fig. 2.11) plots on the line K=1 (filled square). If this subset is further separated into domains bound by F_1 and F_2 axial traces (Fig. 2.11b & 2.12b), the data plot primarily in the prolate field (filled circles). Each domain represents an approximately planar part of a fold limb, so the poles to layering project on a stereogram as a cluster (Fig. 2.12b). The variation in the shape of orientation ellipsoids from different domains is caused by minor folds within a domain. Combined domains represent either a limb of a major F_1 fold (filled diamonds) or a limb of a major F_2 fold (filled triangles). In both cases, the orientation tensors are more oblate than the tensors for the individual domains (filled circles). The data combined across F_2 axial traces are more oblate than the data combined across F_1 axial traces, indicating that the later set of folds is more cylindrical than the early set.

Orientation ellipsoids for the coeval shortening model plot within the prolate field (Fig. 3.12c). The data for the entire surface (open square) yield a strongly

Table 3.2 Eigenvalues of orientation tensors

Exp	domain	n	S1	S2	S3	ln (S1/S2)	ln (S2/S3)	K
Coevally shortenend, high competence contrast								
c214	all	3779	0.726	0.144	0.131	1.62	0.10	16.55
c214	1,2,3,4	557	0.787	0.120	0.093	1.88	0.26	7.17
c214	1	162	0.754	0.171	0.075	1.48	0.82	1.80
c214	2	122	0.817	0.143	0.041	1.75	1.25	1.40
c214	3	64	0.833	0.130	0.037	1.86	1.26	1.48
c214	4	209	0.810	0.140	0.050	1.75	1.03	1.70
Sequentially shortenend, low competence contrast								
c216	all	2499	0.912	0.060	0.028	2.73	0.76	3.60
c216	a, b, c	297	0.812	0.116	0.072	1.95	0.48	4.02
c216	a	99	0.905	0.073	0.022	2.52	1.19	2.13
c216	b	99	0.919	0.060	0.021	2.72	1.07	2.54
c216	c	99	0.844	0.082	0.074	2.33	0.11	20.60
Sequentially shortenend, high competence contrast								
c217	all	2399	0.544	0.247	0.209	0.79	0.17	4.74
c217	1,2,3,4,5,6,7,8,9	684	0.471	0.316	0.213	0.40	0.39	1.02
c217	1	83	0.771	0.147	0.082	1.66	0.58	2.85
c217	2	102	0.799	0.107	0.095	2.01	0.12	17.02
c217	3	87	0.722	0.170	0.108	1.44	0.45	3.18
c217	4	45	0.614	0.252	0.134	0.89	0.63	1.41
c217	5	60	0.679	0.257	0.064	0.97	1.40	0.70
c217	6	52	0.751	0.175	0.074	1.46	0.86	1.70
c217	7	88	0.646	0.242	0.112	0.98	0.77	1.29
c217	8	86	0.731	0.186	0.083	1.37	0.81	1.70
c217	9	74	0.643	0.235	0.122	1.01	0.65	1.54
c217	1&2	186	0.583	0.323	0.091	0.59	1.26	0.47
c217	2&3	191	0.570	0.327	0.103	0.56	1.15	0.48
c217	4&5	105	0.585	0.270	0.145	0.77	0.62	1.24
c217	5&6	112	0.641	0.278	0.081	0.84	1.23	0.68
c217	7&8	174	0.550	0.338	0.113	0.49	1.10	0.44
c217	8&9	160	0.565	0.320	0.115	0.57	1.02	0.56
c217	1&4	128	0.586	0.263	0.151	0.80	0.56	1.43
c217	2&5	163	0.535	0.315	0.150	0.53	0.74	0.71
c217	4&7	134	0.509	0.269	0.222	0.64	0.19	3.26
c217	5&8	147	0.469	0.324	0.207	0.37	0.45	0.83
c217	6&9	127	0.419	0.385	0.196	0.09	0.68	0.13
c217	3&6	140	0.484	0.361	0.155	0.29	0.85	0.35

Table 3.2 (continued)

Exp	domain	S1/S3	ξ	S1 error cones max1	S1 error cones min1	S3 error cones max 3	S3 error cones min3	T3	P3
Coevally shortenend, high competence contrast									
c214	all	5.56	1.716	1.1	1.0	20.9	1.0	103	2
c214	1,2,3,4	8.51	2.141	2.5	2.1	21.1	2.1	107	0
c214	1	10.03	2.306	6.2	3.40	11.8	3.3	270	3
c214	2	19.91	2.991	6.0	2.8	9.7	2.6	175	6
c214	3	22.58	3.117	7.3	3.7	13.7	3.7	185	14
c214	4	16.23	2.787	4.5	2.5	8.1	2.4	290	4
Sequentially shortenend, low competence contrast									
c216	all	32.58	3.484	7.0	0.5	3.4	0.5	77	12
c216	a, b, c	11.34	2.429	3.2	2.2	14.9	2.2	270	3
c216	a	40.97	3.713	3.5	2.2	11.5	2.2	3	13
c216	b	44.39	3.793	3.1	2.2	10.6	2.1	178	3
c216	c	11.47	2.440	4.6	4.1	*	*	163	29
Sequentially shortenend, high competence contrast									
c217	all	2.61	0.958	3.0	2.5	14.6	2.5	199	3
c217	1,2,3,4,5,6,7,8,9	2.21	0.792	11.3	5.0	10.7	5.0	91	30
c217	1	9.38	2.238	6.9	5.3	24.5	5.1	82	28
c217	2	8.42	2.131	5.3	5.0	*	*	112	21
c217	3	6.68	1.899	7.0	6.0	34.2	5.9	80	28
c217	4	4.58	1.522	19.1	10.4	30.1	10.4	310	19
c217	5	10.68	2.369	15.7	5.2	11.8	5.2	245	42
c217	6	10.09	2.312	10.1	5.5	19.7	5.4	288	49
c217	7	5.75	1.749	*	*	*	*	119	48
c217	8	8.79	2.174	8.5	4.5	22.0	4.6	61	50
c217	9	5.25	1.658	13.7	8.3	22.2	8.2	94	30
c217	1&2	6.39	1.854	14.3	4.8	6.2	4.8	93	34
c217	2&3	5.52	1.708	14.7	5.2	6.8	5.2	92	35
c217	4&5	4.04	1.397	14.9	7.2	16.7	7.1	278	29
c217	5&6	7.91	2.068	12.2	4.5	9.2	4.4	257	43
c217	7&8	4.88	1.585	17.2	4.9	9.0	5.0	92	43
c217	8&9	4.90	1.588	14.0	5.5	10.0	5.5	94	36
c217	1&4	3.90	1.360	11.4	7.4	18.2	7.3	64	8
c217	2&5	3.57	1.274	12.2	6.3	15.1	6.2	313	6
c217	4&7	2.30	0.831	14.8	12.0	56.6	12.1	77	22
c217	5&8	2.26	0.815	17.8	11.3	26.1	11.2	313	4
c217	6&9	2.14	0.763	*	*	*	*	223	11
c217	3&6	3.13	1.141	24.8	7.9	12.7	7.9	223	13

* not enough data to calculate error cone axes

n number of data points

S eigenvalue

K [ln(S1/S2)]/[ln(S2/S3)]

ξ ln (S1/S3)

T3 trend of S3 (calculated fold axis)

P3 plunge of S3

prolate ellipsoid. A data subset from the central region of the model (Fig. 3.8b) also plots in the prolate field (filled square). Domains, which are anticlines separated by structural lows (Fig. 3.10), plot within the prolate field. Individual domains are more oblate (lower K) and have stronger orientation fabrics (higher ξ) than the combined data. Thus the apparently noncylindrical fold style of the central region of the model can be divided into domains of more cylindrical folds.

For all three models, data for the entire surface plot within the prolate field, confirming that all of the fold styles are noncylindrical (compare Figs. 3.12a, b, c). The coevally shortened model has the highest value of K, indicating the least cylindrical fold style. Evidently, the intersection of the two girdle distributions (associated with the two dominant fold sets) yields a strong point-clustering of poles to layering (Fig. 3.9). The sequentially shortened, low competence-contrast model has the highest value of ξ because the low limb dips in the model allow little spread in orientation of bedding poles (Fig. 2.5a). The sequentially folded, high competence-contrast model has the lowest value of ξ, indicating the most random orientation fabric, as predicted. The low ξ value is the result of complex refolding of bedding, which obscures original F_1 cylindricity.

In sum, eigenvector analysis helped identify the model with the most random orientation fabric, which resulted from the superposed shortening of high competence-contrast layering (open square, Fig. 3.12b). Eigenvector analysis also identified the region that most closely approximated cylindrical folding, which occurred in the same model, where domains were bounded by F_1 axial traces. These results confirm that the interpretation of structurally complex areas requires

data to be divided into domains bounded by structurally significant elements (cf. Turner and Weiss 1963 p. 175).

Eigenvector analysis illustrates some of the differences in fold styles between the models. Eigenvalue plots, however, could not be used to uniquely identify either the shortening history or rheology of the models. This type of analysis is better used as a quantitative measure of fold geometry, for comparing different data sets, than as a determinant of fold mechanism or of deformation history.

CT X-ray Images

Coevally and sequentially shortened models that were CT-scanned had relatively thick layers, but they deformed with the same general structural styles as more finely laminated models (c235, D_1=33%, D_2=24%, Fig. 3.13; c237, Dx=26%, Dy=27%, Fig. 3.14, Table 3.1, Table 3.3). Folds of the thickly layered models, however, had greater wavelength, fractured more commonly, and had more pronounced boundary effects. CT images away from the boundaries allowed the measurement of average thickness of the laminate and arc-length of fold profiles (Table 3.3, Figs 3.15 and 3.16).

CT scans show several features not recognized by previous analytical techniques. The sequentially folded model fractured more commonly than did the coevally folded model (compare Figs. 3.15 & 3.16). More abundant fracturing may have been caused by the greater D_1 shortening for the sequentially shortened model than for either direction of shortening of the coevally shortened model. Fractures are preferentially located in the F_1 hinge zones (3.15a). F_1 folds have

Table 3.3 Measurements from CT images

		%strain	L	s	w	s	h	s	A	s
c235	D1	33.00	16.50	3.14	12.42	3.13	4.99	0.83	2.74	0.45
c235	D2	24.00	15.30	4.71	10.42	4.62	6.32	1.29	2.17	0.56
c237	Dx	26.00	13.62	2.78	10.90	2.55	4.42	0.44	1.44	0.38
c237	Dy	27.00	10.40	4.11	10.40	4.11	4.77	0.84	0.72	0.19

all measurements in mm
L = mean arc-length
w = mean wavelength
h = mean thickness of laminate (excluding detachment)
A = mean amplitude
s = standard deviation

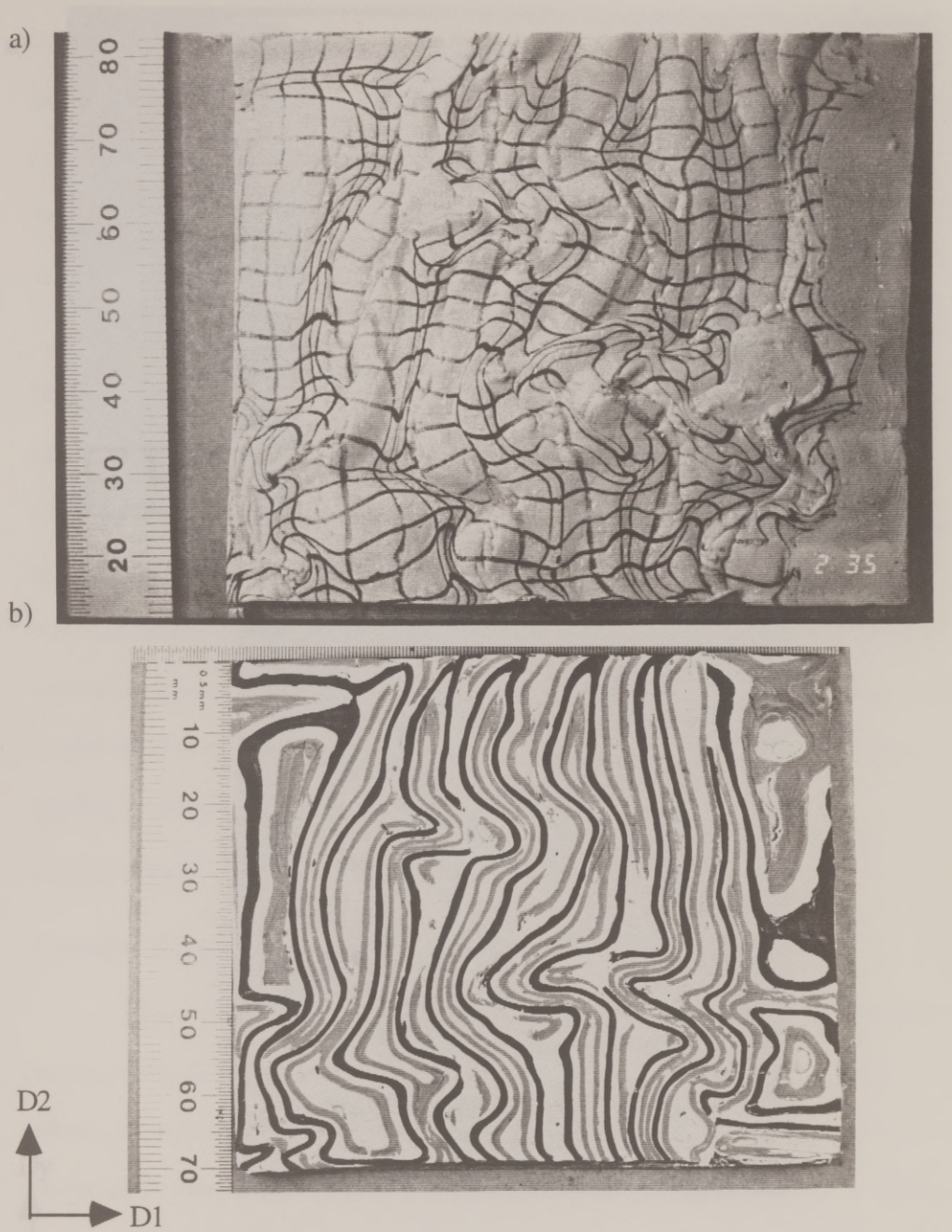

Figure 3.13 Photographs of the sequentially shortened, high competence-contrast model that was CT scanned (c235, D_1=33%, D_2=24%). An initially square grid with 5 mm spacing was printed on the model. Scale in millimeters. (a) Top surface. Laminate inserted between D_1 and D_2 is located near the right-hand boundary, and lacks grid. (b) Horizontal section, 10 mm depth.

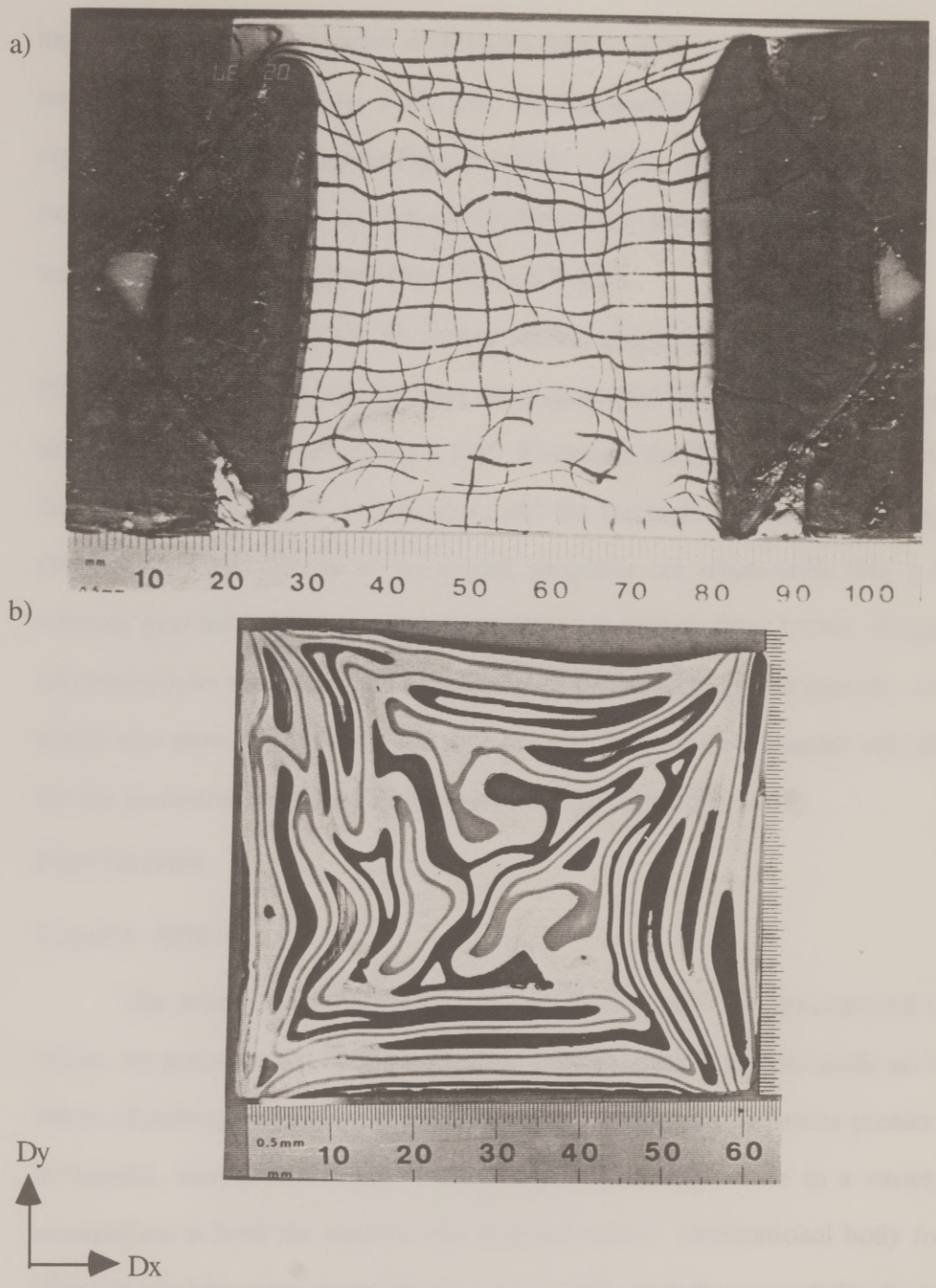

Figure 3.14 Photographs of coevally shortened, high competence-contrast model that was CT scanned (c237, Dx=26%, Dy=27%). An initially square grid with 5 mm spacing was printed on the model. Scale in millimeters. (a) Top surface. (b) Horizontal section, 10 mm depth.

longer wavelengths and higher amplitudes than do folds of the coevally shortened model (Figs. 3.15a and 3.16, Table 3.3). Profiles parallel to the D_2 direction lack a regular periodicity (compare Figs. 3.15a & 3.15b). In the coevally shortened model, the fold profiles in orthogonal directions show little difference in fold wavelength or style (compare Figs. 3.16a & 3.16b).

For the sequentially shortened model, graphical reconstructions of the Plasticine surfaces show that fractures are concentrated in the anticlinal hinge zones, and the fractures are curved (Fig 3.17a). Evidently, the Plasticine layers fractured during an early stage of deformation, and the fractures were folded during D_2 shortening. Near the top of the model, anticlines are lobate-style (Fig 3.17a), whereas near the base of the model anticlines are cuspate (Fig. 3.17b). Graphical reconstructions of the top and bottom Plasticine surfaces of the coevally folded model also show that the anticlinal style changes from lobate to cuspate with depth, but the reconstructions show little evidence of fracturing (Fig. 3.18).

DISCUSSION

Gravity Effects

The results from this study, which included significant gravitational body forces, are generally similar to results from previous studies with insignificant body forces (Ramberg 1959, Ghosh & Ramberg 1968). These similarities predict that horizontal, coeval shortening would produce horizontal folds in a variety of orientations at both the outcrop and regional scales. Gravitational body forces likely damped the vertical amplification of the folds, as in the sequentially shortened models (Ch.2), thereby accentuating the change in fold style with depth (Figs. 3.17

Figure 3.15 Vertical profiles through sequentially shortened model (c235, D_1=33%, D_2=24%). Each division in scale equals one cm. Inverse image, so PL appears black and DC appears light. (a) CT axial scan, parallel to the D_1 direction. (b) Graphical reconstruction of profile normal to the CT scan, parallel to the D_2 direction. (c) Map view graphical reconstruction of model c235. Solid lines mark the position of profiles in Fig. (a) and (b). Laminate inserted between D_1 and D_2 marked with "L".

a)

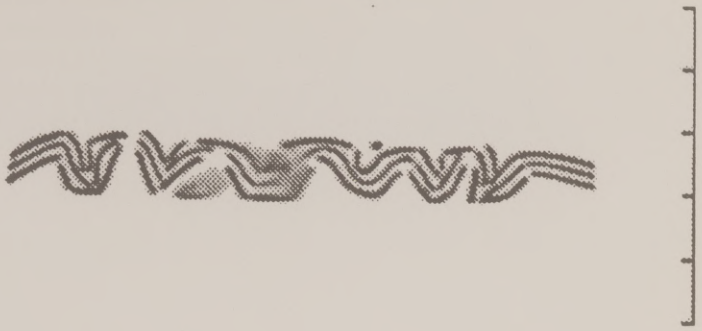

b)

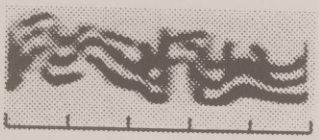

c)

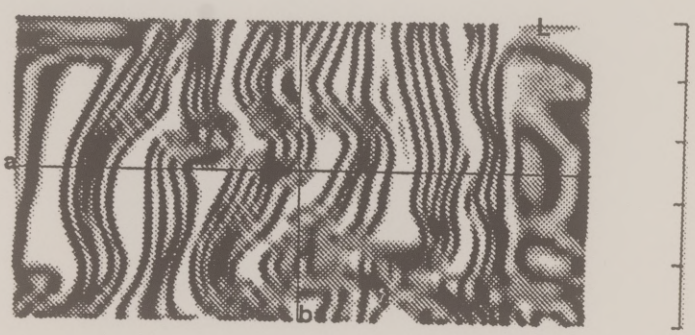

Figure 3.16 Vertical profiles through coevally shortened model (c237, Dx=26%, Dy=27%). Inverse image, so PL appears black and DC appears light. Each division in scale equals one cm. (a) CT axial scan, parallel to the Dx direction. (b) Graphical reconstruction of profile normal to the CT scan, parallel to the Dy direction. (c) Map view graphical reconstruction of model c237. Solid lines mark position of profiles in (a) and (b).

a)

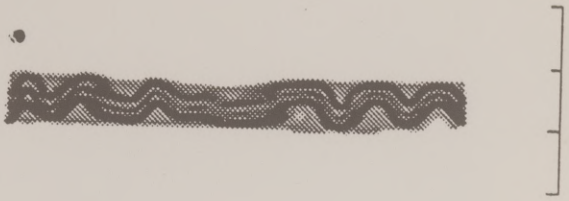

b)

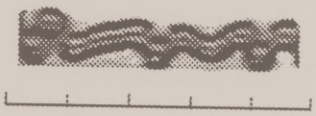

c)

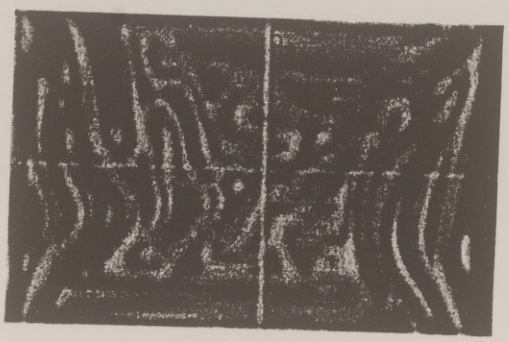

Figure 3.17 Graphical reconstruction from serial CT scans of deformed Plasticine layers for the sequentially shortened model (c235). Light source is from the upper left. (a) Plan view of the top of the uppermost Plasticine surface. Note the curved fractures in the crests of the anticlines. (b) Plan view of the top of the bottom Plasticine surface. Note the change in style between lobate anticlines in (a) and cuspate anticlines in (b).

a)

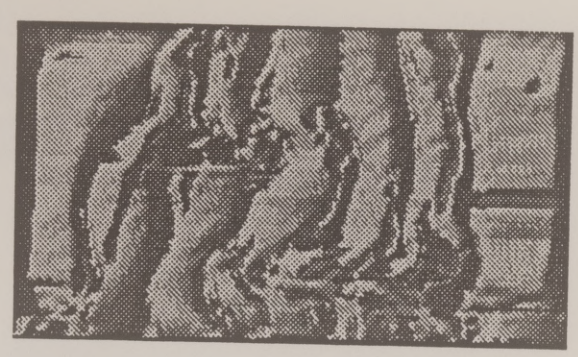

b)

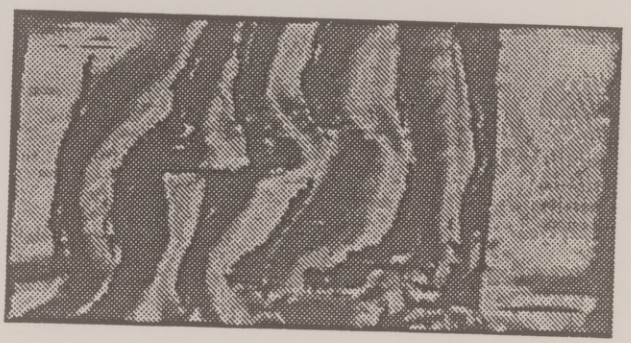

Figure 3.18 Graphical reconstruction from serial CT scans of Plasticine layers from a coevally shortened model (c237) Light source is from the upper left. (a) Plan view of the top of the uppermost Plasticine surface. Note the curved fractures in the crests of the anticlines. (b) Plan view of the top of the bottom Plasticine surface. Note the change in style between lobate anticlines in (a) and cuspate anticlines in (b).

a)

b)

& 3.18). Additionally, the vertical damping of folds may have constrained the plunge of the fold hingelines. Accordingly, coeval shortening may produce regional-scale folds with predominantly horizontal hingelines and outcrop-scale folds with more variable plunge. Such a direct dependence of fold style on scale, however, is poorly supported by the comparison of structures in this study and previous studies (Ramberg 1959, Ghosh & Ramberg 1968). Experimental variables other than gravity, such as boundary conditions, better account for the differences in fold style between this study and previous work.

Boundary Effects

The location and shape of the model boundaries influenced the orientation, amplitude, and location of the structures. The folds have greatest amplitude near the boundaries (Fig. 3.8), and the fold hingelines have a preferred orientation parallel to the boundaries and the shortening directions (Figs. 3.7, 3.11). In the center of the models, the interference patterns have the most equant shape and are oriented obliquely to the shortening directions. Comparison of the generally orthogonally oriented hingelines in coeval folds of this study with the radial hingelines of constrictively shortened models with circular boundaries (Ramberg 1959, Ghosh & Ramberg 1968) further demonstrates the strong influence of boundary shape on fold orientation. The effects of near-field, rigid boundaries are neither ideal nor entirely artificial, given that natural structures do depend on the presence and orientation of natural boundaries such as continental margins or preexisting basement structures. Despite the effect of the rigid boundaries in the present study, the shape and orientation of boundaries were the same for the

coevally shortened models and the sequentially shortened models. Therefore, the boundary effects do not cause the principal differences between their fold interference styles.

Comparison of Coevally and Sequentially Shortened Models

The low competence-contrast, coevally shortened model deformed primarily by thickening. Lack of surface topography, minor surficial grid strain, and simple, non-periodic interference map patterns away from the boundaries are evidence for deformation by layer-parallel shortening rather than buckling. Although the materials were identical to those used in some of the sequentially shortened models (c216, Fig. 2.3), the rheologic interfaces between the detachment unit, the laminate, and free upper-surface did not buckle during coeval shortening. Where rheologic contrast is subtle, buckling is evidently favored by plane strain, a condition approximated by D_1 shortening of the sequentially shortened models.

High competence-contrast, coevally shortened models deformed into nearly horizontal folds with straight to gently curved hingelines in variable orientations. None of the models is characterized by symmetrical, open domes and basins. Thus a multilayer with high competence-contrast accommodates coeval shortening differently from heterogeneous sheared card-deck models (O'Driscoll 1962) and from a thin viscous plate (Ghosh 1970). Broad anticlines and tight synclines suggest a lobate-cuspate fold style that is consistent with buckling mechanism (Fig. 3.16). Models with differential shortening (and model c228 with equal shortening) in different directions show a preferred orientation of fold hingelines, consistent

with predictions for the coeval shortening of an elastic plate (Ghosh 1970) and for a thick viscous plate (Fletcher 1991).

Sequential and coeval shortening produced distinct structural styles. Unlike the sequentially shortened models, coevally shortened models developed no tightly refolded hingelines or axial surfaces. Instead of the non-plane, noncylindrical folds (Turner & Weiss 1963 p.109) produced by sequential shortening, coeval shortening tended to produce plane, noncylindrical to cylindrical folds in various orientations (Fig. 3.10 and 3.12).

The structures in the coevally shortened model most closely resemble the sequentially shortened model with low D_1 shortening (c222, Fig 2.7). In both cases, some domains of the model are dominated by fold sets of a uniform orientation, and crescent-shaped interference patterns occur at the intersection of different fold sets. In the sequentially shortened model, however, there are also domains where the F_1 hingelines, axial traces, and axial surfaces are folded (Fig. 2.7c). The same sequence of refolding and orientation of younger structures occurs in different domains throughout the model. Regionally consistent overprinting relationships can thus be used to differentiate sequential from coeval shortening, even where the degree of shortening is relatively low.

Some domains of the coevally shortened models are similar to sequentially shortened models with >20% D_1 shortening (Fig. 2.8). The coevally folded models have gently curved hingelines and map-view interference patterns shaped like broad crescents (Figs. 3.4 - 3.7). Such curvature is caused by the refolding of early hingelines during progressive shortening in two directions. Apparent curvature of the hingelines also occurs where folds of different trends intersect (cf.

Ghosh and Ramberg 1968). Because the rams moved in different directions and with different strain rates, however, folds with curved hingelines show a regionally inconsistent orientation of refolding (Fig. 3.7).

The hingeline orientations of the coevally shortened models vary in trend within an approximately horizontal plane (Fig. 3.11). To a first order approximation, equal-area projections hingelines of the coevally shortened model resemble the refolded F_1 hingelines of the sequentially shortened model (Fig. 2.12c). Those of the coeval model could be mistaken for hingelines refolded about a vertical axis. Separation of the hingelines into domains, however, demonstrates that F_1 hingelines change orientations systematically across sets of subparallel F_2 axial traces (Fig. 2.12d). For the coeval model, the best-fit fold axes change orientations across variably oriented domain boundaries (Fig. 3.10). Dividing the data into domains aids the differentiation of hingelines reoriented by a single direction of superposed shortening from hingelines that nucleated in variable orientations during coeval shortening in more than one direction.

The different fold styles in profile indicate that the coevally and sequentially shortened models accommodated the imposed strain differently. In the sequentially shortened models, tight F_1 fold profiles and fractures in the F_1 hinge zones (Fig. 3.15a) demonstrate that strain was concentrated in the hinge zones of the F_1 folds. Most pronounced fracturing is present where F_2 folds have the maximum curvature (Fig.3.19a), the predicted locus of maximum superposed strain (Ghosh 1974). Fewer fractures and the more open, rounded folds in the coevally shortened models are evidence that strain was more homogeneously distributed than in the sequentially shortened models (3.16a). Mean arc-length and fold amplitudes are

smaller for the coevally shortened model than for F_1 profiles of the sequentially shortened model (Table 3.3), inconsistent with Ghosh's (1970) calculation for a thin viscous layer. Multiple inflections of curvature in map-view interference patterns (Lisle *et al.* 1991) (Figs. 3.4b - 3.6b) are rare in coevally shortened models, but common in sequentially shortened models (Figs. 2.7b & 2.8b, d). The presence of strain-incompatibility features such as fractures and curvature-accommodation folds suggest that isometric bending of a competent unit is more difficult to achieve by sequential than coeval shortening. Sequential shortening may resist isometric bending because it requires the refolding of F_1 limbs which have different attitudes and curvature (cf. Ramsay 1967 p. 546-547).

The prevalence of fractures in the superposed shortening models (Fig. 3.17) compared with the coevally shortened models (Fig. 3.18) is consistent with theory of lesser total strains during folding within the constriction strain field than within the flattening strain field (Treagus and Treagus 1981). Thus strain markers in regions that deformed during a single, constrictional event should record strains of a smaller magnitude than markers deformed during polydeformation.

Field Applications

Physical models predict that, on the regional scale, folds produced by coeval shortening plunge shallowly and vary in trend, but lack tightly refolded hingelines and axial traces (cf. Figs. 2.9 & 3.7). In the field, coeval shortening may be recognized by domains of nearly uniform fold orientation, domains where different fold trends abut one another, and domains where hingelines and axial traces are gently curved. Sequential shortening may be recognized by one set of

hingelines and axial traces that are folded, and an additional set of hingelines and axial traces that are highly oblique to the first set and parallel to their axial surfaces.

Implications for Restoration

Shortening in two directions associated with rigid, highly oblique boundaries may be uncommon geologically. Examples of analogous natural cases include the interfering strain fields of adjacent, coeval plutons, the shortening constrained by oblique basement uplifts or lateral ramps, or a curved fold belt that is concave towards its foreland. More generally, these models have implications for noncylindrical folds that develop in the absence of plane strain.

Cross section restoration commonly assumes that plane strain conditions are maintained in the direction of tectonic transport (e.g. Elliott 1983, Geiser 1988). Sections across noncylindrical structures and across oblique footwall ramps are thus typically avoided in cross section construction. Recent research, however, has focused on precisely such non-plane strain regions of fold belts (e.g. McDonough & Simony 1989, Wilkerson *et al.* 1991, 1992, Marshak *et al.* 1992, Apotria 1992, Braun 1993, Kveton 1994). New techniques are being developed to restore in three-dimensions deformed surfaces and volumes (e.g. Schultz-Ela 1988, McCoss 1988, Gratier *et al.* 1991, Rouby *et al.* 1993a, 1993b, VonWinterfeld & Oncken 1995). The present study suggests that the deformation history, i.e. whether the deformation is sequential or coeval, influences both the orientation and style of structures. I proprose that the restoration of deformed three-dimensional structures will likewise depend on whether structures in different orientations are restored sequentially or coevally. The deformation history will affect the geometry of the

restored structures and the inferred amount of shortening in each direction. As three-dimensional restoration techniques are refined, the sequence of restoration in different directions should be considered a significant variable.

SUMMARY

Bi-directional, coeval shortening of layering with significant competence-contrast has a fold interference style distinct from that formed by superposed shortening of the same material, with the same deformation and boundary conditions. Coeval shortening produced horizontal folds, with approximately linear hingelines and planar axial surfaces that have variable trend. The dominant style was plane, noncylindrical folds, as opposed to the non-plane, noncylindrical folds produced by sequential shortening of the same materials. Strain appeared to be more homogeneously accommodated on a regional scale in the coeval than the sequentially shortened model. Although structures produced by coeval and sequential shortening are similar to one another locally, the two shortening histories can be distinguished regionally. Coevally shortened folds are identified by the predominance of elongate domes and basins over Type 2 interference, the lack of tightly refolded hingelines and axial surfaces, the lack of regionally consistent fold orientation, and the lack of regionally consistent overprinting relationships.

Chapter 4: Comparison of Models and Field Examples

Fold interference occurs in a range of rock types and tectonic settings. It is most common in the metamorphic cores of orogenic belts. There, metamorphic layering typically has small to insignificant competence-contrast and deforms with a similar fold geometry (Ramsay 1962). Fold interference also occurs in the foreland regions of fold and thrust belts and in some accretionary prisms. There, lower grade metamorphic rocks and sedimentary rocks, which have a high competence-contrast between sedimentary layers or between a sedimentary package and a weak detachment, more commonly deform by buckling. Regional-scale buckle-fold interference is more complex than similar-fold interference.

Physical models of buckle-fold interference, described in Chapters 2 and 3, are dynamically scaled to represent structures affected by significant gravitational body forces. Thus, the models represent folds with wavelengths greater than about 200 m (Ramberg 1967 p. 75). The models were not designed to mimic a specific field area. Indeed, the simplified stratigraphy, boundary conditions, and deformation history of the models make a perfect natural analog elusive. Nonetheless, many of the features of different models are seen in a variety of natural examples, and they provide insight into fold interference processes.

The high competence-contrast, superposed shortening models that deformed in Type 2 interference, have the best natural analogs. In these models, the map-patterns of F_2 folds show fold styles that are consistent with a buckling

mechanism, including lobate-cuspate folds, kink-style folds, and detachment-style folds. Thus buckling is inferred as an important mechanism for natural structures with comparable structural styles. In the models with high competence-contrast, dome-and-basin style (Type 1) interference is rare. Where present, domes and basins typically include curvature accommodation folds (cf. Lisle *et al.* 1990), which could be used to diagnose a buckling mechanism in nature. In both the models and natural examples, dome-and-basin interference may be caused by either coeval or sequential shortening, but tends to occur where two differently oriented fold sets abut one another and where the fold style is open. Below are comparisons between model and field examples of regional-scale fold interference and implications for the natural features given the model interpretations discussed in Chapters 2 and 3. Because Type 2 interference is better documented, it is discussed first.

TYPE 2 INTERFERENCE

Superposed shortening of high competence-contrast models preferentially produced Type 2 interference, with lobate-cuspate, kink-style and detachment-style F2 folds. These styles are used to infer a buckling mechanism in the following natural examples.

Buckle-style F_2 Folds

In the high competence-contrast, superposed shortening models, steeply plunging F_2 folds show fold styles in map view that are analogous to profiles of competent layers buckled during a single deformation. Characteristic structures include lobate-cuspate style F_2 folds, fanning of minor hingelines and strain

markers, and increasing complexity of interference style from the outer- to the inner-arc of F_2 folds (Fig. 2.8 & 2.9). The Asturian arc, northern Spain, beautifully illustrates many of the features seen in the models (Fig. 4.1).

The Asturian arc is a Hercynian fold and thrust belt that is concave towards its foreland (de Sitter 1960). In the hinterland, the fold hingelines and thrust traces are gently curved. In the foreland, the Cantabrian Zone, two fold sets form complex interference patterns, and no metamorphic foliation is developed. One fold set has curved hingelines that are parallel to curved thrust traces. The other set, termed the "radial set", trends highly oblique to the first set (Fig 4.1) (Julivert & Marcos 1973). The extent to which the interference formed from sequential or coeval shortening in different directions is controversial.

Many studies interpret the Asturian arc as an orocline where E-W shortening produced gently curved thrust traces and fold hingelines (Pares *et al.* 1994, and references therein). During subsequent N-S shortening, the folds and thrusts became tightly curved in map view, and the radial fold set formed subparallel to the axial trace of the arc (Julivert & Marcos 1973). The orocline interpretation is supported by the superposed shortening models (compare Figs. 2.8, 2.9, & 4.1). Like the models, the Austurian arc is characterized by tightly curved F_1 hingelines and nearly linear F_2 hingelines, both Type 1 and Type 2 interference, F_2 domes parasitic upon and elongate parallel to the axial traces of broad F_2 crescents, fanning of F_2 axial traces, and complex interference patterns in the inner-arc of F_2 folds.

Alternatively, the radial fold set may have formed coevally with the thrusts, due to thrust motion over oblique and lateral ramps (Alvarez-Marron &

Figure 4.1. Interference in the Cantabrian Zone, Asturian Arc, northern Spain (simplified after Julivert & Marcos 1973 Fig.1). The "arched" fold set (gray lines) is associated with curved thrusts. The "radial" fold set (black lines) may have initiated due to oblique thrusting, or may have been superposed on the arched set as the Asturian Arc tightened during N-S shortening. Note that the hingelines of the radial set fan about an average E-W trend. See Fig. 4.12 for more detailed view of the interference patterns.

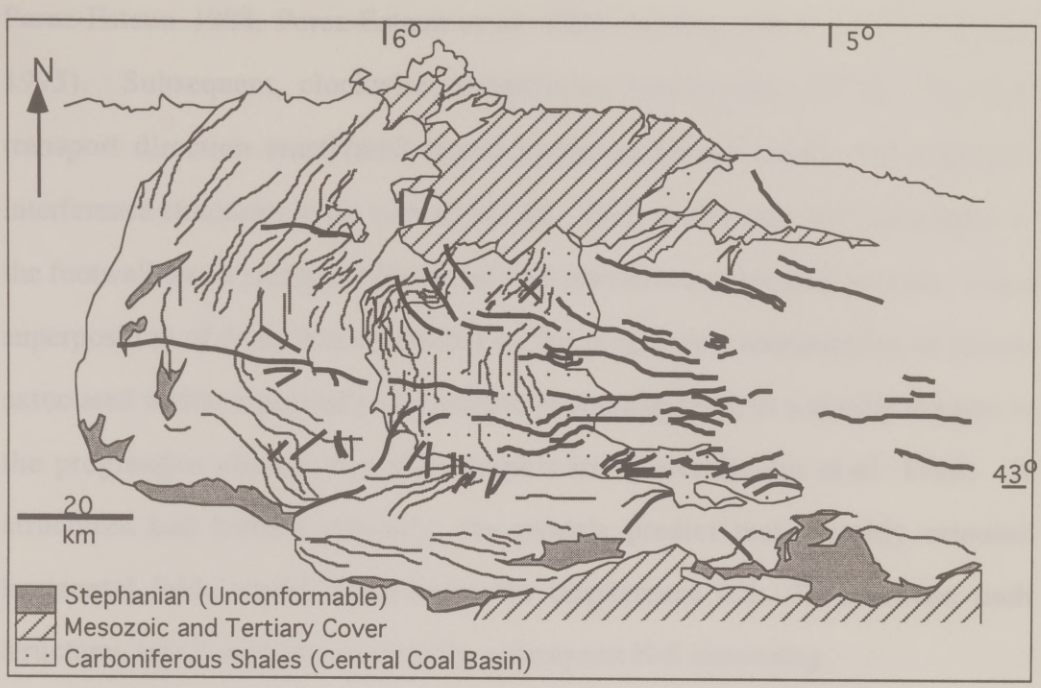
N
6°
5°
43°
20
km
Stephanian (Unconformable)
Mesozoic and Tertiary Cover
Carboniferous Shales (Central Coal Basin)

Perez-Estaun 1988, Perez-Estaun *et al.* 1988, Stewart 1993, Alvarez-Marron 1995). Subsequent, clockwise, progressive reorientation of the dominant transport direction reactivated lateral ramps as frontal ramps and amplified interference structures in the core of the arc. Thus, in this case, the topography of the footwall was a primary influence of fold interference style and location. Local superposition of folds was controlled by the progressive reorientation of thrusts associated within a generally constrictive shortening field, in a similar manner to the progressive closure of a photographic iris (Perez-Estaun *et al.* 1988). If structures had formed coevally, the models predict that variably oriented horizontal folds would characterize the interference (Ch. 3); however, such structures may have been obscured by subsequent N-S shortening.

Because both interpretations require a degree of N-S shortening superposed on E-W shortening, the principal difference between the two models is the role of thrust geometry. In this modeling study, thrusting was not an important deformation mechanism (Ch. 2 and 3). Future mechanical analysis of thrusting over oblique ramps would prove useful, not only where multiple generations and orientations of thrust movements are suspected, but also where noncylindrical folds are associated with a single thrust sheet (e.g. Apotria *et al.* 1992, de Lamotte *et al.* 1995).

Megakinks

In the models, kink-style interference is prominent where the stratigraphy has a high competence-contrast, the deformation is polyphase, and a structural anisotropy is developed during the first shortening event (Ch. 2, Fig. 2.8a, b). In

the field, km-scale kink-style interference is evidence of an early-formed structural anisotropy. This style of interference is well illustrated by megakinks of the Lachlan Fold Belt, New South Wales, and of the Shimanto belt, southwestern Japan.

In Ordovician turbidites of the Lachlan fold belt, S_1 foliation is broadly kinked (Powell 1984, Powell *et al.* 1985)(Figs. 4.2-4.4). Upright F_1 folds have subhorizontal hingelines. Axial planar S_1 cleavage is vertical and is differentiated into quartz- and mica-rich bands. The F_1 hingelines generally trend NNE and are consistently oriented within domains as wide as 10 km. The F_1 hingelines change orientation abruptly, by 20-30°, across zones 10-100 m wide. Like the F_1 hingelines in the models, F_1 axes are refolded within a predominantly horizontal plane, about steeply plunging axes (compare Figs. 2.12c, d and Fig. 4.4). Locally, the megakink bands crosscut one another (Fig. 4.3). In the models, conjugate high strain zones nucleated and intersected at F_1 periclinal depressions (Ch. 2). Similarly, in the field the location of the megakink zones is governed by pre-existing structures. In the Lachlan fold belt, megakinks coincide with and possibly nucleated on the Lachlan River lineament and the Murray River lineament (Powell 1984)(Fig. 4.2). No kinking is present west of the Tantawangalo fault, where the lithology changes to a more massive, less foliated facies (Fig. 4.3). Contemporaneous E-W trending thrusts in cratonic Australia and strike-slip faults that are subparallel to the kink zones in domains with a slaty cleavage are further evidence that the kinks accommodate horizontal, N-S shortening and that the structural style depends on the stratigraphy deformed (Powell 1984).

Figure 4.2 Megakinks in southeast Australia and their relationship to thrusts in the craton (simplified after Powell 1984 Fig. 3). Boxed regions shown in detail in Figs. 4.3 and 4.11.

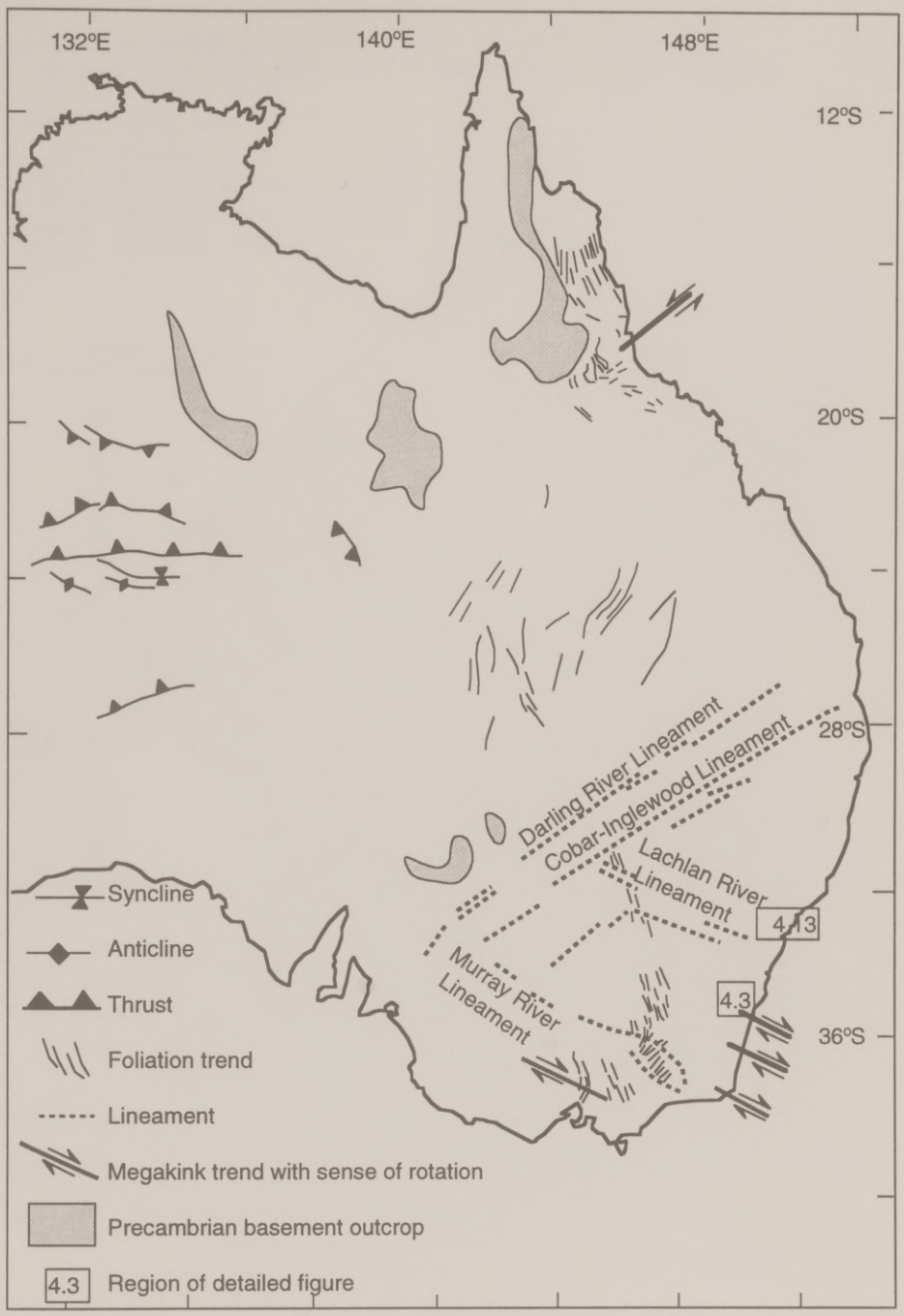
132°E
140°E
148°E
12°S
20°S
28°S
36°S
Darling River Lineament
Cobar-Inglewood Lineament
Lachlan River Lineament
Murray River Lineament
4.3
4.3
Syncline
Anticline
Thrust
Foliation trend
Lineament
Megakink trend with sense of rotation
Precambrian basement outcrop
4.3 Region of detailed figure

Fig. 4.3. Megakinks (dashed lines) of nearly vertical S_1 foliation (solid lines) in the Lachlan fold belt, New South Wales (simplified after Powell *et al.* 1985 Fig. 4).

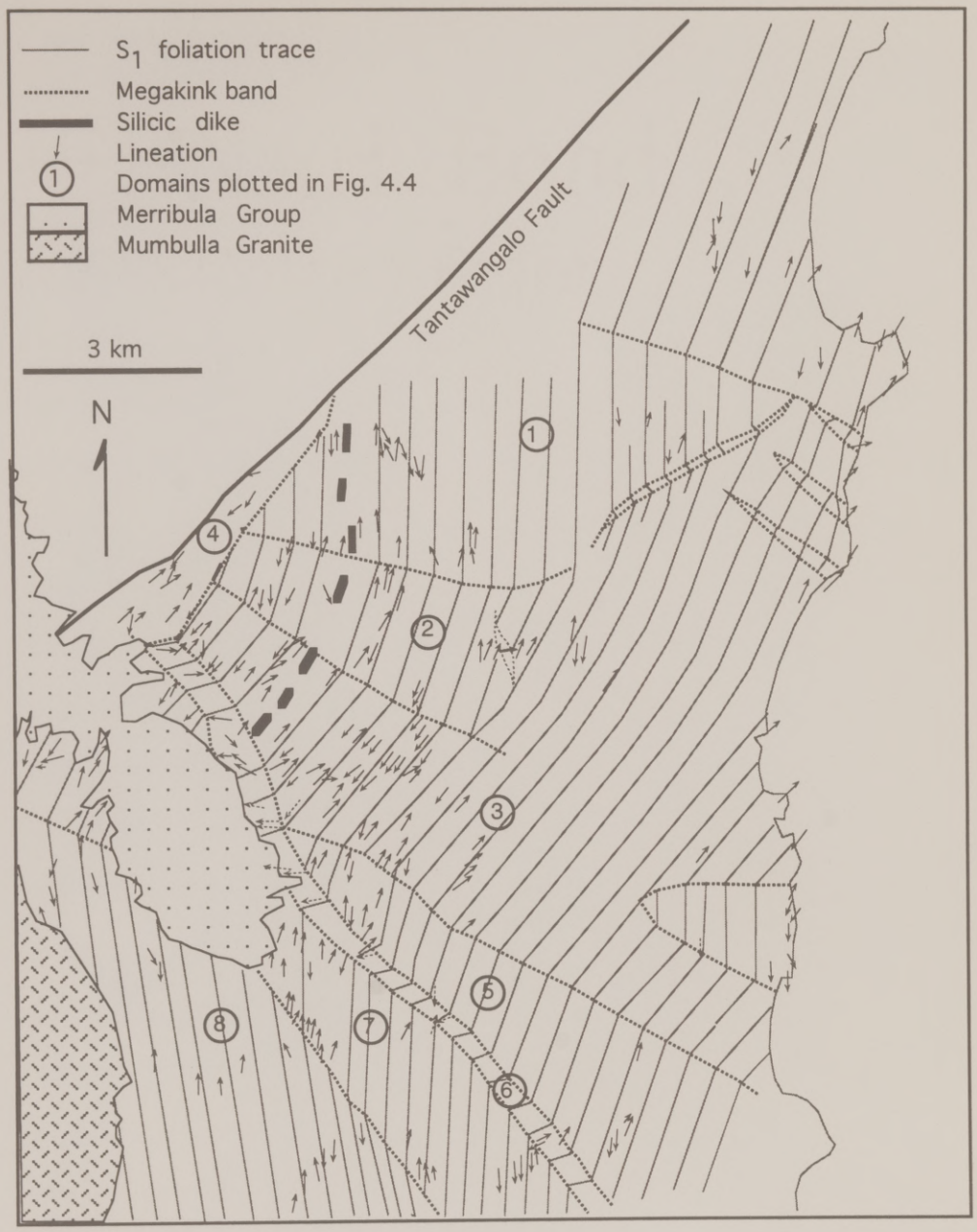
S_1 foliation trace
Megakink band
Silicic dike
Lineation
1
Domains plotted in Fig. 4.4
Merribula Group
Mumbulla Granite
3 km
N
Tantawangalo Fault
1
2
3
4
5
6
7
8

Figure 4.4 Equal area distributions of poles to S_1 foliation (dots) and lineations (x's and open circles) in different domains plotted in Fig. 4.3 (Powell *et al.* 1985 Fig. 4).

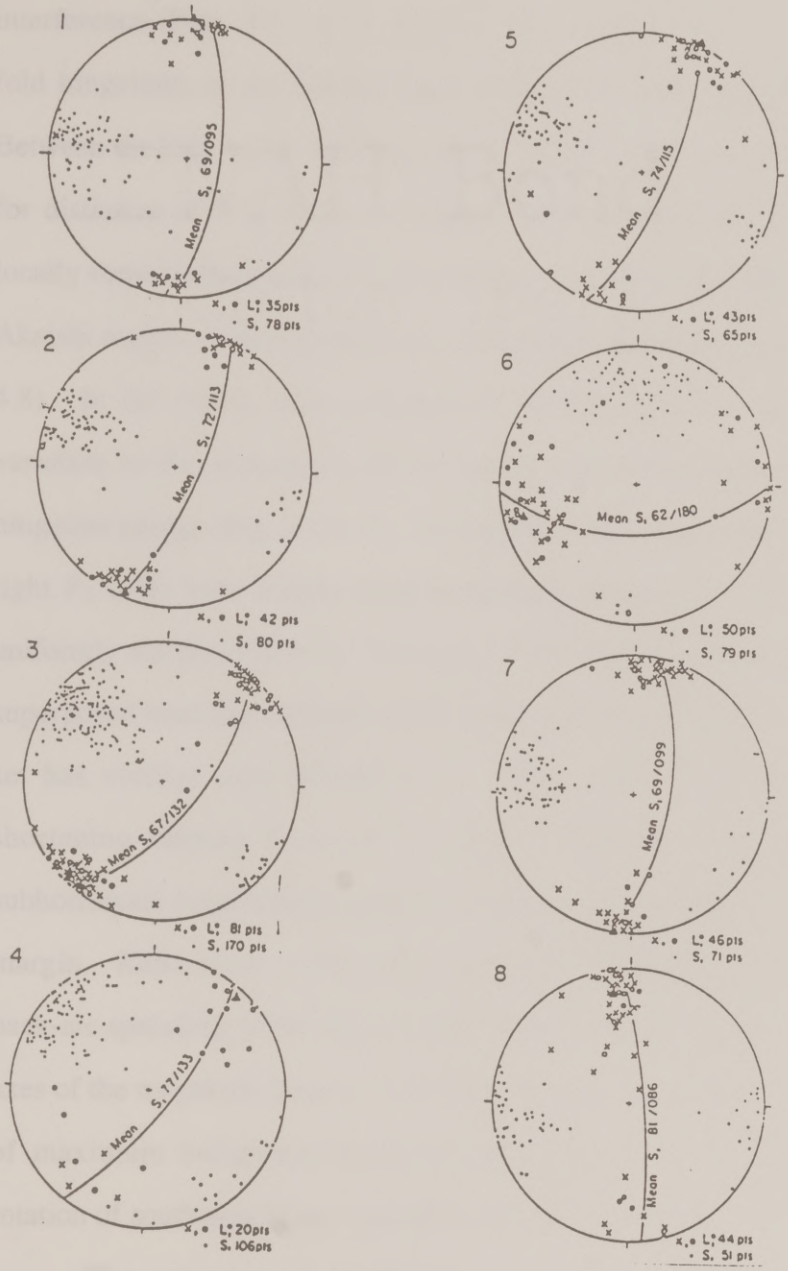
1
Mean S, 69/095
L: 35pts
S, 78 pts
2
Mean S, 72/113
L: 42 pts
S, 80 pts
3
Mean S, 67/132
L: 81 pts
S, 170 pts
4
Mean S, 77/133
L: 20pts
S, 106pts
5
Mean S, 74/115
L: 43pts
S, 65pts
6
Mean S, 62/180
L: 50pts
S, 79 pts
7
Mean S, 69/099
L: 46pts
S, 71 pts
8
Mean S, 81/086
L: 44 pts
S, 51 pts

In the Shimanto fold and thrust belt, southwestern Japan, weakly metamorphosed sandstone and mudstone units also show kink-style fold interference (Figs. 4.5 - 4.7). Nearly vertical bedding traces and subhorizontal fold hingelines of are kinked about steeply plunging axes (Kano *et al.* 1990). Between the kink zones, bedding traces and fold hinges are uniform in orientation for distances of 5 to 30 km. Similar to the models (Fig. 2.8), the kink zones locally form conjugate pairs or fan around a common axis (Figs. 4.6, 4.7). In the Akaishi region, strike-slip faults are subparallel to the kink zone boundaries (Fig. 4.8). In the model with moderate D_1 shortening (c217, D_1=44%, D_2=33%), variation in the inclination and curvature of layering caused a variation in F_2 hingeline plunge (Fig. 2.12e, f). In southwest Japan, as in the Lachlan Fold Belt, tight F_1 folds have steeply dipping bedding surfaces, so the kink axes plunge uniformly steeply (Fig. 4.7). This style of refolding closely approximates Mode 5 superposed buckling, defined where the first fold set is isoclinal and the second set has vertical axes (Ghosh *et al.* 1993). The kink zones accommodated shortening ranging from 2% to 20% in different parts of the belt. The subhorizontal folds formed during subduction along Japan's eastern accretionary margin. Kano *et al.* (1990) interpreted the megakink bands as formed during back-arc spreading of the Sea of Japan. They proposed that the change in rotation axes of the megakink bands in different domains reflects the change in orientation of maximum horizontal stress that accompanied the progressive clockwise rotation of southwest Japan, caused by differential opening of the Sea of Japan.

The presence of kink-style interference in the field signifies low temperature, semi-brittle deformation of a rock with a strong structural anisotropy.

Figure 4.5. The Shimanto belt, southwestern Japan, is bounded to the north by the Butsuzo Tectonic line. Insets show locations of more detailed figures.

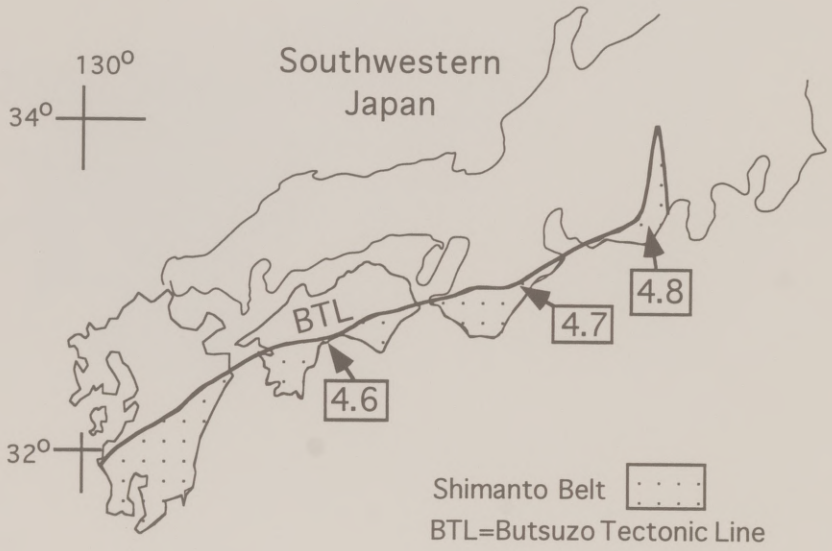
130°
34°
32°
Southwestern
Japan
BTL
4.6
4.7
4.8
Shimanto Belt
BTL=Butsuzo Tectonic Line

Figure 4.6. Megakinks of bedding traces in the Shikoku region, Shimanto fold and thrust belt, southwest Japan (Fig. 6 Kano *et al.* 1990). Note that kink bands form conjugate sets.

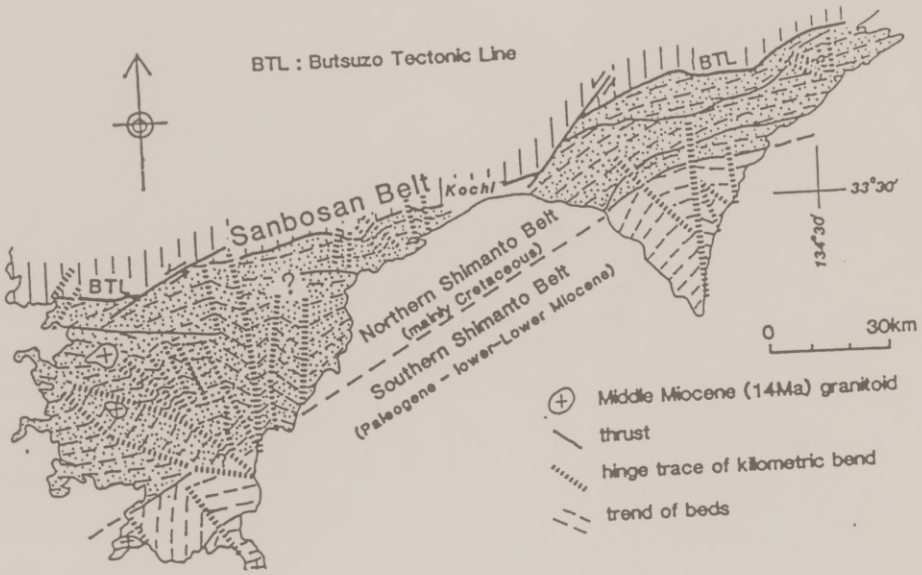
BTL : Butsuzo Tectonic Line
BTL
Sanbosan Belt
Kochi
BTL
?
Northern Shimanto Belt
(mainly Cretaceous)
Southern Shimanto Belt
(Paleogene - lower-Lower Miocene)
33°30'
134°30'
0
30km
Middle Miocene (14Ma) granitoid
thrust
hinge trace of kilometric bend
trend of beds

Figure 4.7. Megakinks of bedding traces and projections of poles to bedding in the Ryujin region, Shimanto fold and thrust belt, southwest Japan (Fig. 4 Kano *et al.* 1990).

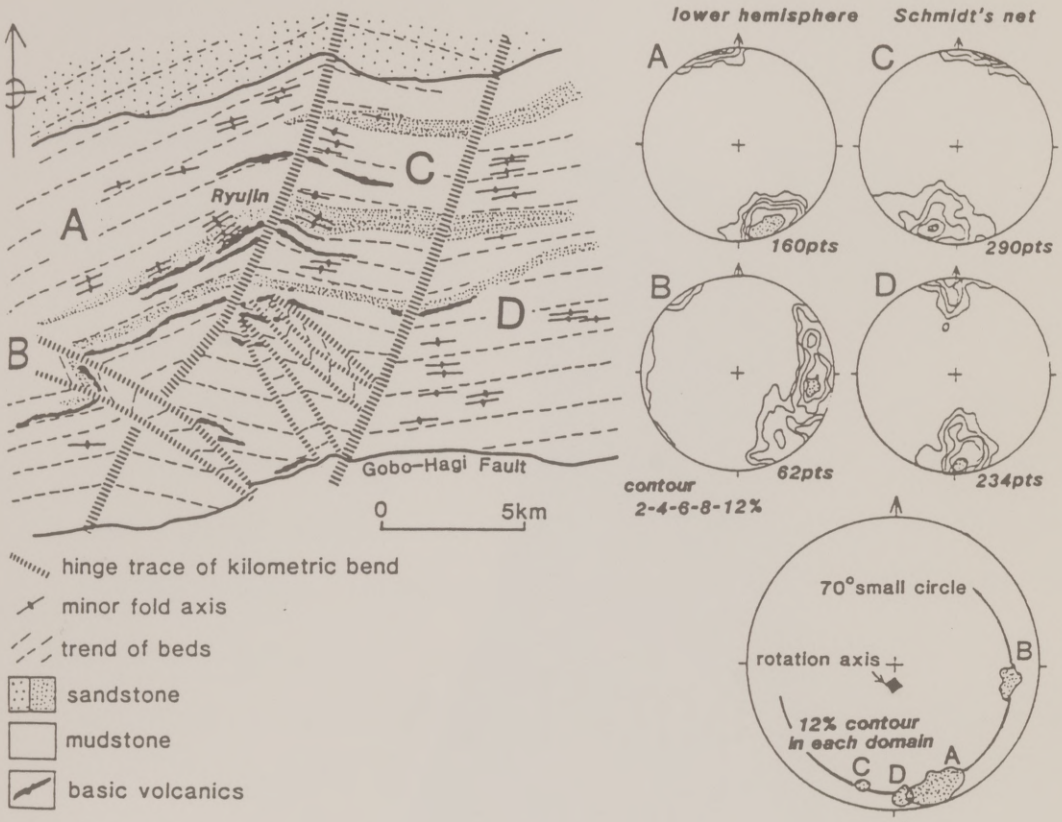
lower hemisphere
Schmidt's net
A
C
B
D
160pts
290pts
62pts
234pts
contour
2-4-6-8-12%
Ryujin
Gobo-Hagi Fault
0
5km
hinge trace of kilometric bend
minor fold axis
trend of beds
sandstone
mudstone
basic volcanics
70°small circle
rotation axis
12% contour
in each domain

Figure 4.8 Megakinks of bedding traces in the Akaishi region, Shimanto Fold and Thrust Belt, Japan (Fig. 5 Kano *et al.* 1990). Megakink bands (dashed lines) are parallel to strike-slip faults.

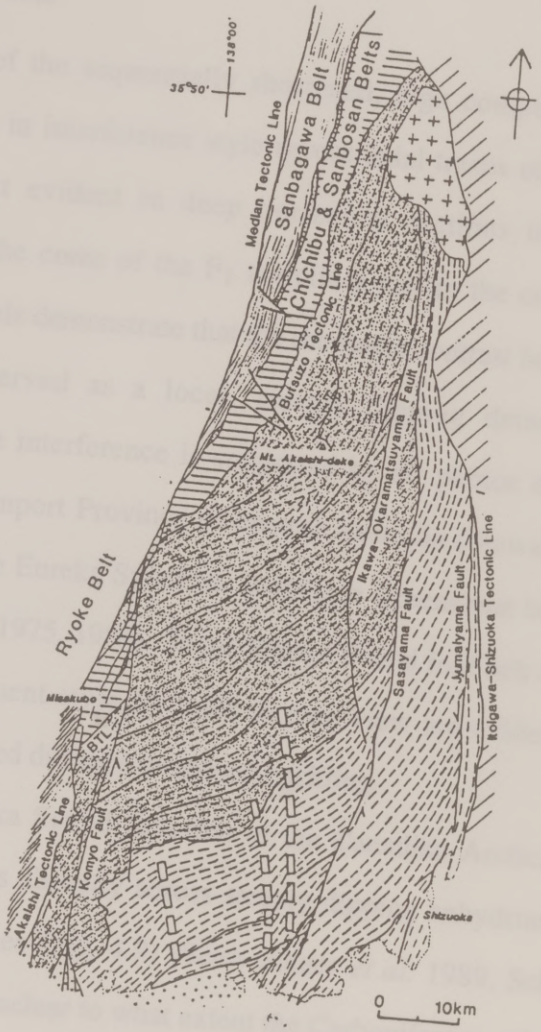
35°50'
138°00'
Median Tectonic Line
Sanbagawa Belt
Chichibu & Sanbosan Belts
Butsuzo Tectonic Line
Mt. Akaishi-dake
Ryoke Belt
Kawa-Okaramatsuyama Fault
Sasayama Fault
Yumiyama Fault
Itoigawa-Shizuoka Tectonic Line
Misaktubo
Akaiwa Tectonic Line
Komyo Fault
Shizuoka
0
10km

In both southwest Japan and southeast Australia, strike-slip faults are associated with the kink bands. Because the kinks reoriented the foliation within discrete zones, the percent shortening and rotation axes could be calculated (Powell 1984, Kano *et al.* 1990).

Detachment Folds

Many of the sequentially shortened, high competence-contrast models show a change in interference style across axial traces of major F_1 folds. This change is most evident in deep horizontal sections that expose the basal detachment in the cores of the F_1 anticlines and in the cusps of F_2 folds (Fig. 2.8d). The models demonstrate that the rheologic contrast between the basal layer and laminate served as a local, steeply dipping detachment during D_2. Detachment-style interference is suggested by air photos of folds in the Early Proterozoic Davenport Province of central Australia (Stewart 1987) and by the map pattern of the Eureka Syncline, Barberton Greenstone belt, Africa (Ramsay 1965, Anhaeusser 1975, 1984). In the Eureka Sound fold belt and in the Grenville Province, detachment-style F_2 folds in map view are evidence of a structural anisotropy developed during superposed buckling.

In the Eureka Sound fold belt of the Canadian Arctic, the style of fold interference changes abruptly across steeply dipping anhydrite beds exposed in the cores of anticlines (Fig. 4.9) (Schwerdtner *et al.* 1989, Schwerdtner & van Berkel 1991). It is unclear to what extent the Carboniferous anhydrite strata were initially deformed by diapirism or by flow during the late Cretaceous Eurekan orogeny (van Berkel *et al.* 1984, Schwerdtner *et al.* 1989, Okulitch & Trettin

Figure 4.9. Interference folds associated with anhydrite (shaded) detachments, Axel Heiberg Island, Canadian Arctic (simplified after Fig. 2, van Berkel *et al.* 1984). Note that anhydrite is exposed along anticlinal traces. The Southern Muskox Ridge Diapir and the Junction Diapir occur in the inner-arcs of map-view detachment folds.

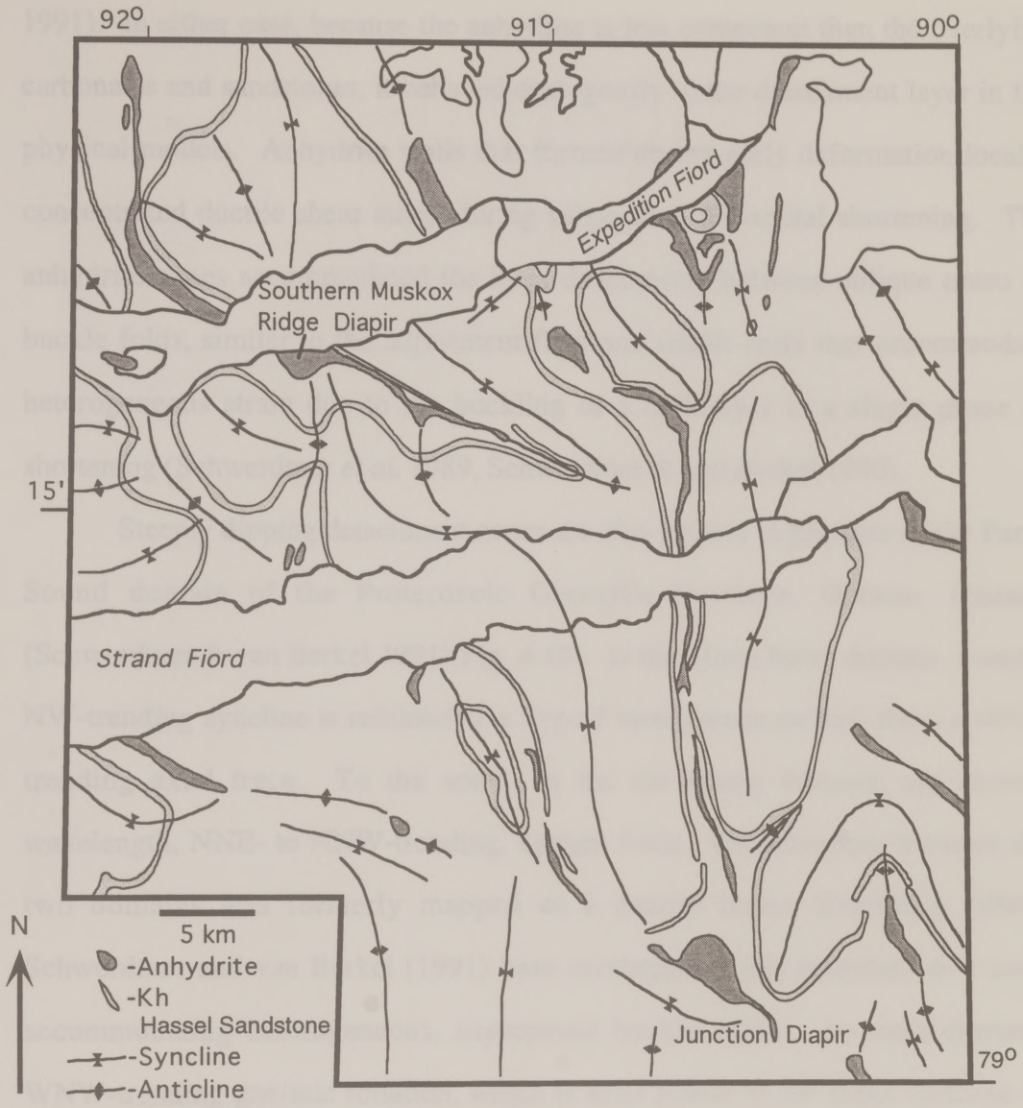
92°
91°
90°
Expedition Fiord
Southern Muskox
Ridge Diapir
15'
Strand Fiord
N
5 km
-Anhydrite
-Kh
Hassel Sandstone
-Syncline
-Anticline
Junction Diapir
79°

1991). In either case, because the anhydrite is less competent than the overlying carbonates and sandstones, it behaved analogously to the detachment layer in the physical models. Anhydrite walls that formed during early deformation locally concentrated ductile shear strain during subsequent horizontal shortening. The anhydrite zones accommodated the local disharmony between oblique trains of buckle folds, similar to the adjustment flow and saddle reefs that accommodate heterogeneous strain due to the buckling of a multilayer in a single phase of shortening (Schwerdtner *et al.* 1989, Schwerdtner & van Berkel 1990).

Steeply dipping detachment zones are also present in gneisses of the Parry Sound domain of the Proterozoic Grenville Province, Ontario, Canada (Schwerdtner & van Berkel 1991)(Fig. 4.10). In the Moon River domain, a major NW-trending syncline is refolded in a Type 2 interference pattern about a NNE-trending axial trace. To the south, in the Go Home domain, are shorter wavelength, NNE- to NNW-trending, upright folds. The boundary between the two domains was formerly mapped as a ductile thrust (Davidson 1984). Schwerdtner and van Berkel (1991) have reinterpreted this boundary as a zone accommodating heterogeneous, superposed buckle strain. An early-formed, WNW-trending gneissic foliation, which is axial planar to the major syncline of the Moon River domain, provided a structural anisotropy that allowed buckling during subsequent shortening and locally served as a detachment surface.

The field examples demonstrate that structural anisotropies developed during an early phase of deformation may be reactivated during subsequent deformation as local detachments.

Figure 4.10. Detachment-style interference in the Grenville Province, Ontario, Canada (after Fig. 8, Schwerdtner & van Berkel 1991). The boundary between the Moon River and Go Home structural domains (heavy dashed line) may represent a detachment that accommodates superposed buckling.

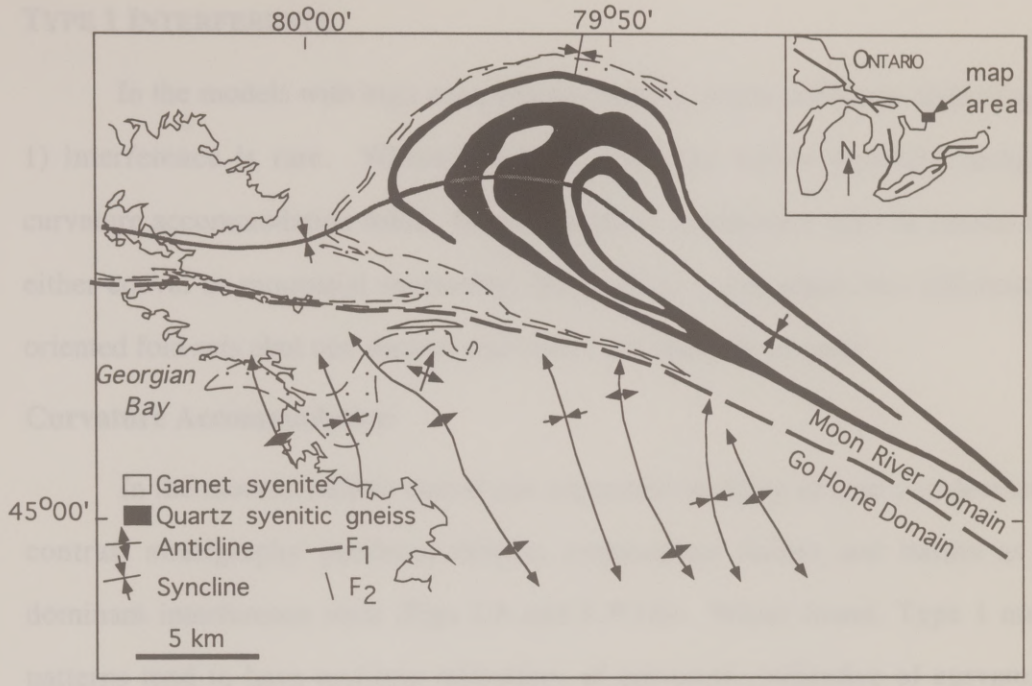
80°00'
79°50'
45°00'
ONTARIO
map area
N
Georgian Bay
Moon River Domain
Go Home Domain
Garnet syenite
Quartz syenitic gneiss
Anticline
Syncline
F1
F2
5 km

TYPE 1 INTERFERENCE

In the models with high competence-contrast, dome-and-basin style (Type 1) interference is rare. Where present, domes and basins typically include curvature accommodation folds. Dome-and-basin interference may be caused by either coeval or sequential shortening, but tends to occur where two differently oriented fold sets abut one another and where the fold style is open.

Curvature Accommodation

In the models, neither coeval nor sequential buckling of high competence-contrast stratigraphy produces simple, symmetrical domes and basins as a dominant interference style (Figs 2.8 and 3.3-3.6). Where found, Type 1 map patterns tend to have multiple inflections of curvature, indicative of curvature accommodation folds (Lisle *et al.* 1990). This type of fold has also been described in the Missi Group metaclastics in the Flin Flon Basin, Churchill Province, Manitoba. There, the greenschist-grade basal metaconglomerate is complexly refolded. F_1 axial traces intersect F_2 axial traces at nearly right angles, yet the map interference pattern has multiple lobes (Stauffer & Mukherjee 1971)(Fig. 4.11). Within some domains, fold axes defined by poles to bedding are oblique to both the F_1 and F_2 fold trends. The lobes that are oblique to the F_1 and F_2 trends are curvature accommodation folds, which allow the relatively competent metaconglomerate unit to fold in two directions without changing thickness (Stauffer 1988, Lisle *et. al.* 1990).

In the models, fractures and faults also accommodate bidirectional curvature (Fig. 3.17). In the Cantabrian fold and thrust belt, Spain, a basin-

Figure 4.11. Bedding trace map of curvature accommodation folds (marked CAF) near Flin Flon, Manitoba. CAF's trend oblique to F_1 axial traces (dashed) and F_2 axial traces (solid) (after Stauffer & Mukherjee 1971 Fig. 8).

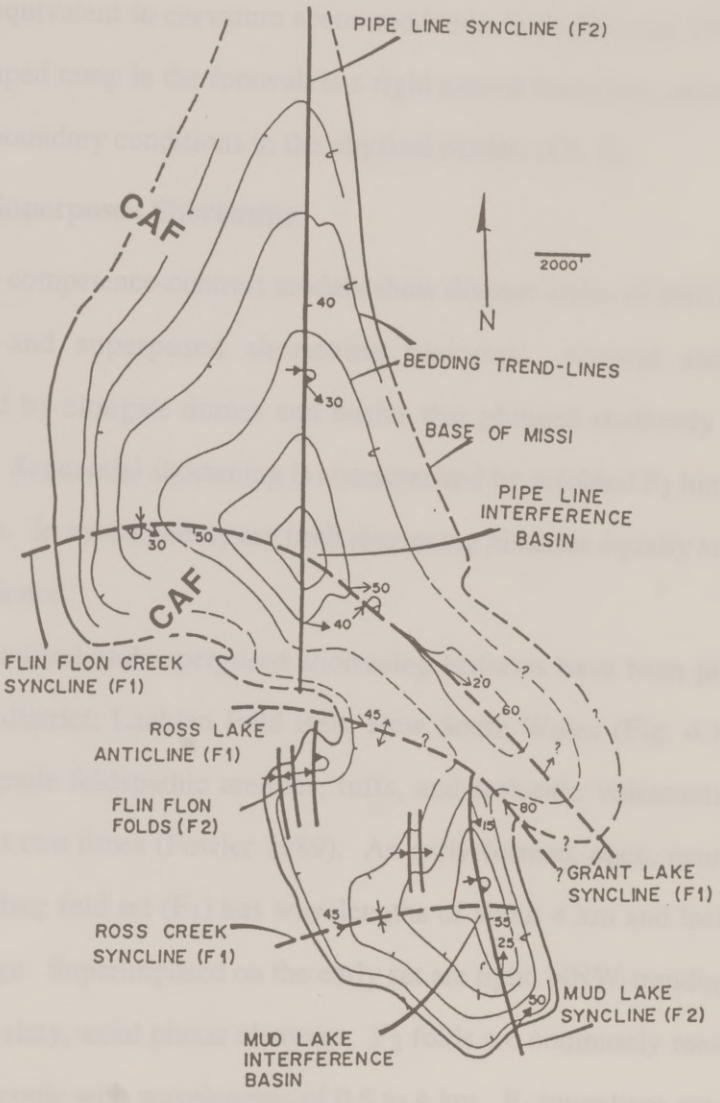
PIPE LINE SYNCLINE (F2)
CAF
2000'
N
40
BEDDING TREND-LINES
30
BASE OF MISSI
PIPE LINE
INTERFERENCE
BASIN
30
50
CAF
50
40
FLIN FLON CREEK
SYNCLINE (F1)
20
60
ROSS LAKE
ANTICLINE (F1)
45
FLIN FLON
FOLDS (F2)
80
15
GRANT LAKE
SYNCLINE (F1)
45
ROSS CREEK
SYNCLINE (F1)
55
25
MUD LAKE
SYNCLINE (F2)
50
MUD LAKE
INTERFERENCE
BASIN

shaped, fault-bend fold occurs where the competent Ponga Unit was thrust over oblique footwall and lateral ramps (Stewart 1993, Alvarez-Marron 1995)(Fig. 4.12). This massive, predominantly quartzite unit shows no evidence of thickening in the structural culmination. Instead, a minor strike-slip fault serves as a brittle equivalent to curvature accommodation folds (Stewart 1993). Such a "corner"-shaped ramp in the footwall is a rigid natural boundary, analogous to the orthogonal boundary conditions in the physical models (Ch. 3).

Coeval vs. Superposed Shortening

High competence-contrast models show distinct styles of fold interference for coeval and superposed shortening histories. Coeval shortening is characterized by elongate domes and basins that plunged shallowly in variable orientations. Sequential shortening is characterized by refolded F_1 hingelines and axial surfaces. In nature, rarely are both shortening histories equally supported by geologic evidence.

Both coeval and superposed shortening histories have been proposed for the Rockley district, Lachlan Fold Belt, New South Wales (Fig. 4.13). There greenschist-grade feldspathic arenites, tuffs, and andesitic volcaniclastics were folded at least two times (Fowler 1989). An early-formed, open, nearly upright, variably-trending fold set (F_1) has wavelengths of about 4 km and lacks an axial planar cleavage. Superimposed on the early set are tight, NNW-trending F_2 folds, which have a slaty, axial planar cleavage. F_2 folds are commonly mesoscopic or rarely macroscopic with wavelengths of 0.8 to 4 km. F_1 hingelines range in trend from NNW to ENE, but generally are not tightly folded in a Type 2 interference

Figure 4.12. (a) Curved thrusts of the Cantabrian Zone, Asturian Arc, northern Spain. Large arrow is trend of major D2 fold. Small arrows show orientation of fold hingelines that are associated with a "corner" in the footwall ramp (after Stewart 1993 Fig.2). (b) Schematic representation of basin-shaped interference formed by thrusting in two directions over an oblique ramp. Area is hatched zone in (a). Note that a strike slip duplex (SSD) accommodates the bending of the competent thrust sheet (after Fig. 6, Stewart 1993).

a)

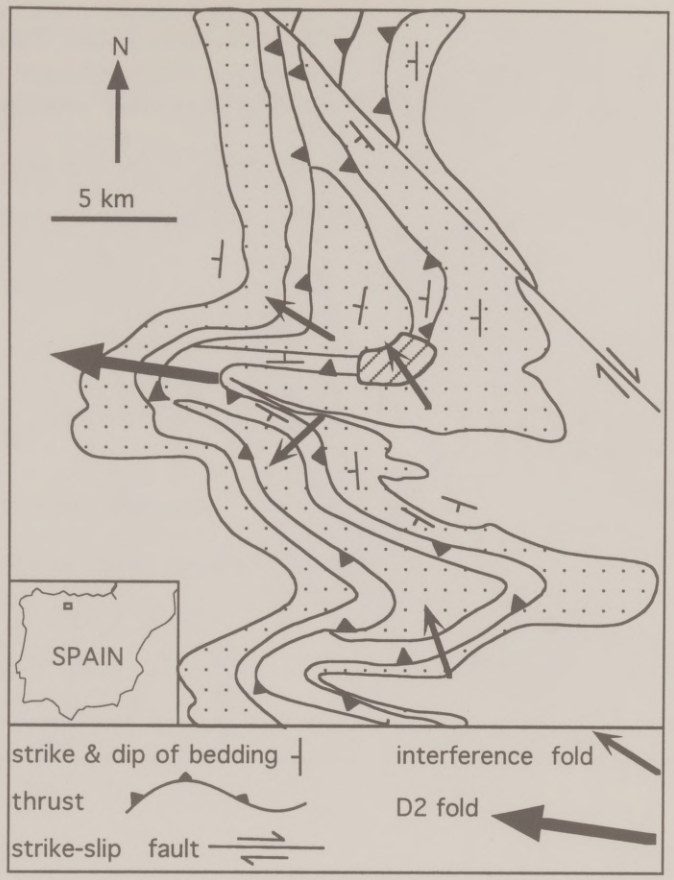
N
5 km
SPAIN
strike & dip of bedding
thrust
strike-slip fault
interference fold
D2 fold

b)

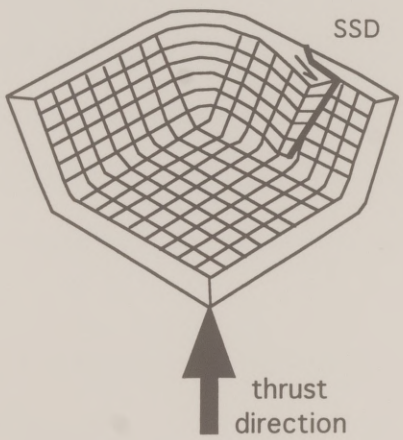
SSD
thrust
direction

Figure 4.13. Fold interference in the Rockley district, New South Wales (simplified after Fowler 1989 Fig. 2). F_1 folds trend parallel to oblique to typically mesoscopic F_2 folds, which have an axial-planar slaty cleavage (dashed lines).

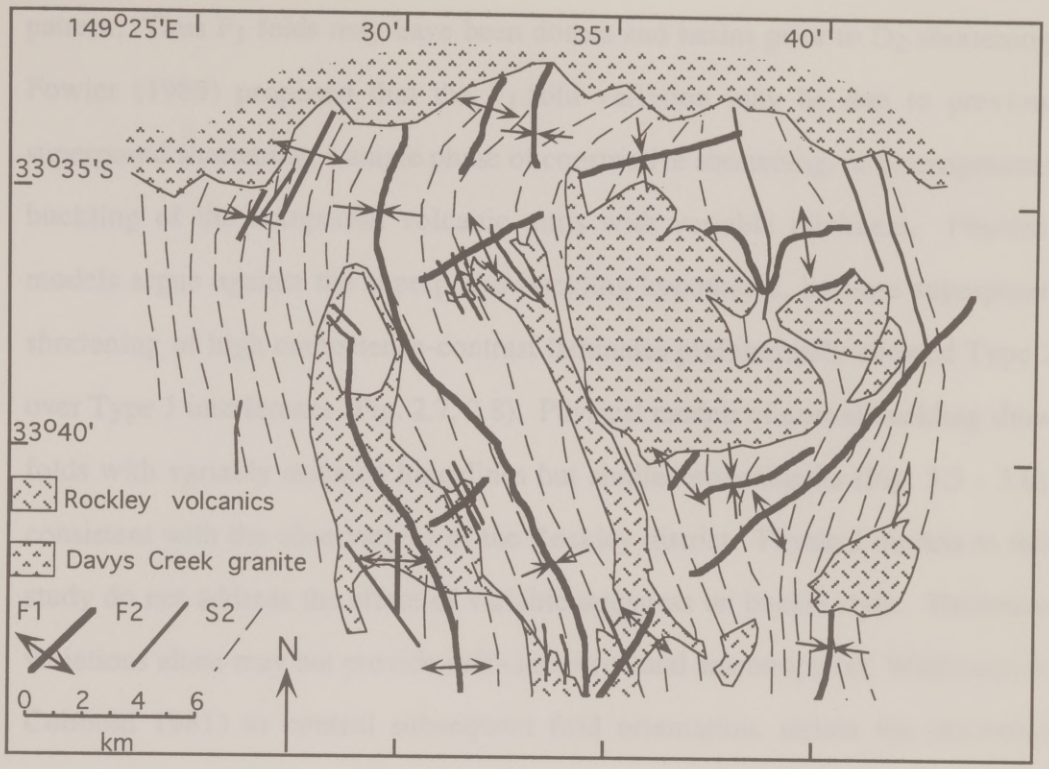
149°25'E
30'
35'
40'
33°35'S
33°40'
Rockley volcanics
Davys Creek granite
F1
F2
S2
N
0 2 4 6
km

pattern. Thus F_1 folds may have been domes and basins prior to D_2 shortening. Fowler (1989) proposed that the F_1 fold variation may be due to previous superposed shortening, a single phase of constrictive shortening, or heterogeneous buckling of the competent volcanic units with variable thickness. Physical models argue against the superposed buckling hypotheses, because superposed shortening of high competence-contrast laminates preferentially showed Type 2 over Type 1 interference (Fig. 2.7, 2.8). Physical models of coeval buckling show folds with variably oriented hingelines but similar wavelengths (Fig. 3.3 - 3.6), consistent with the observations of the Rockley district. Physical models in this study do not address the effect of variable thickness on buckle style. Thickness variations alone may not provide sufficient structural anisotropy (cf. Watkinson & Cobbold 1981) to control subsequent fold orientation, unless the thickness variation had a strong directional control.

Fold Abutment

In high competence-contrast models, dome-and-basin style interference is associated with the abutment of one fold trend against another. This style occurred in the superposed shortening model with low D_1 strain (Fig. 2.7), and in coevally shortened models (Figs. 3.3 - 3.6). In nature, dome-and-basin style interference is found at the intersection of two structural trends of known and distinct ages.

Dome-and-basin interference occurs at the intersection of the east-trending Parry Islands fold belt and the north-trending Cornwallis fold belt, Canadian Arctic (Fig. 4.14) (Kerr 1977, Okulitch et al. 1986, Okulitch *et al.* 1991). The

Figure 4.14 (a) Interference at the intersection of the N-S trending Cornwallis fold belt and E-W trending Parry Islands fold Belt, Canadian Arctic (data compiled from Kerr 1977 Fig. 2, Okulitch *et al.* 1986 Fig. 3, and Okulitch *et al.* 1991 Fig. 2). (b) Schematic cross section through the southern Corwallis fold belt, illustrating the thick-skinned style of deformation (modified after Okulitch *et al.* 1986 Fig. 5).

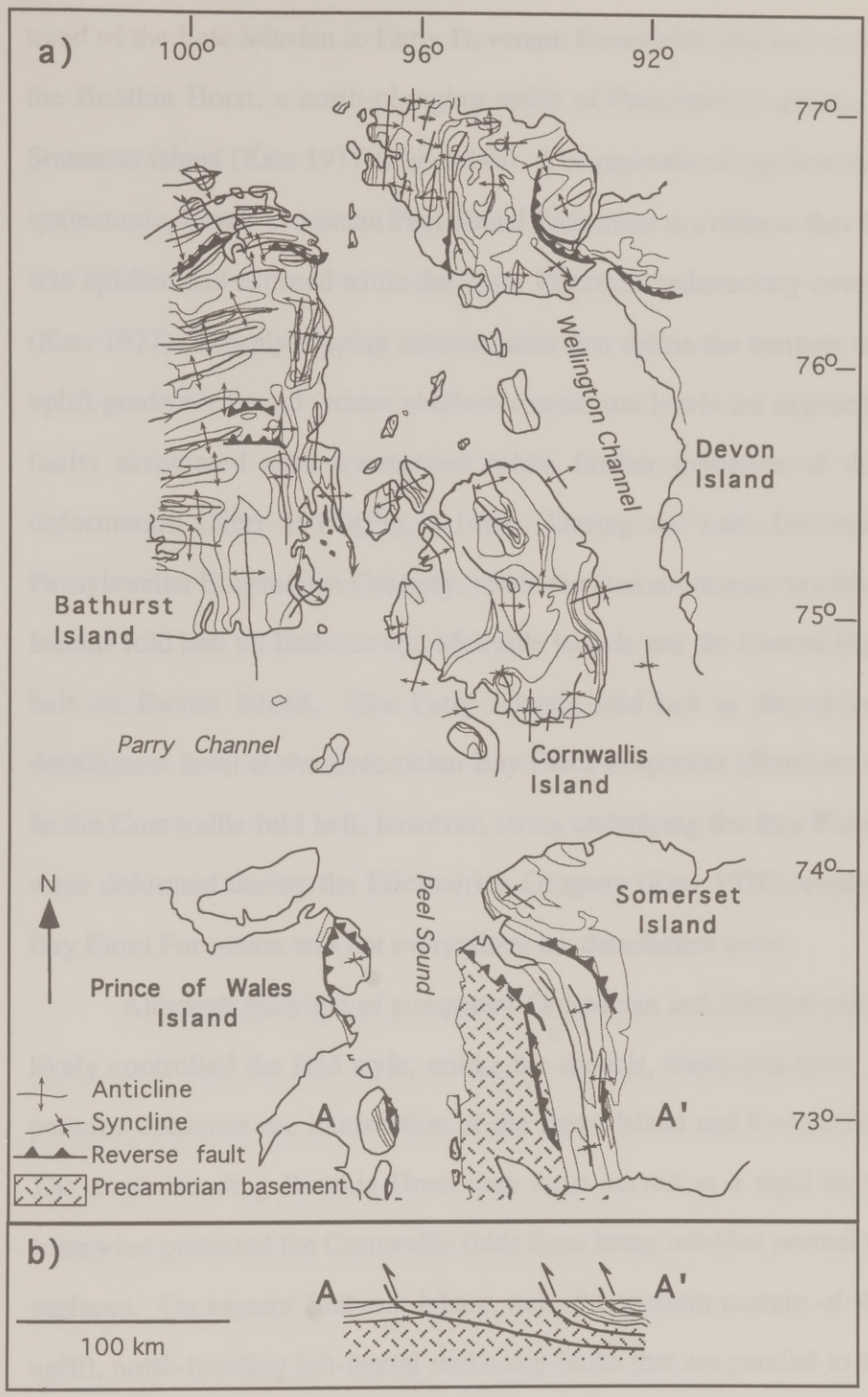
a)
100°
96°
92°
77°
76°
75°
74°
73°
Wellington Channel
Devon Island
Bathurst Island
Parry Channel
Cornwallis Island
Somerset Island
Peel Sound
Prince of Wales Island
N
A
A'
Anticline
Syncline
Reverse fault
Precambrian basement
b)
A
A'
100 km

trend of the Late Silurian to Early Devonian Cornwallis fold belt is controlled by the Boothia Horst, a north-plunging uplift of Precambrian gneiss, exposed on Somerset Island (Kerr 1977)(Fig. 4.14a). The presence of gneissic cobbles in the syntectonic, Lower Devonian Peel Sound Formation is evidence that the basement was uplifted and exposed while the lower Paleozoic sedimentary cover was folded (Kerr 1977). Steeply dipping reverse faults that define the western margin of the uplift grade northward (where shallower structural levels are exposed) into thrust faults associated with overturned folds, further evidence of thick-skinned deformation (Kerr 1977)(Fig. 4.14b). During the Late Devonian to Early Pensylvanian Ellesmerian Orogeny, south-directed shortening produced the Parry Islands fold belt on Bathurst and Mellville islands and the Central Elsmerian fold belt on Devon Island. The Parry Islands fold belt is thin-skinned, with a detachment level at the Ordovician Bay Fiord evaporites (Harrison *et al.* 1991). In the Cornwallis fold belt, however, strata underlying the Bay Fiord Formation were deformed during the Ellesmerian Orogeny (Kerr 1976), evidence that the Bay Fiord Formation was not everywhere the detachment zone.

Although buckling of competent Ordovician and Silurian carbonate strata likely controlled the fold style, unlike the models, dome-and-basin interference patterns dominate the intersection of the Parry Island and Cornwallis fold belts. The north-trending Boothia Horst may have served as a rigid buttress, which somewhat protected the Cornwallis folds from being refolded normal to their axial surfaces. On eastern Bathurst Island, near the western margin of the basement uplift, north-trending left-lateral strike-slip faults that are parallel to the basement margin further suggest the impedence of southerly transport (Kerr 1977).

Another example of dome-and-basin interference at the intersection of two fold belts occurs in the High Atlas range of Morocco (de Sitter 1952). Non-metamorphosed, interbedded massive carbonates and marls comprise a high competence-contrast stratigraphy that deformed by buckling. Because the NE-SW Pyrenean trend and the (younger) E-W Vindobonian trends are well-defined elsewhere in North Africa, the sense of superposition can locally be determined (de Sitter 1952).

Additionally, domes and basins may occur at the intersection of two fault trends. Rare domes and basins occur near Kingston, NY, where the NE-trending Kittatiny-Shawangunk fold and thrust belt overprints the N-S-trending, Hudson Valley fold and thrust belt (Marshak & Tabor 1989). This noncylindrical fold style characterizes only the area (approximately 3 km by 3 km) where the two differently oriented segments of the fold belt meet. Similarly, in northern Alabama the intersection of thrusts from the Alleghenian trend and the Ouachita trend produced local dome-and-basin style interference (Tull 1984).

SUMMARY

Comparison of the models with several field examples of buckle-style fold interference allows generalizations beyond the simple deformation and boundary conditions of the models. Buckle-style fold interference is not as common a structural style as similar-style fold interference that characterizes the deep metamorphic cores of orogens. Nonetheless, examples of buckle-style fold interference demonstrates that it occurs in a range of rock types, deformation conditions, and tectonic settings. Lithologies that deform by buckling include

carbonates, quartzites, volcaniclastics, and their metamorphic equivalents. Several of the field examples included an evaporite detachment layer (e.g. Kerr 1977, Schwerdtner *et al.* 1988), implying that km-wavelength buckling is facilitated where a rheologic detachment is present. Buckle interference is not restricted to sedimentary rocks, but also occurs in higher grade rocks where a structural anisotropy developed during early deformation, and later deformation occurred at lower temperatures (e.g. Schwerdtner & van Berkel 1991). At shallow crustal levels, faults as well as folds control regional interference and local accommodation of bi-directional curvature (e.g. Tull 1984, Marshak & Tabor 1989, Stewart 1993, Alvarez-Marron 1995). Tectonic settings of buckle-fold interference range from arcuate fold and thrust belts (Julivert & Marcos 1973) to subduction zones (Kano *et al.* 1990). Results of the models can therefore be applied to predict and interpret fold interference geometry in a broad array of lithologic and tectonic settings.

Chapter 5. Application of Physical Models to the Narragansett Basin, Rhode Island

The southern Narragansett Basin is characterized by a complex polydeformational history. Extensive coastal outcrops along Narragansett Bay beautifully expose in three dimensions multiple generations of folds and foliations. Because of the discontinuous outcrop and scale of the different fold generations, the fold interference is not expressed as kilometer-scale map patterns. Previous detailed mapping and correlation of the minor structures, however, has shown that the interference of the fold generations and their relative orientation varies across the basin. Results from the physical models can help interpret the heterogeneous polyphase deformation in the southern Narragansett Basin, Rhode Island.

Structural Styles in the Southern Narragansett Basin

The Narragansett Basin is a composite graben filled with Pennsylvanian alluvial fan sediments (Mosher 1983, Skehan *et al.* 1986) (Fig. 5.1). During the Alleghenian Orogeny, the sediments were metamorphosed and deformed in several phases associated with basin closure and subsequent transcurrent shear (Mosher 1983). Metamorphic grade generally increases from chlorite and biotite grade in the east to sillimanite grade in the western part of the basin (Mosher 1983). The polydeformation is expressed by several generations of minor folds and foliations, which vary in style and orientation across the southern basin.

Throughout the basin, N to NNE trending, subhorizontal, early fold generations (F_1, or locally F_{1a} and F_{1b}, and F_2) are nearly coaxially superposed

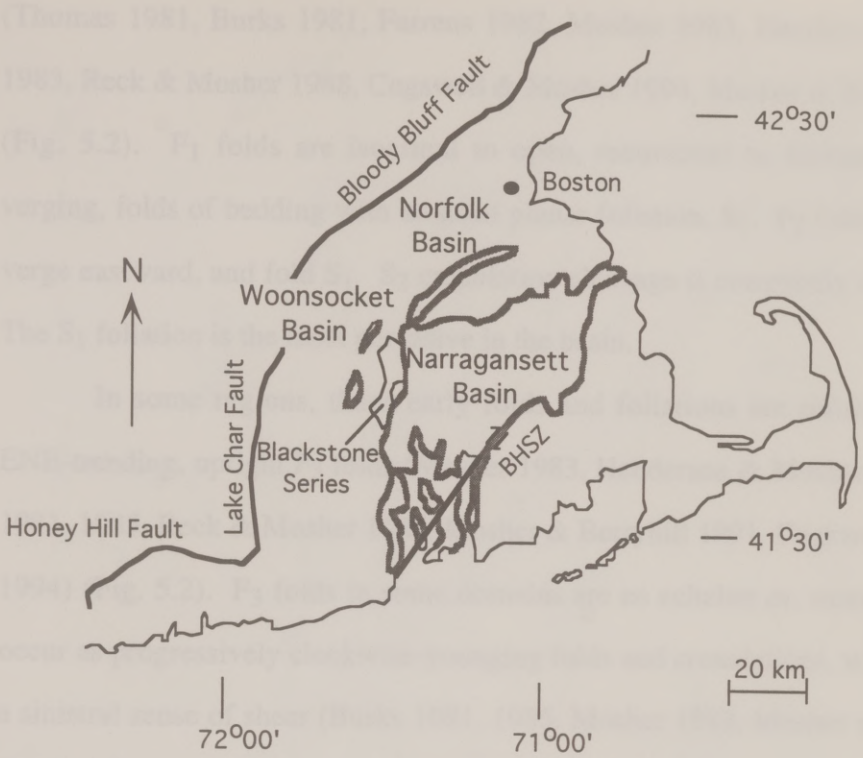

Figure 5.1 Location map of the Narragansett Basin (after Snoke & Mosher 1989, Figure 36). BHSZ is the Beaverhead shear zone.

(Thomas 1981, Burks 1981, Farrens 1982, Mosher 1983, Henderson & Mosher 1983, Reck & Mosher 1988, Cogswell & Mosher 1994, Mosher & Berryhill 1991) (Fig. 5.2). F_1 folds are isoclinal to open, recumbent to inclined, westward verging, folds of bedding with an axial planar foliation, S_1. F_2 folds are upright, verge eastward, and fold S_1. S_2 crenulation cleavage is commonly oblique to S_1. The S_1 foliation is the most pervasive in the basin.

In some regions, these early folds and foliations are refolded by E- to ENE-trending, upright F_3 folds (Mosher 1983, Henderson & Mosher 1983, Burks 1981, 1985, Reck & Mosher 1988, Mosher & Berryhill 1991, Cogswell & Mosher 1994) (Fig. 5.2). F_3 folds in some domains are en echelon or, more commonly, occur as progressively clockwise-younging folds and crenulations, which indicate a sinistral sense of shear (Burks 1981, 1985, Mosher 1983, Mosher and Berryhill 1991). F_3 folds are most common in a broad NE-trending zone, named the Beaverhead Shear Zone (BHSZ) (Mosher 1983) (Fig. 5.1). Associated with the BHSZ are N- to NNE-trending sinistral faults mapped on land and parallel lineaments in the basin floor inferred to be sinistral faults (Mosher & Berryhill 1991, Henderson unpublished work) (Fig. 5.3). F_3 folds also occur in isolated regions outside of the BHSZ (Fig. 5.2). Rare, E-trending F_3 folds occur as kinks of the S_1 foliation on Aquidneck Island (Farrens 1982), as folds of the S_1 foliation on northern Conanicut Island (Burks 1981, Henderson & Mosher 1983), as folds of bedding and S_1 on the eastern margin (Mosher unpublished work), and are inferred from a ENE-trending foliation on Hope Island (Thomas 1981). Near the western basin margin, S_3 forms a pervasive and predominant foliation, and F_3 axes range in orientation from N to E (Cogswell & Mosher 1994).

Figure 5.2. Minor F_1, F_2, and F_3 fold axes in the southern Narragansett Basin. F_4 fold axes are omitted for clarity. Data are compiled from Thomas (1981), Farrens (1982), Burks (1981, 1985), Reck & Mosher (1988), Mosher & Berryhill (1991), Cogswell & Mosher (1994), and Mosher (unpublished data). A=Aquidneck Island, C=Conanicut Island, BH=Beaverhead region of Conanicut Island, D=Dutch Island, G=Gould Island, H=Hope Island, P=Prudence Island, and BHSZ=Beaverhead Shear Zone.

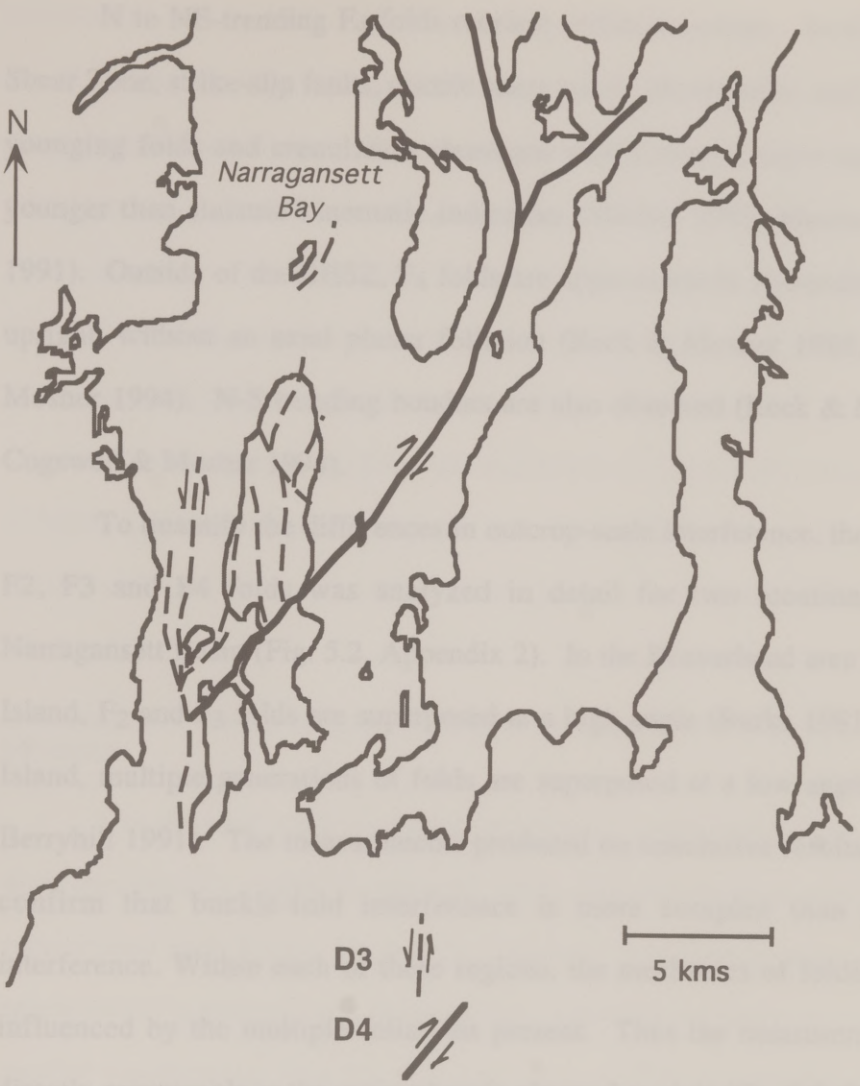

Figure 5.3. Strike-slip faults in the southern Narragansett Basin (after Mosher & Berryhill 1991, Cogswell & Mosher 1994).

N to NE-trending F_4 folds reorient earlier structures. In the Beaverhead Shear Zone, strike-slip faults, ductile shear zones, sheath folds, and progressively younging folds and crenulation cleavages with a dextral sense are everywhere younger than sinistral kinematic indicators (Mosher 1983, Mosher & Berryhill 1991). Outside of the BHSZ, F_4 folds are approximately N-trending, open, and upright, without an axial planar foliation (Reck & Mosher 1988, Cogswell & Mosher 1994). N-S trending boudins are also observed (Reck & Mosher 1988, Cogswell & Mosher 1994).

To quantify the differences in outcrop-scale interference, the geometry of F2, F3 and F4 folds was analyzed in detail for two locations within the Narragansett Basin (Fig. 5.2, Appendix 2). In the Beaverhead area of Conanicut Island, F_2 and F_3 folds are superposed at a high angle (Burks 1981). On Dutch Island, multiple generations of folds are superposed at a low angle (Mosher & Berryhill 1991). The measurements produced no conclusive results, but they do confirm that buckle-fold interference is more complex than passive-fold interference. Within each of these regions, the mechanics of folding are likely influenced by the multiple foliations present. Thus the measurements are not directly comparable to the regional-scale physical models (Ch. 2 & 3).

Tectonic History of the Narragansett Basin

The structures in the Narragansett Basin formed during E-W basin contraction and subsequent sinistral and dextral shear, according to Mosher (1983) (Fig. 5.4). During the initial collision of North America and Africa, progressive D1 and D2 shortening produced the generally N-trending, coaxially

refolded F_1 and F_2 folds. D3 deformation is concentrated in, but not limited to, the NE-trending Beaverhead Shear Zone. Mosher (1983) proposed that the Beaverhead Shear Zone comprises basement faults reactivated as sinistral R' reidel shears to a dextral megashear system between the African and North American plates. Sinistral reactivation of other basement faults, including the nearly N-trending basin margins, formed E- to NNE-trending F_3 folds (Henderson & Mosher 1983, Cogswell & Mosher 1994). Further dextral motion of a NE-trending transform system (D4) caused the dextral reactivation of the BHSZ and of NE to ENE basement faults, resulting in N- to NE- trending folds, boudins, and dextral strike-slip faults and shear zones (Mosher & Berryhill 1991, Cogswell & Mosher 1994).

COMPARISON OF NARRAGANSETT STRUCTURES WITH THE PHYSICAL MODELS

The physical models of fold interference described in Chapters 2 and 3 were dynamically scaled to represent folds sufficiently large to be affected by gravitational body forces. D1 and D2 folds have wavelengths up to 1.5 km, so are appropriately compared with these models. D3 folds, however, tend to occur with smaller wavelengths (less than 0.2 km), and the fold interference occurs at the outcrop-scale. Thus the local fold interference may be better compared with previous models that had insignificant gravitational body forces (e.g., Watkinson 1981, Ghosh *et al.* 1992, 1993, Grujic 1993). Nevertheless, the similarity between models in this study and previous models, and the regional-scale of interference heterogeneity in Rhode Island, allows direct comparison of the models and the structures in the Narragansett Basin.

The superposition of ENE-trending D3 structures on N-trending D1 and D2 structures in the Narragansett Basin is analogous to superposed shortening in the physical models (Ch. 2). The consistent overprinting of D1/D2 structures by D3 structures rules out interference caused by coeval shortening, analogous to the models described in Ch. 3. Interbedded phyllites, quartzites, meta-siltstones and metaconglomerates of the Rhode Island Formation likely had a high competence-contrast as they deformed, as demonstrated by local changes in fold style from open in coarser-grained units to chevron in phyllites (Mosher & Helper 1988 p. 371). Physical models of superposed shortening of a high competence-contrast laminate have laterally heterogeneous interference styles. Accordingly, the models provide insight into the irregular distribution of structures of different generations in the Narragansett Basin. Further, highly oblique basin boundaries separate the rigid basement from the less competent basin fill. The natural boundary conditions thereby approximate the rigid, orthogonal boundaries of the models.

In the model with <20% D1 shortening, the distribution and amplitude of F_1 folds affected the interference pattern (Ch. 2, Figs. 2.7). Where F_1 folds were initially absent or poorly developed, that is, where they had low amplitude, only the F_2 fold trend is evident. Elsewhere in the same model, F_1 folds are the dominant trend. Similarly in the Narragansett Basin, some regions are characterized by D1 and D2 structures, but show little if any evidence of D3 deformation. Examples include Prudence Island (Thomas 1981), most of Aquidneck Island (Mosher 1978, Farrens 1982), and northeastern Conanicut Island (Henderson & Mosher 1983). In other domains of the model, the F_1

hingelines and axial traces were folded in a Type 2 interference style. These regions are similar to areas of the Narragansett Basin where F_3 folds are highly oblique to earlier F_1-F_2 folds. Examples of oblique interference are the western basin margin (Reck & Mosher 1987, Cogswell & Mosher 1994), the Beaverhead area and Jamestown Bridge area of Conanicut Island (Burks 1981, Henderson & Mosher 1983), near Portsmouth Abbey on Aquidneck Island (Farrens 1982), and on the southeastern basin margin (Mosher unpublished). Comparison with the models suggests that the sporadic distribution of D3 structures may depend on the initial size and style of earlier structures. The scale of F_1 and F_2 folds depends on lithology (Hermes *et al.* 1994). F_3 folds are found in graphitic schists and phyllite, and rarely in fine-grained sandstone. Where present, F_3 folds are of the same general scale (less than 0.2 km wavelength) as the F_1 and F_2 folds. No F_3 folds are observed where the massive sandstones and conglomerates are folded into larger wavelength (0.5-1.3 km) F_1 and F_2 folds.

Additionally, the physical models include zones of concentrated deformation. In models with >20% D1 shortening, the interference style was commonly kink-like (e.g., c218, D1=54% D2=20%, Ch. 2, Figs. 2.8a, b). Within conjugate zones of high strain, D2 deformation was intense, PL layers were faulted, and grid markers were offset. Outside of the conjugate zones, there was little evidence of D2 shortening. In a similar manner, effects of D3 deformation are concentrated in (but not limited to) the NE trending Beaverhead Shear Zone (Burks 1982, Mosher 1983, Mosher & Berryhill 1991, Cogswell & Mosher 1994). Within the BHSZ, deformation is intense. Outside of the BHSZ, there are no

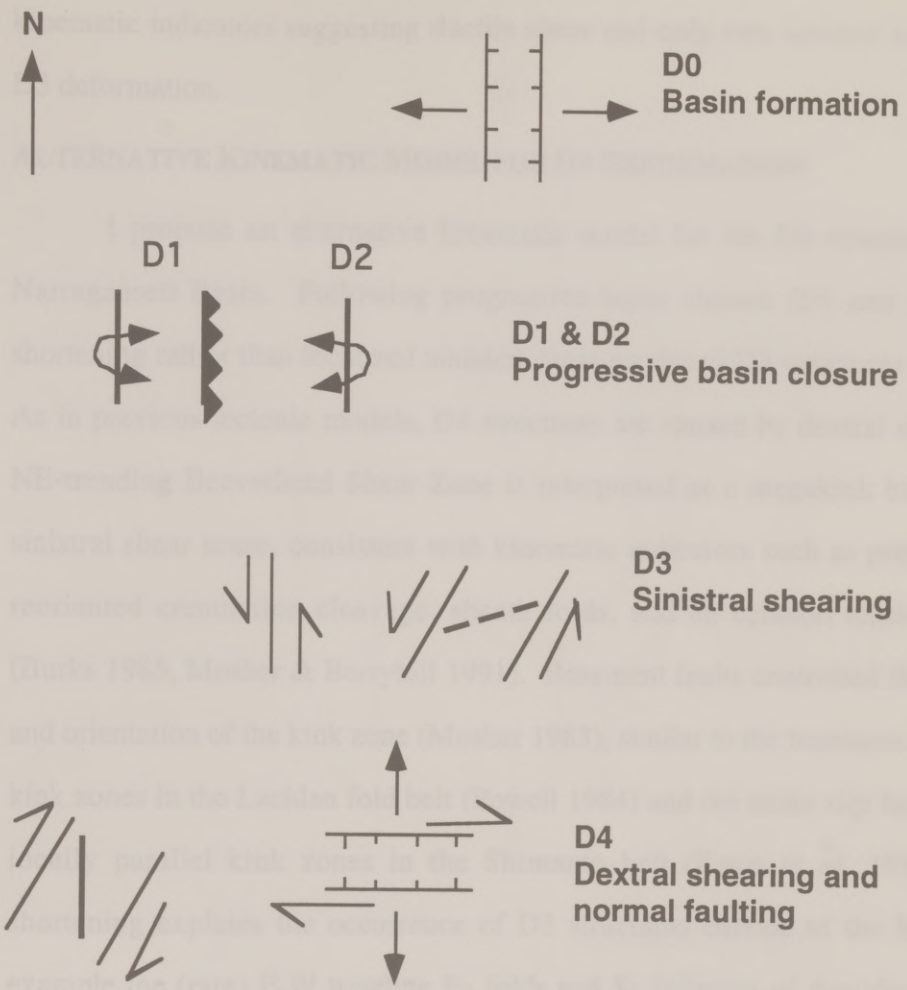

Figure 5.4. Schematic tectonic history of the southern Narragansett Basin. Bold lines represent fold axis trends (based on Mosher 1983).

kinematic indicators suggesting ductile shear and only rare isolated examples of D3 deformation.

Alternative Kinematic Model for D3 Deformation

I propose an alternative kinematic model for the D3 structures in the Narragansett Basin. Following progressive basin closure (D1 and D2), N-S shortening rather than localized sinistral shear produced D3 structures (Fig. 5.5). As in previous tectonic models, D4 structures are caused by dextral shear. The NE-trending Beaverhead Shear Zone is interpreted as a megakink band with a sinistral shear sense, consistent with kinematic indicators such as progressively reoriented crenulation cleavage, sheath folds, and en echelon tension gashes (Burks 1985, Mosher & Berryhill 1991). Basement faults controlled the location and orientation of the kink zone (Mosher 1983), similar to the basement control of kink zones in the Lachlan fold belt (Powell 1984) and the strike slip faults which locally parallel kink zones in the Shimanto belt (Kano *et al.* 1990). N-S shortening explains the occurrence of D3 structures outside of the BHSZ, for example the (rare) E-W trending F_3 folds and S_3 foliation of Aquidneck Island (Farrens 1982), Hope Island (Thomas 1981), the Beaverhead area of Conanicut Island (Burks 1982), northern Conanicut Island (Henderson & Mosher 1983), and the southeastern basin margin (Mosher unpublished work). The heterogeneous distribution of D3 structures outside of the BHSZ may be related to the initial distribution, style, and scale of earlier structures.

The proposed model agrees with much, but not all, of the field data. N-S shortening is inconsistent with N- to NNE- trending F_3 folds described in the

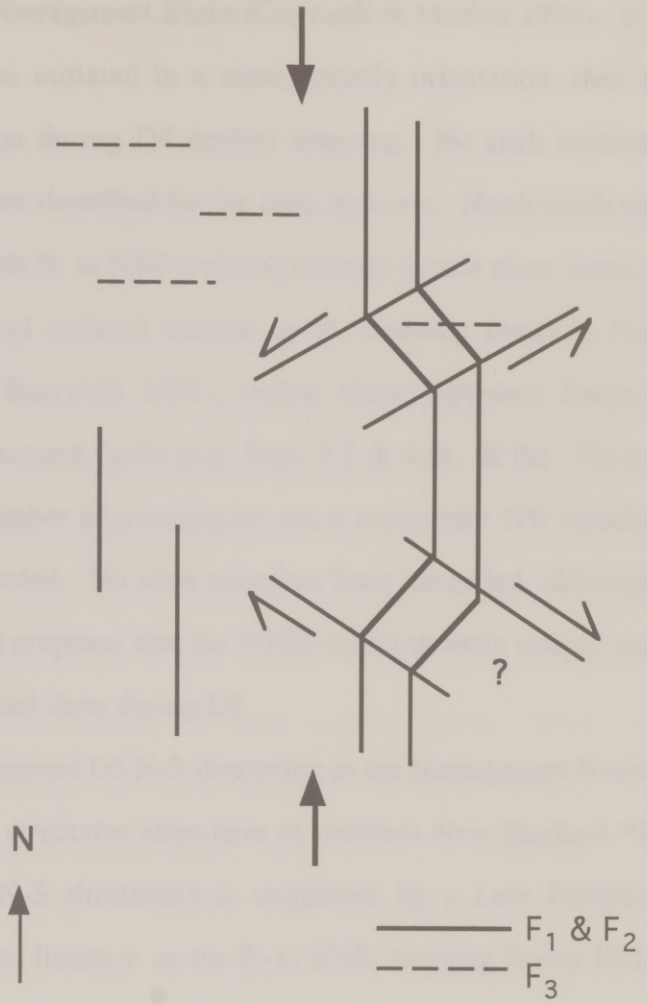

Figure 5.5. Alternative kinematic model for the D3 structures in the Narragansett Basin. N-S shortening produced a NE-trending, sinistral kink band (the Beaverhead Shear Zone). Corresponding dextral, SE trending kink bands have not been mapped.

southwestern Narragansett Basin (Cogswell & Mosher 1994). It is possible that these structures initiated in a more easterly orientation, then rotated to their present position during D4 dextral shearing. No such evidence of fold axis rotation has been described for the area, however. North-south shortening is also inconsistent with N- to NNE-trending sinistral ductile shear zones on Dutch Island and the inferred sinistral motion on N- trending faults in Narragansett Bay (Mosher and Berryhill 1991), unless these represent fanned kink axes or preexisting basement faults (e.g. Figs. 4.7 & 4.8). If the NE-trending sinistral BHSZ is a member of a conjugate set, a concurrent NW-trending dextral zone would be expected. No such zone has been identified, although Cogswell and Mosher (1994) proposed that the WNW-trending basin margin was reactivated as a dextral R' riedel shear during D3.

The proposed D3 N-S shortening in the Narragansett Basin correlates with late Paleozoic structures elsewhere in southern New England. In south-central Connecticut, N-S shortening is suggested by a Late Permian ESE-to-SSW trending mineral lineation on the E- to ENE- trending Honey Hill Fault (Wintsch & Sutter 1986)(Fig. 5.1). Additionally, the proposed model accounts for the superposition of N-S by E-W trending Alleghenian fold axes in the Precambrian Blackstone Series (Dreier 1985) and in the (probably) Carboniferous Woonsocket basin to the northwest of the Narragansett basin (Snoke & Mosher 1989), as well as the generally E-W trending fold axes in the Carboniferous Norfolk Basin, southeastern Massachusetts (Cazier 1987) and northern Narragansett Basin (Snoke & Mosher 1989). A change from E-W shortening to N-S shortening in southern New England may require a change in orientation in Africa's plate

motion relative to North America during the Permian to Early Triassic (Wintsch & Sutter 1986).

TESTS AND IMPLICATIONS OF THE PROPOSED MODEL

Both the proposed model of N-S shortening and the previous model of sinistral shear account for the main D3 structural styles: E-W trending fold axes and sinistral shear kinematic indicators within a NE-trending zone. Testing these two hypotheses can be used to guide future field work and regional correlation. For sinistral shear, D3 structures would preferentially occur in discrete zones, and commonly be accompanied by clear kinematic indicators. Determination of a sinistral shear sense on ductile or brittle faults outside of the BHSZ or in other contemporaneous basins would further support the shear hypothesis. For N-S shortening, E-W trending F_3 folds and S_3 foliation would be the dominant structures. D3 structures would be more regionally pervasive than if they were exclusively associated with shear zones. Kinematic indicators suggesting sinistral shear would occur in NE-trending zones and dextral shear in NW-trending zones (Fig. 5.5). Kink zones might also fan in orientation (cf. Figs. 2.8 & 4.6). Mutually cross-cutting kink zones would be further evidence that they formed concurrently and accommodated regional shortening. If N-S shortening were caused by major reorientation of plate motions, contemporaneous features in southern New England should show E-W trending folds and N- or S-directed thrusts. Such a change in plate motion may also be expressed in paleomagnetic data for rocks of both North American and African affinity.

SUMMARY

In sum, the physical models suggest that the heterogeneous distribution of D3 structures in the Narragansett Basin is partly the result of heterogeneity inherent to superposed buckling and may also be due to a component of N-S shortening. Application of this alternative hypothesis can explain some data inconsistent with previous models of D3 deformation. Testing of this hypothesis can be used to guide future fieldwork and to aid correlation of the structural styles in the southern Narragansett with Alleghenian deformation elsewhere.

Chapter 6. Conclusions

Physical models of non-coaxial, regional-scale fold interference demonstrate that the interference style is influenced by the rheology of the material deformed, the deformation history, the gravitational body forces, and the boundary conditions (Fig 6.1).

Low competence-contrast layering has a simple, homogeneous interference style because it accommodates shortening by a combination of layer-parallel shortening and buckling. High competence-contrast layering has a more heterogeneous and complex interference style because individual layers as well as the multilaminate package buckle.

Sequentially shortened, high competence-contrast layering preferentially forms complex Type 2 interference patterns. Coevally shortened, high competence-contrast layering forms elongate domes and basins, which plunge shallowly but trend variably. Although sequentially and coevally shortened structures locally resemble one another, the regional structural styles are distinct.

Gravitational body forces effectively damp vertical fold amplification. Gravitational body forces may thereby accentuate the development of Type 2 fold interference during sequential shortening and constrain the fold plunge during coeval shortening.

In the models, near-field rigid boundaries affect the orientation, amplitude, and extension direction of structures. Natural, far-field boundaries are expected to have a similar (though less pronounced) control of fold interference.

The combined effects of the above parameters cause fold interference to be heterogeneous laterally and with depth. Application of the physical models to natural examples can be used to recognize and interpret the sources of such heterogeneities.

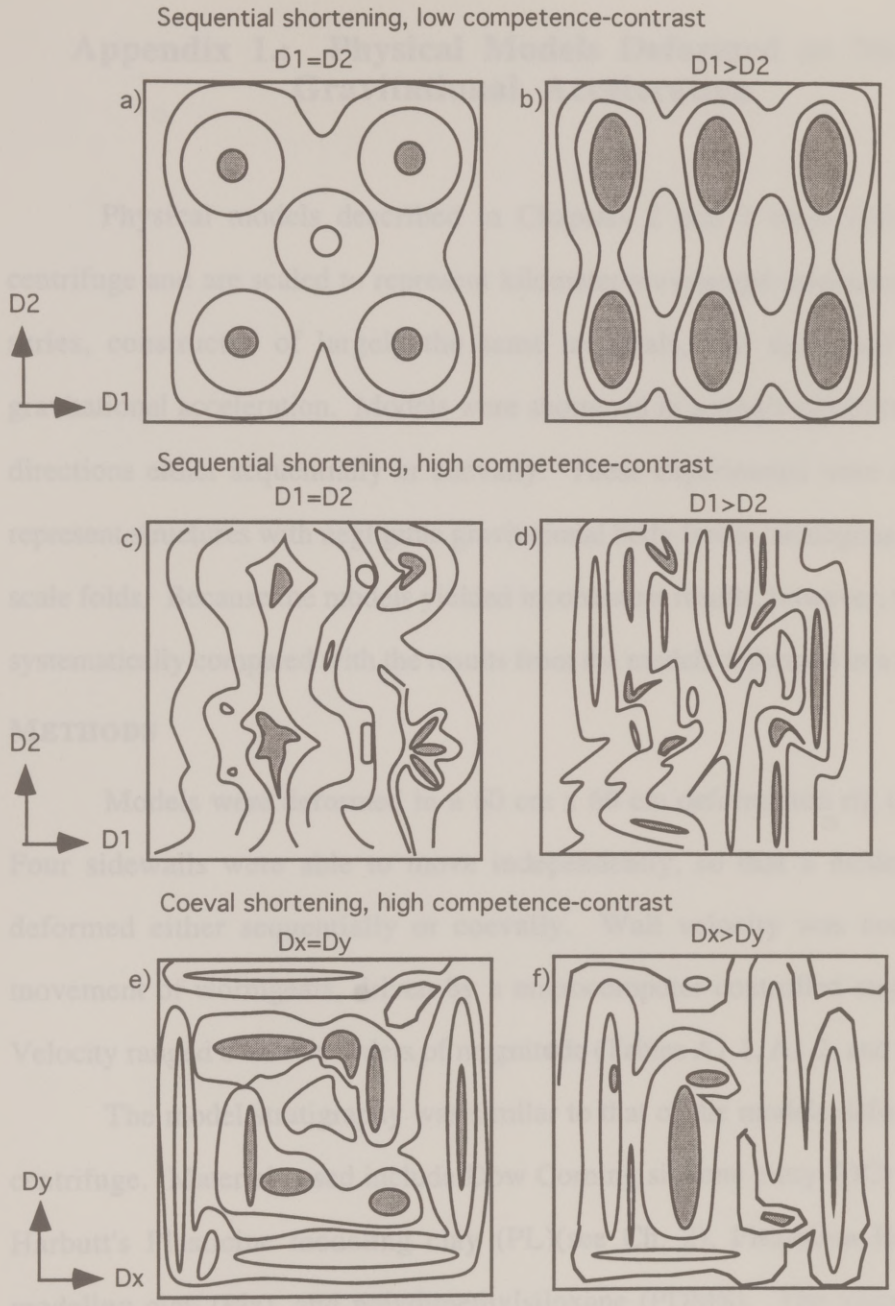

Figure 6.1. Schematic representation of the range of fold interference styles produced in this study.

Appendix 1.: Physical Models Deformed at Normal Gravitational Acceleration

Physical models described in Chapters 2 and 3 were deformed in a centrifuge and are scaled to represent kilometer-wavelength structures. Another series, constructed of largely the same materials, was deformed at normal gravitational acceleration. Models were shortened in a single direction, or in two directions either sequentially or coevally. These experiments were designed to represent structures with negligible gravitational body forces, analogous to outcrop-scale folds. Because the models yielded inconsistent results, however, they are not systematically compared with the results from the models deformed in a centrifuge.

METHODS

Models were deformed in a 60 cm x 60 cm deformation rig (Fig. A1.1). Four sidewalls were able to move independently, so that a model could be deformed either sequentially or coevally. Wall velocity was controlled by movement of wormgears, driven by a microcomputer-controlled stepper-motor. Velocity ranged over two orders of magnitude (Tables A1.1, A1.2, and A1.3).

The model stratigraphy was similar to that of the models deformed in the centrifuge. Materials used include Dow Corning silicone putty (DC) (see Ch.2), Harbutt's Plasticine modeling clay (PL)(see Ch. 2), Plastalina Hardness #1 modeling clay (Pla), and polydimethylsiloxane (PDMS). The viscosity of the Plastalina was not measured. Qualitatively, however, it behaved similar to the Harbutt's Plasticine. Plastalina was substituted for PL in some models because it

Figure A1.1 Schematic diagram of the deformation rig for normal gravitational acceleration experiments. (a) Plan view. Four sidewalls are displaced independently by four motor-driven wormgears. (b) Cross section. The walls are attached to the wormgears by metal rails, which slide along ball bearings. The rails allow the walls to be displaced simultaneously in two orthogonal directions.

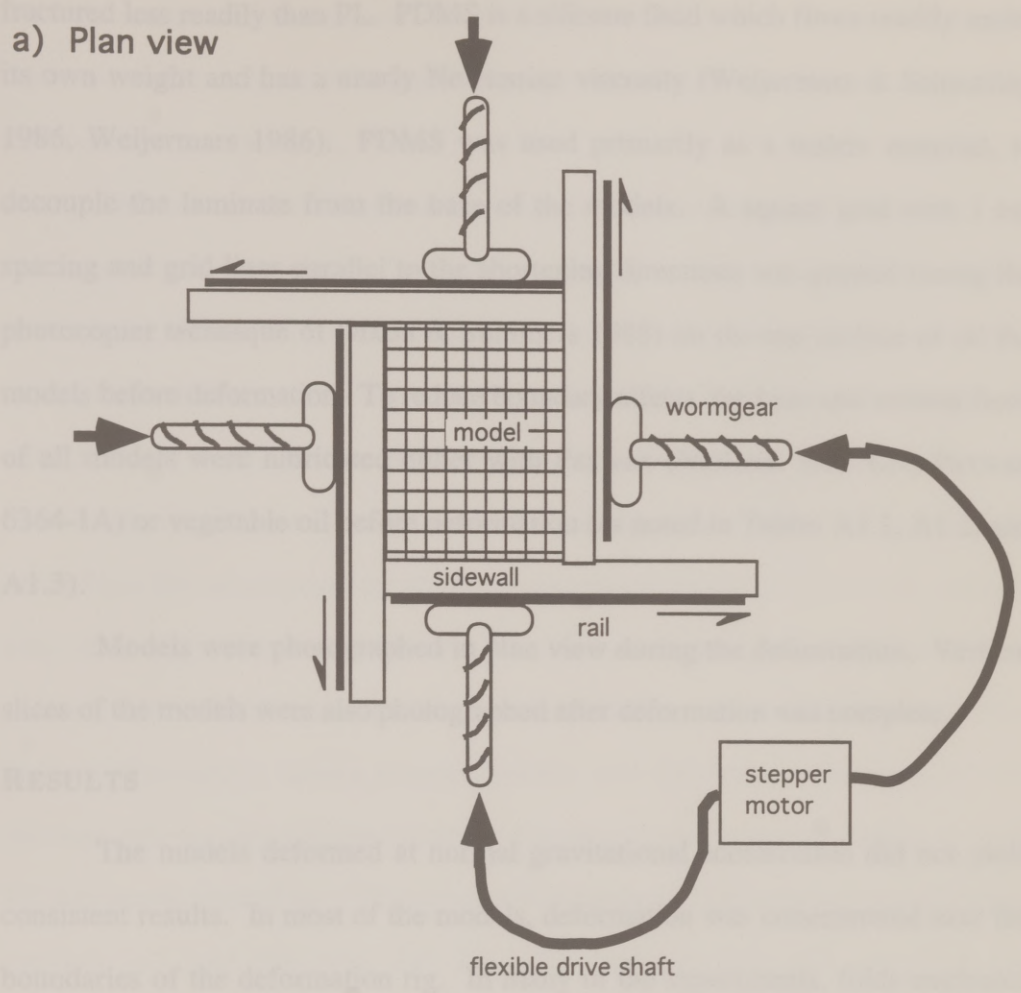
a) Plan view
model
wormgear
sidewall
rail
stepper
motor
flexible drive shaft

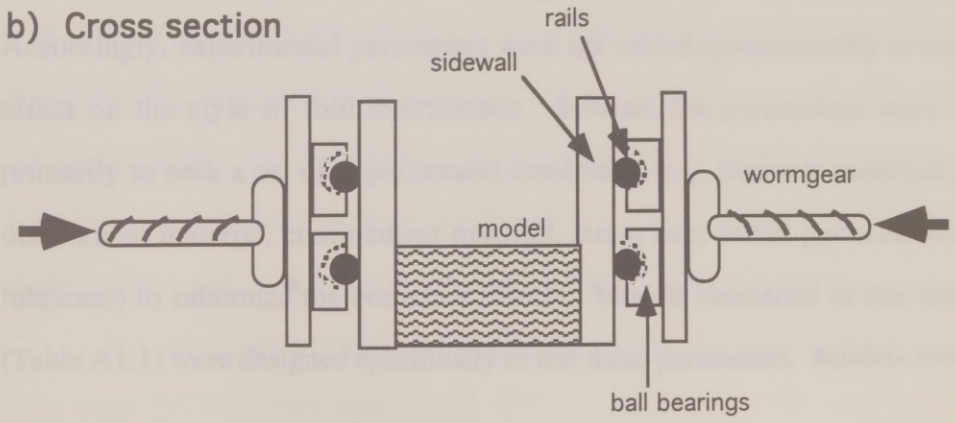
b) Cross section
rails
sidewall
wormgear
model
ball bearings

fractured less readily than PL. PDMS is a silicone fluid which flows readily under its own weight and has a nearly Newtonian viscosity (Weijermars & Schmeling 1986, Weijermars 1986). PDMS was used primarily as a matrix material, to decouple the laminate from the base of the models. A square grid with 1 cm spacing and grid lines parallel to the shortening directions was printed (using the photocopier technique of Dixon & Summers 1985) on the top surface of all the models before deformation. To reduce boundary effects, the base and vertical faces of all models were lubricated either with Paxwax (National Wax Co., Paxwax 6364-1A) or vegetable oil before deformation (as noted in Tables A1.1, A1.2, and A1.3).

Models were photographed in plan view during the deformation. Vertical slices of the models were also photographed after deformation was complete.

RESULTS

The models deformed at normal gravitational acceleration did not yield consistent results. In most of the models, deformation was concentrated near the boundaries of the deformation rig. In many of the experiments, folds nucleated near the model boundaries and continued to amplify until the laminate fractured. Accordingly, experimental parameters were not varied systematically to test their effect on the style of fold interference. Instead, the parameters were varied primarily to seek a set of experimental conditions (e.g. laminate materials, basal detachment material, confinement material, strain rate, initial perturbations, and lubricant) to minimize the boundary effects. Models shortened in one direction (Table A1.1) were designed specifically to test these parameters. Models shortened

in two directions, either sequentially (Table A1.2) or coevally (Table A1.3), were designed to test whether deformation history was a more significant variable than the boundary conditions.

The most pronounced boundary effects occurred in models with no basal detachment unit (model 120, Table A1.2). In this model, all deformation of the interlayered DC and PL occurred at the model boundary, forming a bowl-shaped basin. To better decouple the laminate from the base, subsequent models were built with different basal detachments (PDMS or DC) of various thickness or different basal lubricants (Paxwax or vegetable oil). Additionally, to introduce perturbations away from the boundaries, some laminates were thinned by up to 20% (models 136, 150, 153, 171, 178, 179, 180, and 181) or were indented by metal rods (models 278, 279, 280, and 281). To reduce brittle failure of the laminate, less viscous Pla and Pla mixed homogeneously with DC were substituted for PL. Because the viscosities of the materials decreased with decreasing strain-rate (e.g. Weijermars & Schmeling 1986), some models were also deformed at low velocities (models 183, 184, 216, 275, 276, 277, 278, 279, 280, 281, 282, 285, 289, and 292). To test if the deformation would be distributed more evenly for a flexural slip fold mechanism, in one model (292) individual layers were lubricated with vegetable oil. These different techniques reduced, but by no means eliminated the boundary effects. Even in models where deformation was not concentrated at the boundary, deformation was poorly distributed. Where the laminate was indented in several places, one fold typically amplified at the expense of other folds.

The least pronounced boundary effects occurred in two types of models. In first type, DC was interlayered with PDMS (models 95, 109, and 112). Both

materials have a low viscosity compared with PL and Pla. Although folds initiated near and parallel to the moving sidewalls, folds also formed in the central regions of the models. Because the PDMS is affected by significant gravitational body forces, it is an inappropriate material to represent outcrop-scale structures, so it was used in few models. The second category of models with reduced boundary effects had a thick, strong confining unit (models 182 and 185). These 15 cm long models were shortened in one direction. Their laminates of DC and Pla were incased in a matrix of a thin layer of DC and a thicker layer of Pla (Table A1.1). The laminate buckled in a series of 2 cm wavelength folds, and the matrix thickened approximately uniformly. When a larger model (model 186, 26 cm by 26 cm) was built with the same stratigraphy and was shortened in two directions, the confining unit buckled and faulted. The behavior of the thick confining unit controlled the structures of the laminate below it (as it did in a preliminary centrifuge experiment, Ch. 2). In two subsequent models (models 196 and 216) lead shot was used to weigh down the Pla confining unit. As the Pla unit deformed, however, the lead shot flowed away from the locus of amplification, so was not an effective confinement.

DISCUSSION

Despite the strong boundary effects, some models had similarities in their style of fold superposition with the models deformed in the centrifuge (Ch. 2 and Ch. 3). A sequentially shortened model with high competence contrast (model 136) formed dominantly Type 2 interference. A coevally shortened model with high competence contrast (model 126) formed elongate domes and basins which were oriented parallel to the sidewalls near the boundaries. The similarities between the

models deformed at normal and increased gravitational acceleration suggest that although gravitational body force may modify fold interference, it is less significant than parameters such as deformation history.

Deformation propagated away from the boundaries in the unconfined centrifuge models (Ch. 2 and 3), in the unconfined models with weak materials deformed at normal gravity, and in the models with a strong confinement unit deformed at normal gravity. Both the confining unit and gravitational body forces evidently damped vertical structural growth. The precise mechanism relating limitation of amplification and distribution of deformation is unclear, however. In the models, folds typically first nucleated adjacent to the moving walls (or rams in the centrifuge models). Amplification of these folds was restricted by a confining layer or by the laminates' gravitational body forces. Apparently, it was energetically more favorable for perturbations to nucleate and grow away from the moving wall than for the initial folds to continue to amplify. In this manner folds nucleate and propagate away from the moving wall. This mechanism of fold propagation and amplification may be analogous to the critical taper model of thrust belt accretion (Davis *et al.* 1983), whereby the gravitational force of the material in the hinterland helps drive the active deformation in the foreland, at the toe of the wedge.

TABLE A1.1 MODELS SHORTENED IN ONE DIRECTION

Exp. #	Stratigraphy			Deformation		Comments
	materials	n	h(mm)	%strain	v(cm/hr)	
95	PDMS(top)	1	10	42	19	
	PDMS	1	10			
	DC	2	5			
	PDMS(base)	1	10			
178	Pla(top)	1	25	20	9.5	thinned laminate
	DC	5	1			
	Pla	5	1			
	Pla(base)	1	25			
179	DC(top)	1	25	20	9.5	thinned laminate
	DC	4	1			
	Pla	4	1			
	DC(base)	1	25			
180	Pla(top)	1	20	20	9.5	thinned laminate
	DC	4	1			
	Pla	4	1			
	DC	2	5			
	Pla(base)	1	20			
181	Pla(top)	1	25	20	9.5	
	DC	5	1			
	Pla	4	1			
	Pla(base)	1	25			
182	Pla(top)	1	20	20	9.5	
	DC	1	5			
	DC	9	1			
	Pla	8	1			
	DC	1	5			
	Pla(base)	1	20			
183	PDMS(top)	1	25	20	1	
	DC	2	4			
	Pla	2	1			
	PDMS(base)	1	25			
184	PDMS(top)	1	25	20	1	
	DC	3	4			
	Pla	2	1			
	PDMS(base)	1	25			

Table A1.1 (continued)

Exp. #	Stratigraphy			Deformation		Comments
	materials	n	h(mm)	%strain	v(cm/hr)	
185	Pla(top)	1	50	20	4.76	
	DC	1	5			
	DC	9	1			
	Pla	8	1			
	DC	2	5			
	Pla(base)	1	50			
275	DC	3	2	11.5	0.5	veg. oil lubricant
	Pla	3	2			
	DC (base)	1	7			
276	DC	3	2	7.5	0.5	veg. oil lubricant
	Pla	3	2			
	DC	1	10			
	dense silicone (base)	1	2			
277	DC	3	5	7.4	0.1	veg. oil lubricant
	Pla	3	2			
	DC (base)	1	10			
278	DC	3	2	15.8	0.03	indented laminate
	Pla	3	2			
	DC (base)	1	10			
279	DC	4	2	13	0.03	indented laminate
	Pla	4	2			
	DC(base)	1	10			
280	DC	4	2	6.3	0.03	indented laminate
	Pla-DC	4	2			
	DC(base)	1	10			
281	DC	5	2	7.4	0.02	indented laminate
	Pla-DC	5	2			
	DC(base)	1	10			
285	DC	4	2		0.08	partial lubricant
	Pla-DC	4	2			
	DC(base)	1	10			
289	DC	4	2	18	0.3	
	Pla-DC	4	2			
	DC(base)	1	10			

Table A1.1 (continued)

Exp. #	Stratigraphy			Deformation		Comments
	materials	n	h(mm)	%strain	v(cm/hr)	
292	DC	4	2	12.2	0.1	interlaminar lubricant
	Pla-DC	4	2			
	DC(base)	1	10			

PDMS=polydimethylsiloxane
DC=Dow Corning bouncing putty
PL=Harbutt's Plasticine modeling clay
Pla=Plastilina #1 modelclay
n=number of layers
h=thickness of each layer
v=velocity

TABLE A1.2 MODELS SHORTENED SEQUENTIALLY

Exp.#	Stratigraphy			Deformation				Comments
	materials	n	h(mm)	%strain		v(cm/hr)		
				D1	D2	D1	D2	
132	PDMS (top)	1	10	27	27	10	10	
	PL	4	2					
	DC	4	2					
	PDMS(base)	1	10					
136	PDMS (top)	1	10	18	18	20	20	
	PL	4	2					
	DC	4	2					
	PDMS(base)	1	10					
150	PL	2	2	14	14	10	10	
	DC	2	2					
	PDMS	1	10					
166	PDMS	1	10	18	30	13	13	
	PL	5	1					
	DC	5	1					
	PDMS(base)	1	10					
171	PDMS(top)	1	25	20	20	7	7	
	PL	5	2					
	DC	5	2					
	PDMS(base)	1	25					
176	DC(top)	1	30	16	16	10	10	
	PL	1	2					
	DC(base)	1	30					
186	Pla(top)	1	50	20	20	4.76	4.76	
	Pla	9	1					
	DC	3	1					
	DC	2	5					
	Pla (base)	1	25					
189	PDMS (top)	1	10	20	20	14.3	19	
	DC	1	5					
	PDMS(base)	1	40					
196	Pla (top)	1	50	20	20	1.5	1.5	25 lbs Pb shot added to top
	DC	1	5					
	DC	8	1					
	PL	9	1					
	DC	1	5					
	Pla (base)	1	20					

Table A1.2 (continued)

Exp.#	Stratigraphy			Deformation				Comments
	materials	n	h(mm)	%strain		v(cm/hr)		
				D1	D2	D1	D2	
216	Pla (top)	1	10	15	25	0.5	0.5	50 lbs
	DC	1	5					Pb shot
	DC	8	1					added to top
	PL	9	1					
	DC(base)	1	5					
282	DC	5	2	8	12.6	0.5	0.5	
	Pla-DC	5	2					
	DC(base)	1	10					

PDMS=polydimethylsiloxane
DC=Dow Corning bouncing putty
PL=Harbutt's Plasticine modeling clay
Pla=Plastilina Hardness#1 modeling clay
Pla-DC=homogeneous mixture of Pla & DC
n=number of layers
h=thickness of each layer
v=velocity

TABLE A1.3 MODELS SHORTENED COEVALLY

Exp.#	Stratigraphy			Deformation			
	materials	n	h(mm)	%strain		v(cm/hr)	
				Dx	Dy	Dx	Dy
109	PDMS	2	10	30	30	20	20
	DC	1	5				
112	PDMS	3	6	30	30	20	20
	DC	3	3				
120	PL	3	3	30	30	20	20
	DC	4	3				
126	PDMS	1	10	20	20	10	10
	PL	4	2				
	DC	4	2				
	PDMS(base)	1	10				
153	PL	2	2	16	16	3	3
	DC	2	2				
	PDMS(base)	1	15				

PDMS=polydimethylsiloxane
DC=Dow Corning bouncing putty
PL=Harbutt's Plasticine modeling clay
n=number of layers
h=thickness of each layer
v=velocity

Appendix 2. Field Measurements from the Narragansett Basin

Detailed fold geometry of outcrop-scale fold interference from two regions of the Narragansett Basin, Rhode Island was measured during the summer of 1992 (see Ch. 5 for description of regional structural styles). Coastal outcrops beautifully expose in three-dimensions outcrop-scale fold interference on the Beaverhead area of Conanicut Island and on Dutch Island (Figs. 5.2, A2.1 and A2.2). Although separated by only a few kilometers, the two regions display different styles of fold interference and have different kinematic histories. In the Beaverhead area, upright F_2 and F_3 folds are noncoaxially superposed at nearly right angles, and the interference styles include Type 1 and Type 2 (Burks 1981). On Dutch Island, multiple generations of upright folds and crenulations are superposed at a low angles. The fold interference is expressed as sinuous hinge lines and as domes and basins, interpreted to have formed during first sinistral then dextral shearing (Mosher and Berryhill 1991). Both regions have been mapped in detail (Burks 1981, Berryhill 1984), and the significance of the local deformation to local kinematics and the regional tectonics has been previously discussed (Burks 1981, Burks 1985, Mosher and Berryhill 1991). The geometry of fold interference was measured to test to what extent the geometry of fold interference, as opposed to crosscutting relationships among different generations of foliations, reflects the kinematics of fold superpostion. Additionally, the fold geometry was measured for comparison with physical models. Because the physical models deformed in the

centrifuge (Ch. 2 and Ch. 3) were scaled to represent regional structures, and because physical models deformed at normal gravitational acceleration gave inconsistent and incomplete results (Appendix 1), direct comparison of the physical models and the field measurements is inappropriate. Moreover, the field measurements from the two regions proved to be insufficient to characterize the differences in their kinematic histories.

METHODS

Both field areas were divided into several measurement stations (Figs. A2.1 and A2.2), subdivided into smaller regions (e.g. Location 3A), and further subdivided into individual folds (e.g. Location 3A, fold 1). I measured the variation of fold hinge orientation, fold amplitude, wavelength and interlimb angle along strike or at different depths (Tables A2.1 and A2.2). Because of the orientation and size of the surface exposed, not all parameters were measured at all stations. Where outcrops exposed the top of deformed surfaces, the fold hinge trend and plunge, fold amplitude, and interlimb angle were measured in plan view at 5 cm intervals. Where outcrops exposed cross sections through the structures, variation in the same geometric parameters could be measured with depth.

RESULTS

The measurements document a variation in fold geometry within and across domains. Equal-area projections show variation in fold hinge orientation of a single fold hinge, of different fold hinges within a measurement station, and of the two field areas (Fig. A2.3). Fold amplitude, wavelength, and interlimb angle plotted against the length of traverse along individual fold hinges describes changes in the

geometry of individual folds (Fig. A2.4). Neither the stereograms nor the fold geometry graphs yielded plots characteristic of the structural style of each domain. The results show as much variation between adjacent folds within measurement stations as between measurement stations, or within a the Beaverhead domain as between Beaverhead and Dutch Island. Systematic measurement of fold geometry therefore may aid the description of interference style, but is not diagnostic of the kinematics of the interference style.

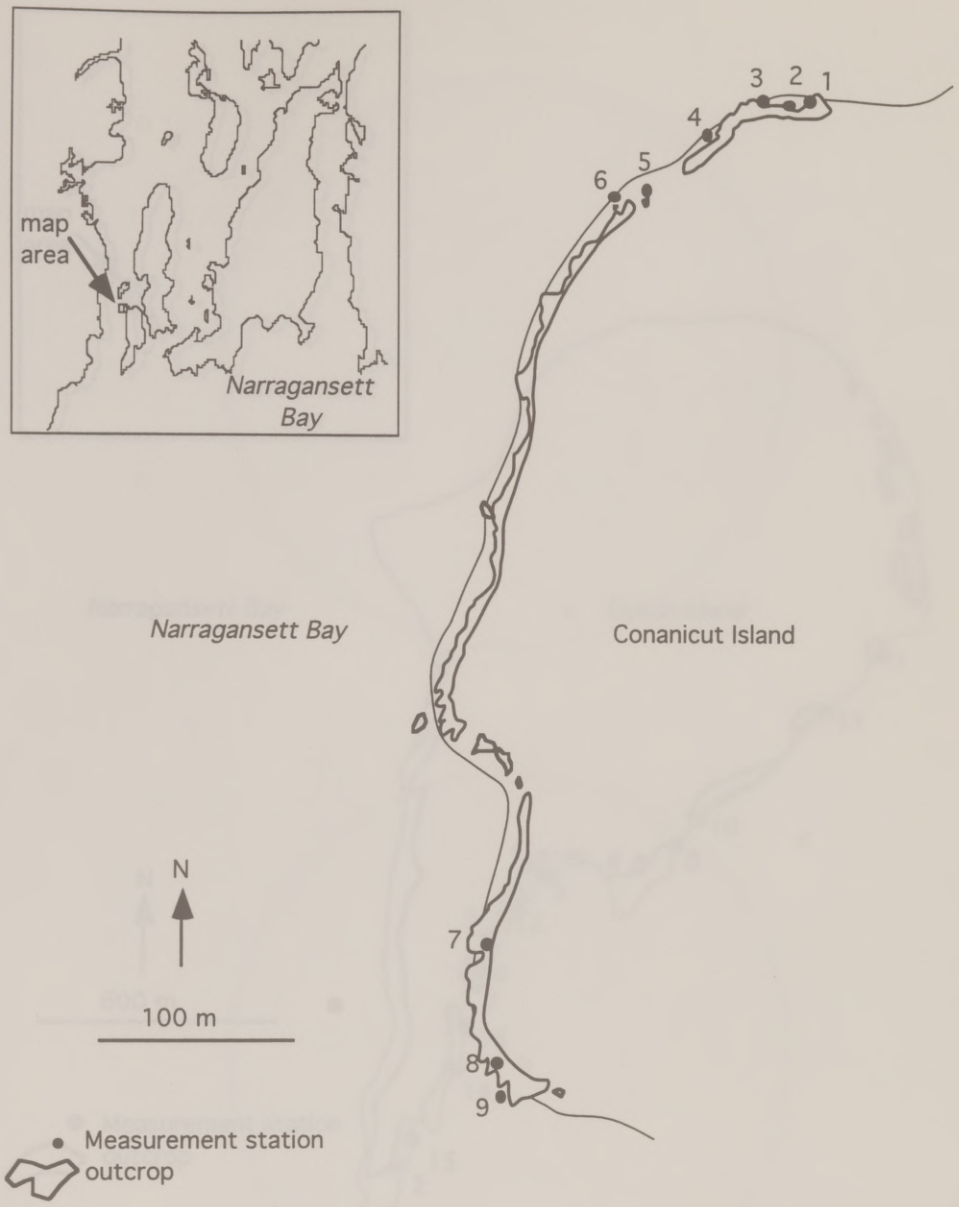

Figure A2.1 Sample location map, Beaverhead area, Conanicut Island (after Fig. 5, Burks 1981). Numbers refer to measurement stations listed in Tables A2.1 and A2.2.

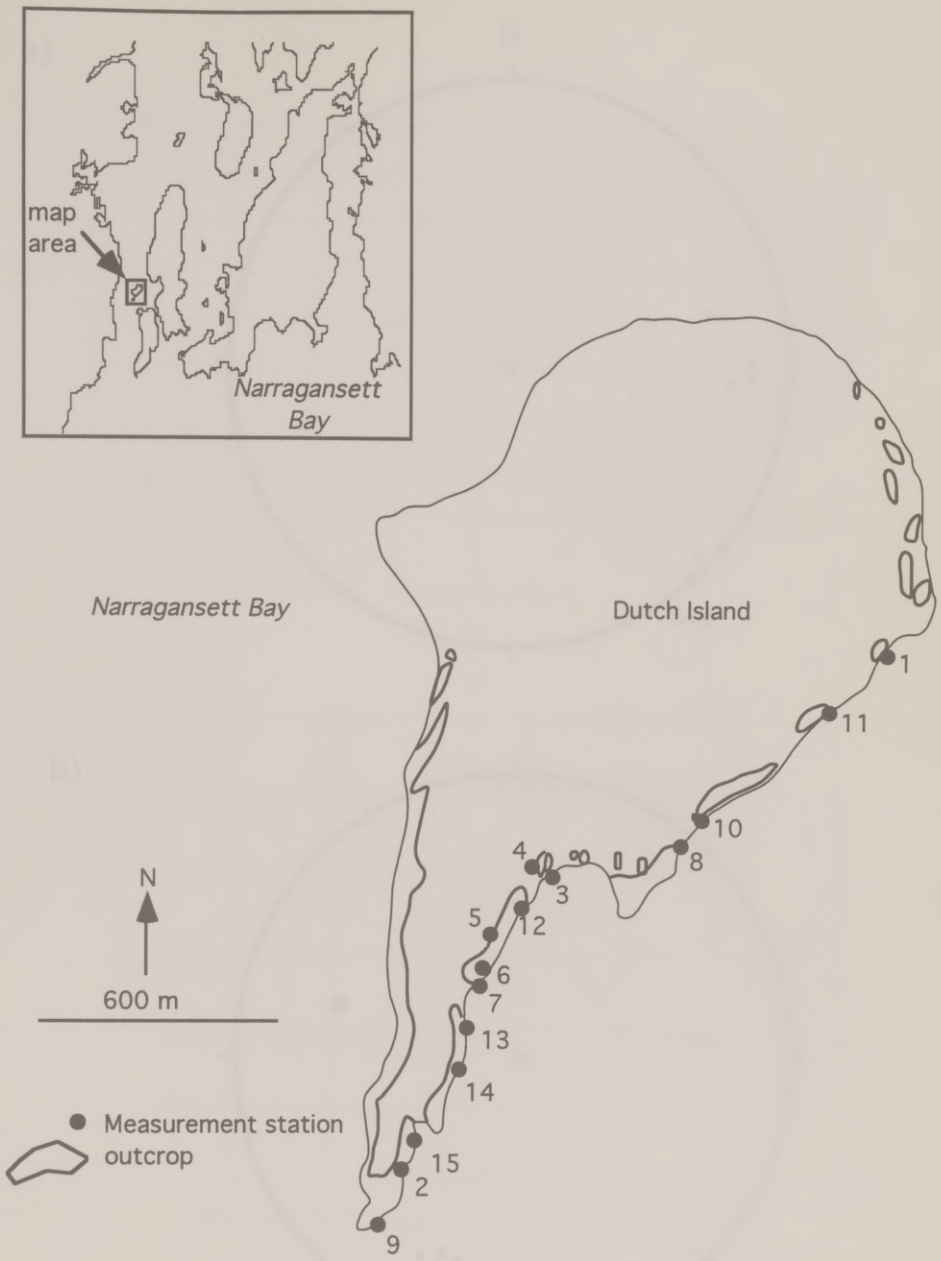

Figure A2.2 Sample location map, Dutch Island (after Fig.2, Berryhill 1984). Numbers refer to measurement stations listed in Tables A2.1 and A2.2.

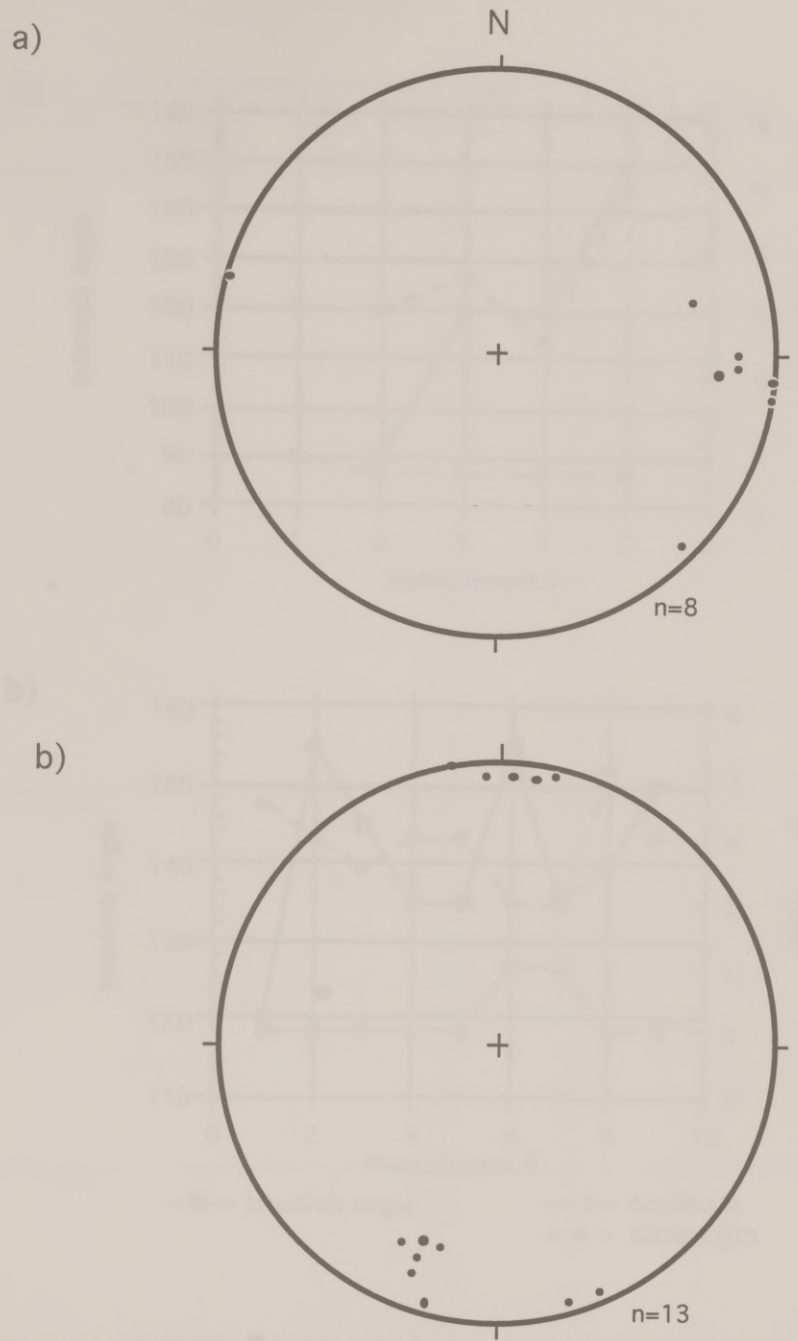

Figure A2.3 Representative equal-area projections illustrating the variation in the orientation of an individual fold hinge, measured at 5 cm intervals along its trend. (a) Location 3F Beaverhead, Conanicut Island. (b) Location 2C, Dutch Island.

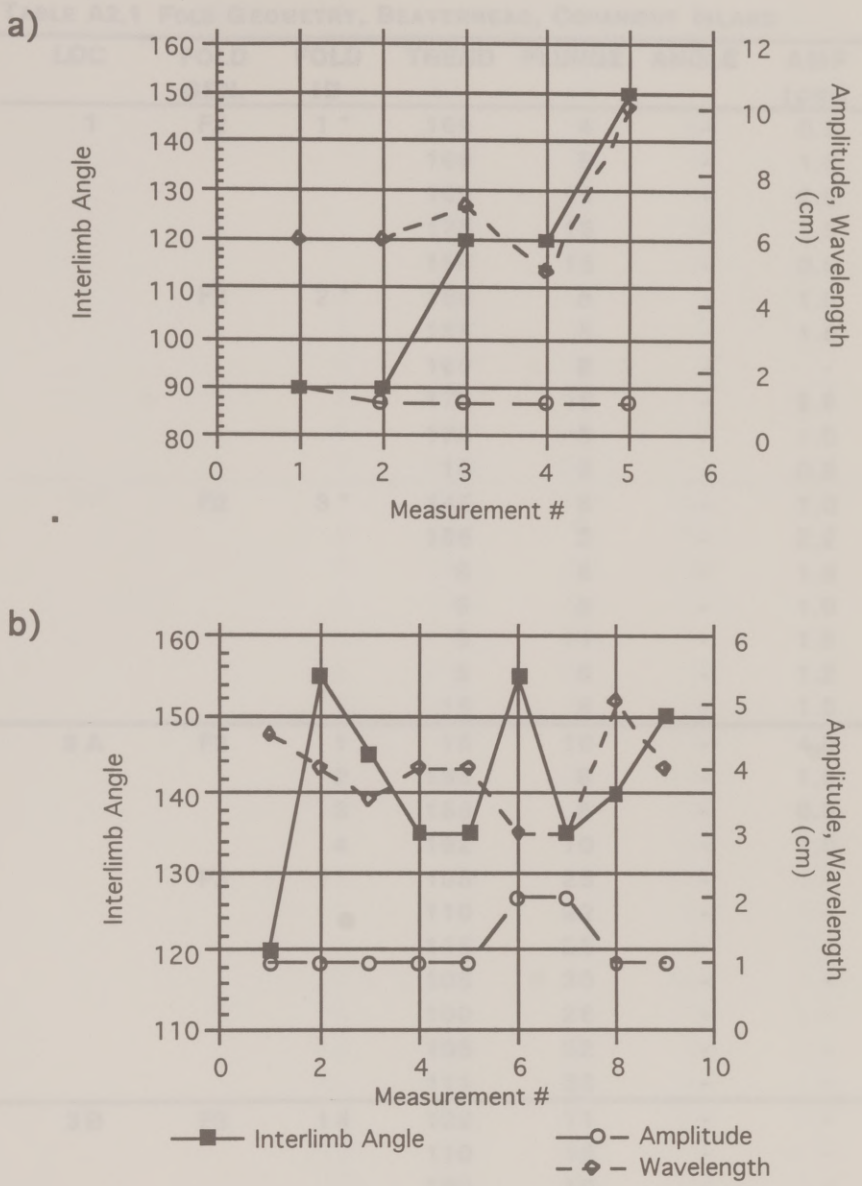

Figure A2.4 Variation in amplitude, interlimb angle, and wavelength of an individual fold, measured at 5 cm intervals along its trend. (a) Example from Location 3F, Beaverhead region. (b). Example from Location 9D, Dutch Island.

TABLE A2.1 FOLD GEOMETRY, BEAVERHEAD, CONANICUT ISLAND

LOC	FOLD GEN.	FOLD ID	TREND	PLUNGE	ANGLE	AMP (cm)	WL (cm)
1	F2	1 *	169	4	-	0.5	-
			166	5	-	1.5	-
			165	15	-	2.0	-
			175	15	-	1.5	-
			160	15	-	0.5	-
	F2	2 *	150	8	-	1.9	-
			155	5	-	1.8	-
			160	6	-	-	-
			172	10	-	2.0	-
			175	5	-	1.0	-
			10	5	-	0.8	-
	F2	3 *	145	5	-	1.0	-
			165	2	-	2.2	-
			8	6	-	1.3	-
			5	5	-	1.0	-
			5	11	-	1.6	-
			5	6	-	1.2	-
			15	8	-	1.0	-
3 A	F2	1	15	10	-	4.0	4.0
		2	195	8	-	1.0	5.0
		3	188	6	-	0.5	3.0
		4	192	10	-	1.0	16.0
	F3	1 *	105	25	-	-	-
			110	32	-	-	-
			115	25	-	-	-
			105	30	-	-	-
			100	26	-	-	-
			105	32	-	-	-
			111	33	-	-	-
3 B	F3	1 #	122	11	-	-	-
			110	15	-	-	-
			100	10	-	-	-
			115	40	-	-	-
			145	56	-	-	-
			123	35	-	-	-
			100	34	-	-	-
			105	30	-	-	-
3 C	F3	1 #	127	45	90	-	-

Table A2.1 (continued)

LOC	FOLD GEN.	FOLD ID	TREND	PLUNGE	ANGLE	AMP (cm)	WL (cm)
			220	50	45	-	-
			125	40		-	-
			110	72	60	-	-
			115	73	35	-	-
			118	20	60	-	-
			125	35	75	-	-
			125	35	70	-	-
		2	125	20	-	-	-
		3	118	38	-	-	-
		4	115	48	-	-	-
		5	102	45	-	-	-
		6	120	46	-	-	-
		7	122	52	-	-	-
3D	F3	1	130	10	110	-	2.0
		2	107	3	135	-	25.0
		3	127	22	143	-	-
		4	115	22	-	-	-
		5	145	40	-	-	-
		6	112	37	45	-	7.0
		7	113	49	90	-	-
4A	F3	1	150	50	100	-	-
		2	125	30	155	-	-
		3	70	2	120	1.0	2.0
		4	130	42	115	1.5	8.0
		5	115	34	100	3.0	5.0
		6	110	35	65	2.0	4.0
		7	115	36	65	2.5	3.0
		8	125	20	140	1.0	3.0
		9	105	40	110	1.0	2.0
		10	105	0	85	2.0	5.0
		11	75	9	90	4.0	7.0
		12	110	20	150	3.0	8.0
		13	85	25	100	50.0	30.0
		14	100	34	115	4.0	15.0
		15	115	35	90	2.0	2.0
		16	135	55	100	2.0	2.0
4C	F3	1 *	110	24	115	1.0	6.0
			125	55	90	2.0	4.0
			128	36	110	1.0	5.0
			125	34	115	1.0	4.0

Table A2.1 (continued)

LOC	FOLD GEN.	FOLD ID	TREND	PLUNGE	ANGLE	AMP (cm)	WL (cm)
			129	30	115	0.5	1.0
		2	138	44	90	1.0	3.0
		3	144	28	60	6.0	7.0
		4	128	44	90	13.0	4.0
		5	115	34	-	-	-
		6	122	80	110	10.0	15.0
		7	130	35	120	3.0	3.0
		8	125	46	90	-	3.0
		9	130	51	112	2.0	5.0
		10	80	55	45	10.0	10.0
4D	F2	1	326	15	120	1.0	2.0
		2	327	18	115	1.5	2.0
		3	333	15	130	1.0	3.0
		4	22	60	90	2.0	2.0
		5	310	55	160	1.0	7.0
	F3	1#	135	29	115	1.0	3.0
			146	20	140	3.0	15.0
			130	32	120	1.0	3.0
			130	29	120	3.0	3.0
			135	35	90	2.0	15.0
			121	20	110	3.0	4.0
			115	40	60	1.0	9.0
			95	55	120	4.0	2.0
			108	27	90	3.0	9.0
			85	23	150	3.0	4.0
			108	39	120	3.0	6.0
			122	36	140	3.0	20.0
			131	70	100	2.0	4.0
4E	F2	1*	220	16	150	30.0	40.0
			215	14	-	-	-
			215	10	-	-	-
			208	10	-	-	-
			220	10	-	-	-
			205	12	-	-	-
			200	13	-	-	-
			198	10	-	-	-
		2*	55	14	120	3.0	15.0
			45	11	120	3.5	12.0
			38	12	120	3.0	10.0
			50	15	120	4.0	9.0

Table A2.1 (continued)

LOC	FOLD GEN.	FOLD ID	TREND	PLUNGE	ANGLE	AMP (cm)	WL (cm)
			65	10	115	4.0	10.0
			35	0	90	5.0	11.0
			203	5	95	5.0	15.0
			230	10	120	7.0	16.0
			225	25	120	7.0	19.0
			220	15	140	2.0	12.0
			205	11	150	1.0	2.0
		3 *	205	85	150	4.0	21.0
			208	6	140	4.0	20.0
			220	4	160	5.0	20.0
			44	4	150	5.0	20.0
			30	6	120	3.0	15.0
			45	9	120	3.0	15.0
			35	6	120	3.0	9.0
			50	6	110	3.0	4.0
			35	21	120	2.0	4.0
			25	54	150	1.0	4.0
		4 *	50	2	120	1.5	9.0
			50	5	120	1.5	9.0
			210	20	140	1.0	7.0
4E	F3	1	125	20	150	15.0	30.0
		2	75	46	120	1.0	3.0
		3	245	60	150	2.0	5.0
		4	230	30	120	2.0	10.0
		5	255	2	150	1.0	10.0
		6	245	15	160	1.0	15.0
4F	F2	1	185	5	-	1.0	3.0
		2	130	10	-	2.0	3.0
		3	260	35	-	-	-
	F3	1	271	5	-	-	-
		2	255	25	-	-	-
		3	260	54	120	1.0	4.0
		4	100	24	150	2.0	9.0
		5	145	6	130	3.0	10.0
		6	120	25	120	2.0	6.0
		7	190	24	150	3.0	13.0
4G	F2	1	50	36	160	1.0	4.0
		2	40	16	120	2.0	4.0
		3	48	45	100	2.0	4.0
		4	68	24	110	1.0	3.0

Table A2.1 (continued)

LOC	FOLD GEN.	FOLD ID	TREND	PLUNGE	ANGLE	AMP (cm)	WL (cm)
	F3	1	65	55	150	1.0	6.0
		2	170	19	95	4.0	15.0
		3	130	40	85	7.0	11.0
		4	140	45	60	7.0	10.0
		5	130	29	90	3.0	10.0
		6	132	46	95	2.0	4.0
		7	148	42	160	2.0	9.0
5 A	F2?	1 *	120	42	150	0.5	3.0
			120	53	140	0.5	5.0
			127	39	130	1.0	3.0
			125	33	150	1.0	3.0
			90	6	150	0.5	4.0
			102	10	160	0.5	4.0
			85	14	120	2.0	4.0
	F3?	1 *	175	32	120	2.0	7.0
			175	24	130	1.5	6.0
			165	25	150	1.0	4.0
			150	41	130	1.5	4.0
			178	30	150	1.0	3.0
			175	15	160	1.0	6.0
6		1.a*	43	11	-	-	-
			74	11	85	0.7	0.6
		1.b*	56	19	150	0.5	1.0
			26	2	150	0.5	0.5
		1.c*	50	19	110	0.8	1.0
			34	2	90	0.3	1.0
		1.d*	40	34	140	0.5	1.5
			32	6	100	0.5	5.0
		1.e*	34	41	160	0.2	3.0
			49	10	90	0.5	5.0
		2 *	226	5	-	-	-
			35	9	-	-	-
			23	5	90	0.5	1.0
			18	9	-	-	-
			13	9	-	-	-
		4.a*	105	0	170	0.1	1.2
			55	18	160	0.5	2.5
			44	11	170	0.1	1.5
			45	20	100	0.5	1.0
		4.b*	75	5	150	0.5	1.0

Table A2.1 (continued)

LOC	FOLD GEN.	FOLD ID	TREND	PLUNGE	ANGLE	AMP (cm)	WL (cm)
			45	10	120	0.5	0.8
			39	3	90	1.0	3.0
			210	3	150	1.5	3.2
		4.c*	216	6	170	0.5	1.0
		5 *	41	9	90	0.5	1.0
			26	9	90	1.0	2.0
			6	5	90	1.0	1.8
			14	4	150	0.8	1.5
		6.a*	29	10	110	0.5	0.5
			49	6	150	1.0	0.5
			0	4	150	2.0	0.5
			204	6	120	1.5	1.0
			39	5	110	5.0	2.5
			35	20	100	2.5	1.5
			19	15	90	1.0	0.5
		6.b*	89	15	170	1.0	0.5
			85	4	160	2.0	1.0
			84	29	170	1.0	0.5
			84	15	160	2.0	0.5
		6.c*	60	6	150	1.0	0.5
			85	10	160	2.5	0.5
			85	60	120	5.0	1.0
			80	17	170	2.0	2.0
	F2	7 *	54	11	120	0.5	1.0
			39	20	90	0.8	1.0
			34	44	110	0.8	1.5
			15	3	130	0.5	1.5
7 A	F2	1	275	15	-	2.0	3.0
		2	260	30	-	2.0	5.0
		3	240	22	-	0.5	1.0
		4	60	5	-	1.0	2.0
		5	235	5	-	3.0	6.0
		6	220	10	-	1.0	2.0
		7	40	8	-	1.0	2.0
		8	200	11	-	4.0	10.0
	F3	1	52	34	-	2.0	3.0
		2	355	60	-	4.0	15.0
7 B	F2	1	265	30	-	10.0	50.0
		2	245	6	-	1.0	5.0
		3	245	42	-	2.0	3.0

Table A2.1 (continued)

LOC	FOLD GEN.	FOLD ID	TREND	PLUNGE	ANGLE	AMP (cm)	WL (cm)
	F3	1 *	226	40	150	2.0	-
			235	35	120	4.0	10.0
			240	30	90	4.5	9.0
			18	2	80	4.0	7.0
			203	10	110	2.0	6.0
			205	15	150	1.0	3.0
		2 *	236	30	90	2.0	5.0
			235	19	85	4.0	5.0
		3 *	210	34	120	-	-
			207	41	120	-	-
			205	38	145		-
		4 *	22	6	-	1.0	3.0
			24	20	-	3.0	8.0
			222	21	-	1.0	1.0
			35	20	-	1.0	3.0
			230	19	-	0.5	1.0
			225	35	-	3.0	5.0
			211	2	-	3.0	5.0

LOC = location, see Fig. A2.1
FOLD GEN. = fold generation, from Burks 1981
FOLD ID = fold identification
ANGLE = interlimb angle
AMP = amplitude
WL = wavelength
- = not measured
= measurements at different depths of a single fold hinge
* = measurements along strike of a single fold hinge

TABLE A2.2 FOLD GEOMETRY, DUTCH ISLAND

LOC	FOLD ID	TREND	PLUNGE	ANGLE	AMP(CM)	WL(CM)
1A		190	22	180	0.5	1.5
		192	20	150	1	5
		200	16	125	5	7
		206	16	105	6	17
		202	15	90	7	17
		210	16	100	7	17
		212	16	100	4	20
		215	16	90	4	17
		213	12	120	4	17
		204	12	130	3	17
1B	1	212	12	140	2	-
		219	20	140	3	-
		219	20	130	3	-
		215	21	130	3	-
		216	25	105	3	-
		221	21	105	4	-
		222	23	105	3	-
		228	20	150	2	-
		220	25	145	1	-
		224	30	150	1	-
		225	34	155	1	-
		225	40	165	2	-
		215	30	130	2	-
1B	2	218	33	175	2	2
		210	35	155	3	3
		205	38	140	3	5
		205	24	125	3	8
		210	36	110	4	9
		218	21	115	5	9
		220	18	110	5	9
		220	17	130	5	9
		224	20	130	5	9
		226	20	140	4	8
		226	15	140	3	4
		230	10	140	3	3
1C	1	209	17	90	2	5
		216	18	100	3	5
		211	19	100	2	4
		210	24	105	2	4

LOC	FOLD ID	TREND	PLUNGE	ANGLE	AMP(CM)	WL(CM)
		219	15	100	3	4
		219	10	100	3	4
		216	25	80	3	4
		216	15	130	3	2
		212	6	120	3	3
		212	8	120	3	3
1C	2	206	29	130	0.5	1
		213	22	125	1	3
		220	16	130	1	3
		222	20	130	0.5	3
1C	3	216	11	-	0.5	1
		219	14	120	1	2
		214	12	-	0.5	1
1C	4	210	16	-	0.5	2
		210	20	100	2	2
		213	18	-	2	3
2A	1	167	29	130	-	-
		163	26	145	-	-
		161	25	180	-	-
		164	16	180	-	-
		164	24	130	-	-
		175	11	120	-	-
		180	20	120	-	-
		178	18	110	-	-
		188	14	125	-	-
		165	28	128	-	-
2A	2	185	22	90	-	-
		188	10	-	-	-
		200	20	150	-	-
		190	19	110	-	-
		177	20	140	-	-
2A	3	175	15	60	2	-
		180	19	60	-	-
		188	18	60	1	-
		190	20	60	-	-
		192	29	130	-	-
		184	28	120	-	-
		184	24	130	-	-
		184	16	150	-	-
		172	32	180	-	-

LOC	FOLD ID	TREND	PLUNGE	ANGLE	AMP(CM)	WL(CM)
3	1	18	4	125	1.5	-
		16	4	135	-	-
		18	4	145	0.5	-
3	2	203	6	120	-	-
		194	15	130	-	-
		193	11	125	-	-
		193	8	125	-	-
		188	10	140	-	-
		193	5	130	-	-
		195	14	135	-	-
3	3	194	14	160	0.5	-
		200	6	145	2	-
		192	5	120	1	-
3	4	202	14	140		-
		198	15	130	2.5	-
		201	14	135	-	-
		20	4	135	3	-
		25	4	138	-	-
		21	2	115	3.5	-
		21	3	118	-	-
		20	5	120	3	-
		22	7	135	-	-
		14	6	140	1	-
		14	5	150	0.5	-
6	1	212	10	180	-	-
		206	4	180	-	-
		211	4	130	-	-
		208	7	130	-	-
		208	6	160	-	-
		204	11	140	-	-
		205	16	135	-	-
		200	17	145	-	-
		202	16	160	-	-
6	2	202	11	160	-	-
		208	8	140	-	-
		206	16	120	-	-
		214	10	110	-	-
		212	9	120	-	-
		218	0	115	-	-
		30	3	125	-	-
		34	9	130	-	-

LOC	FOLD ID	TREND	PLUNGE	ANGLE	AMP(CM)	WL(CM)
		214	4	130	-	-
		212	9	115	-	-
		220	4	120	-	-
		225	6	135	-	-
		220	4	125	-	-
		221	3	120	-	-
		222	2	125	-	-
		220	9	125	-	-
		211	5	135	-	-
		212	2	140	-	-
		210	19	150	-	-
6	3	205	23	0.5	-	-
		199	24	1	-	-
		200	20	0.5	-	-
6	4	212	5	170	-	-
		212	5	125	-	-
		216	4	115	-	-
		210	4	95	-	-
		210	6	100	-	-
		222	0	110	-	-
		220	4	105	-	-
		228	14	120	-	-
7 A	1	186	10	85	1	-
		192	9	85	1.5	-
		199	10	75	2	-
		199	15	105	2	-
		199	16	110	1.5	-
		194	14	110	1.5	-
		189	9	130	1.5	-
		193	15	113	1.5	-
		196	10	125	2	-
		205	15	110	2	-
		199	10	135	2.5	-
		200	14	128	2.5	-
		205	15	135	2	-
		205	3	140	2	-
		191	25	145	2	-
		194	22	160		-
7 A	2	192	4	130	0.5	-
		195	15	125	3.5	-

LOC	FOLD ID	TREND	PLUNGE	ANGLE	AMP(CM)	WL(CM)
		200	17	125	3	-
		198	22	128	3	-
		190	27	135	2.5	-
		195	30	15	2	-
		202	27	160	1	-
7 A	3	202	14	125	1	-
		205	16	125	3	-
		205	18	130	3.5	-
		213	18	120	3	-
		208	20	125	3.5	-
		208	16	125	2.3	-
		210	15	120	1.8	-
		208	10	150	1.5	-
		206	8	150	1.5	-
		205	14	150	1.5	-
		212	14	60	0.5	-
		212	15	60	1	-
		212	11	50	1	-
8 A	1	199	9	110	-	-
		205	6	105	-	-
		202	5	100	-	-
		206	7	110	-	-
		202	5	110	-	-
		206	0	105	-	-
		30	5	105	-	-
		30	4	115	-	-
		30	6	120	-	-
		28	0	110	-	-
		25	9	110	-	-
		31	13	130	-	-
		32	10	140	-	-
		34	12	150	-	-
		33	14	155	-	-
		30	10	155	-	-
		22	3	145	-	-
		22	0	145	-	-
		204	2	-	-	-
		198	0	-	-	-
		198	2	-	-	-
		20	10	-	-	-
		20	9	155	-	-

LOC	FOLD ID	TREND	PLUNGE	ANGLE	AMP(CM)	WL(CM)
		198	6	160	-	-
8 A	2	210	0	85	-	-
		36	2	85	-	-
		38	4	95	-	-
		36	4	85	-	-
		30	6	85	-	-
		35	0	65	-	-
		210	4	68	-	-
		200	6	80	-	-
		200	6	75	-	-
		198	1	7	-	-
		194	9	75	-	-
		194	1	8	-	-
		192	9	84	-	-
		189	10	90	-	-
		194	14	90	-	-
		194	9	85	-	-
		192	9	85	-	-
		189	14	75	-	-
		186	14	70	-	-
		190	11	85	-	-
8 A	3A	22	34	-	-	-
		34	20	80	-	-
		221	5	85	6	-
		203	5	80	-	-
		210	2	-	-	-
		203	9	90	-	-
		209	4	85	-	-
		205	4	90	-	-
		201	5	100	-	-
		205	0	120	-	-
		200	4	130	-	-
		200	5	130	10	
		205	3	150	-	-
		205	3	130	-	-
8 A	3B	210	4	125	-	-
		210	5	130	-	-
		220	2	130	8	-
		220	0	135	7	-
		216	4	125	7	-
		209	6	95	6	-
		216	9	95	5	-

LOC	FOLD ID	TREND	PLUNGE	ANGLE	AMP(CM)	WL(CM)
		228	11	93	2	
		226	15	90	2	-
		222	10	130	3	-
		222	3	130	3	-
		234	2	85	1	-
		236	0	90	1	-
8 A	3C	213	6	115	2	-
		228	5	95	3	-
		209	12	95	3	-
		216	6	160	0.5	-
8 A	4	198	10	140	1	
		191	10	140	1	-
		195	6	125	1.5	-
		201	6	125	2	-
		202	9	130	2	-
		202	9	140	1.5	-
		204	4	145	1.5	-
		205	0	135	1	-
		20	5	110	1	-
		191	0	115	0.5	-
8 A	5	350	19	123	2	-
		5	10	98	3	-
		5	5	95	3	-
		5	9	85	5	-
		5	9	90	6	-
		10	7	90	6	-
		10	10	95	-	-
		10	0	95	8	-
		10	3	110	-	-
		15	3	112	-	-
		12	0	125	-	-
		10	2	125	-	-
		12	2	130	-	-
8B		20	5	70	0.5	1
		21	2	85	1	1.5
		32	7	120	2	5.5
		32	10	120	5	6
		32	6	95	7	7
		24	14	100	7	6
		30	15	90	7	8

LOC	FOLD ID	TREND	PLUNGE	ANGLE	AMP(CM)	WL(CM)
		28	15	100	6	8
		28	12	110	5	8
		31	6	100	6	7
		31	0	95	6	7
		218	6	90	7	8
		210	2	125	3	5
8C	1	182	12	85	1	-
		170	10	85	2	-
		194	2	95	3	-
		202	3	130	0.5	-
		210	5	125	-	-
		211	2	75	5	-
		184	11	85	-	-
		170	20	95	8	-
		185	15	100	-	-
		189	10	95	-	-
		194	5	75	-	-
		195	5	70	5	-
		200	9	90	-	-
		205	2	90	-	-
		210	0	90	-	-
8C	2	228	5	105	4	-
		240	25	105	4	-
		240	16	110	3	-
		245	11	1	-	-
8D		240	6	100	2	6
		214	16	110	4	6
		225	25	90	3	-
		227	11	95	4	-
		232	6	115	3	8
		54	2	95	4	9
		46	5	85	4	9
		45	5	90	3	9
		228	0	85	3	7
		220	0	115	2	4
		222	5	130	1.5	6
		212	16	120	2	9
		205	15	125	2	1
		208	19	130	2	1
8E	1	358	25	115	-	8
		204	2	100	7	6

LOC	FOLD ID	TREND	PLUNGE	ANGLE	AMP(CM)	WL(CM)
		198	34	110	7	6
		195	38	115	4	7
		198	28	105	4	8
		202	20	105	6	8
		199	24	100	-	-
		220	24	130	-	-
		204	24	135	7	10
		204	10	135	9	10
		204	10	120	9	9
		200	9	115	5	5
		190	5	115	4	4
		18	7	110	4	4
		26	7	115	3	5
		26	4	115	2	6
		22	6	110	2	6
		18	9	120	1	6
8E	2	212	19	-	-	-
		199	19	135	4	12
		199	12	125	2	12
		205	12	145	1	10
		190	19	150	0.5	10
		195	5	150	0.5	10
		191	24	148	0.5	9
		216	14	135	1	8
		221	4	140	1	8
		20	5	145	1	10
		40	9	153	3	14
		21	19	150	2	16
8E	3	190	4	135	1	2
		176	12	130	1	4
		161	14	130	1	5
		154	20	130	1	6
		160	21	150	0.5	6
8F	1	211	14	135	-	3
		214	25	120	-	5
		212	36	115	-	7
		191	36	120	-	2
		195	41	130	-	19
		196	36	125	-	19
		224	28	130	-	17
		230	21	130	-	16

LOC	FOLD ID	TREND	PLUNGE	ANGLE	AMP(CM)	WL(CM)
		215	25	130	-	15
		218	25	135	-	15
		214	21	160	-	14
8F	2	203	15	155	-	13
		205	18	140	-	13
		202	16	125	-	14
		205	18	130	-	14
		200	14	130	-	14
		205	14	125	-	14
		206	16	120	-	15
		209	20	120	-	14
		210	16	120	-	13
		210	15	130	-	12
		215	14	155	-	12
		210	19	150	-	10
		216	19	170	-	10
8F	3	205	26	85	2	5
		202	25	-	3	5
		198	32	-	5	6
		186	27	-	7	6
		200	22	-	9	7
		207	15	-	9	6.5
		216	15	-	8	7
		222	10	-	7	5
		228	6	-	5	3
8F	4	192	24	160	-	13
		180	16	160	-	12
		176	18	155	1	18
		180	24	160	2	18
		180	24	165	-	16
8F	5	204	31	155	-	28
		208	25	145	-	27
		216	20	130	-	20
		216	20	130	-	19
8G	1	198	6	155	1	-
		16	6	150	1	-
		16	2	145	-	-
		20	0	140	20	-
		204	11	115	-	-
		210	20	110	-	-
		211	20	110	26	-

LOC	FOLD ID	TREND	PLUNGE	ANGLE	AMP(CM)	WL(CM)
		210	20	115	-	-
		211	19	120	-	-
		215	17	105	-	-
		212	18	110	12	-
		220	14	90	-	-
		222	19	95	-	-
		224	20	90	5	-
		226	11	100	-	-
		226	6	110	-	-
		230	0	115	2	-
8G	3	224	20	110	2	-
		215	14	125	2	-
		210	9	130	1	-
		206	6	140	1	-
		203	4	155	0.5	-
		200	6	160	0.5	-
8G	2	182	16	155	-	7.5
		184	22	145	-	5.5
		186	19	145	-	3
		191	15	150	-	2
9A		198	19	170	1	11
		200	19	155	2	13
		198	24	155	2.5	13
		194	23	145	3	11
		195	20	135	4.5	13
		190	15	125	4.5	15
		192	13	135	5	14
		199	13	115	4	15
		198	19	110	4	14
		202	15	110	4	18
		209	13	110	5	20
		204	11	100	5	21
		203	21	95	5.5	25
		201	18	105	6	26
		203	11	115	7	26
		200	20	110	7	26
		201	16	130	6	27
		204	21	135	6	27
		207	16	120	5	27
		221	18	120	5	27
		201	20	125	4	27

LOC	FOLD ID	TREND	PLUNGE	ANGLE	AMP(CM)	WL(CM)
		214	24	130	4	27
		214	24	130	4	27
		212	22	135	4	27
		214	18	135	4	27
		224	16	135	4	27
		219	21	135	4	30
		223	19	135	4	19
		219	19	140	2	13
		219	14	145	1	11
		215	15	155	2	9
		215	16	155	2	8
9B	2	199	19	105	12	40
		200	23	110	-	-
		200	21	105	10	-
		202	20	125	-	-
		204	20	140	3	25
		202	19	105	4	-
		199	25	125	5	22
		204	20	125	6	-
		210	14	105	6	20
		205	16	110	6	-
		205	16	108	6	14
		205	20	105	6	12
		206	16	115	4	10
		212	16	105	4	8
		212	14	100	2	8
		208	4	140	1	5
9B	3	185	9	170	1	4
		192	5	125	3	5
		194	10	125	3	6
		194	9	130	3	7
		198	6	160	4	7
		195	3	150	4.5	8
		189	8	130	4	9
		190	8	130	5	10
		194	10	120	7	9
		194	10	115	7	10
		196	10	115	9	10
		194	14	110	8	9
		199	14	85	8	9
		201	13	90	8	9

LOC	FOLD ID	TREND	PLUNGE	ANGLE	AMP(CM)	WL(CM)
		207	6	110	6	8
		200	19	130	4	12
		199	16	120	4	11
		198	15	135	3	9
		203	19	115	2	8
		204	17	140	2	8
		205	14	100	1	6
9C	1	189	9	70	0.5	0.5
		180	10	75	1	5
		186	9	120	1	6
		202	4	125	1.5	6.5
		208	2	130	1	5
		204	10	135	1	3
		203	10	140	0.5	2
9C	2	185	11	120	1	3
		189	16	90	1	2
		195	16	130	1	2
		210	9	135	1	3
9C	3	210	4	145	1	8
		210	2	145	2	9
		212	2	140	2	6
		214	4	140	1.5	5
		206	11	150	1	4
9D	1	15	4	120	1	4.5
		195	2	155	1	4
		190	0	145	1	3.5
		190	0	135	1	4
		191	2	135	1	4
		191	0	155	2	3
		6	4	135	2	3
		15	2	140	1	5
		200	15	150	1	4
9D	2	18	6	145	2	12
		20	4	145	2.5	11
		24	6	150	3	10
		18	4	135	3	9
		20	3	135	3	8
		22	4	140	2	8
		23	9	140	1	6
		16	2	140	1	5

LOC	FOLD ID	TREND	PLUNGE	ANGLE	AMP(CM)	WL(CM)
9D	3	180	6	145	0.5	4
		190	6	150	1	5
		192	7	170	0.5	4
9D	4	186	7	170	0.5	2
		188	7	150	1	5
		198	9	160	1	5
		200	5	170	0.5	2
9E	1	196	10	-	-	-
		200	14	-	-	-
		199	16	-	-	-
		204	16	-	-	-
		204	16	-	-	-
		206	16	-	-	-
		200	10	-	-	-
		202	16	-	-	-
		200	12	-	-	-
		210	6	-	-	-
		210	6	-	-	-
		210	10	-	-	-
		208	14	-	-	-
		208	18	-	-	-
		210	16	-	-	-
		218	20	-	-	-
		225	30	-	-	-
		225	22	-	-	-
		208	12	-	-	-
		202	12	-	-	-
		195	16	-	-	-
		200	14	-	-	-
9E	2	195	16	-	-	-
		195	12	-	-	-
		200	11	-	-	-
		194	11	-	-	-
		191	14	-	-	-
		192	12	-	-	-
		186	14	-	-	-
		187	14	-	-	-
		187	8	-	-	-
		185	5	-	-	-
		180	5	-	-	-
		170	0	-	-	-

LOC	FOLD ID	TREND	PLUNGE	ANGLE	AMP(CM)	WL(CM)
		152	5	-	-	-
		160	10	-	-	-
		158	10	-	-	-
		158	10	-	-	-
		162	10	-	-	-
		164	10	-	-	-
10.A	1	225	25	115	3	9
		220	4	100	3	9.5
		219	9	110	3	9
		220	8	105	3	9.5
		222	10	120	3	9.5
		220	14	115	3	8
		219	15	115	3	8
		218	9	125	2.5	8
		38	0	115	2	7
		37	4	125	2	4
		35	0	125	1	3
		214	4	125	1	1.5
		214	4	135	1	2
10.B		210	15	160	4	1
		197	11	145	5	2
		200	17	100	9	8
		201	22	900	9	8
		202	22	115	10	8
		206	25	100	11	8
		206	24	100	10	7.5
		208	10	100	9	10
		210	9	100	13	9
		212	13	110	13	11
10.C		174	10	170	1	-
		185	0	105	2	-
		6	2	95	2	-
		191	0	95	2	-
		21	4	90	1.5	-
10.D		209	16	155	50	-
		205	12	135	-	-
		205	12	130	-	-
		204	10	125	-	-
		205	11	115	-	-
		209	9	100	35	-
		216	3	85	-	-

LOC	FOLD ID	TREND	PLUNGE	ANGLE	AMP(CM)	WL(CM)
		215	0	80	-	-
		215	4	75	-	-
		218	11	90	-	-
		214	9	85	-	-
		212	24	85	45	-
		210	20	80	-	-
		212	25		-	-
		210	14		30	-
		210	9		-	-
		206	19	130	-	-
		210	6	140	-	-
		210	6	140	-	-
		205	9	120	10	-
		205	18	135	-	-
		200	20	140	-	-
		209	4	135	-	-
		210	9	135	-	-
		200	26	145	30	-
		205	6	140	-	-
		210	5	130	-	-
		205	5	125	-	-
		214	6	95	-	-
		219	4	90	-	-
		215	3	105	-	-
		215	8	115	40	-
		218	2	120	-	-
		220	2	115	-	-
		220	2	110	-	-
		223	0	120	-	-
		218	6	130	38	-
		225	9	125	-	-
		235	9	125	-	-
		230	2	130	-	-
		230	4	150	-	-
		230	2	160	28	-
11	1	220	19	160	-	-
		222	16	130	-	-
		225	19	120	-	-
		226	24	115	-	-
		227	23	105	-	-
		232	19	110	-	8

LOC	FOLD ID	TREND	PLUNGE	ANGLE	AMP(CM)	WL(CM)
		228	9	105	-	8
		220	19	115	-	8
		227	19	115	-	7
		228	20	115	-	7
		228	19	120	-	7
		228	9	125	-	6
		232	8	130	-	7
		235	14	140	-	8
		240	14	150	-	9
		240	9	140	-	9
		235	8	140	-	10
		240	15	130	-	10
		236	20	140	-	10
		235	19	140	-	11
		235	15	140	-	11
11	2	224	25	130	-	-
		226	23	130	-	-
		223	15	110	-	-
		221	15	120	-	-
		220	19	120	-	-
		222	12	160	-	-
		225	9	145	-	-
		220	20	145	-	-
		228	15	145	-	-
		229	17	150	-	-
		230	18	160	-	-
		231	15	170	-	-
11	3	220	16	150	1	2
		220	20	150	1	3.5
		225	21	160	1	4
		225	21	170	1	4
11	4	208	23	170	-	7
		220	18	160	-	9
		225	15	150	-	8.5
		225	16	160	-	8
		228	14	175	-	8
14	1	186	6	155	18	25
		184	6	155	18	25
		183	4	140	18	25
		183	4	130	18	25
		183	5	115	18	25

LOC	FOLD ID	TREND	PLUNGE	ANGLE	AMP(CM)	WL(CM)
		186	9	110	18	25
		186	9	95	18	25
		191	5	95	18	25
		191	7	90	14	25
		195	10	85	14	20
		190	14	85	14	20
		194	14	80	8	18
		195	9	80	12	18
		197	10	80	12	16
		197	10	95	12	15
		195	12	110	9	15
		198	10	120	8	15
		198	11	120	6	11
		201	5	120	6	9
		200	10	130	4	8
		191	2	140	2	7
		192	5	145	1	6
		190	10	160	1	5
		190	10	175	1	5
14A	2	174	15	155	2	15
		169	11	140	5	15
		7	16	0	6	15
		4	17	110	7	13
		7	7	110	6	12
		3	7	105	5	12
		5	10	100	5	12
		0	15	100	5	12
		7	2	110	4	12
		11	4	120	2	11
14A	4	189	4	120	1	10
		189	6	120	1.5	11
		189	5	100	3	12
		189	5	90	3.5	12
		190	11	85	4	12
		191	11	80	3	12
		199	19	105	2.5	10
		202	20	135	2.5	10
14B		195	15	130	8	-
		195	20	120	5	-
		214	5	120	5	-
		209	10	145	3	-

LOC	FOLD ID	TREND	PLUNGE	ANGLE	AMP(CM)	WL(CM)
		202	15	150	3	-
		199	12	150	2	-
		191	11	160	1	-
		192	11	170	0.5	-
		191	9	170	0.5	-
		191	6	170	0.5	-

Bibliography

Alvarez-Marron, J. & Perez-Estaun, A. 1988. Thin skinned tectonics in the Ponga region (Cantabrian Zone, NW Spain). *Geologische Rundschau* **77**, 539-550.

Alvarez-Marron, J. 1995. Three-dimensional geometry and interference of fault-bend folds: examples from the Ponga Unit, Variscan Belt, NW Spain. *J. Struct. Geol.* **17**, 549-560.

Anhaeusser, C.R. 1975. Precambrian tectonic environments. *An. Rev. Earth & Planetary Sci.* **3**, 31-54.

Anhausser, C.R. 1984. Structural elements of Archaen granite-greenstone terranes as exemplified by the Barberton Mountain Land, southern Africa. In: Kroner, A. & Greiling, R. (eds.) *Precambrian Tectonics Illustrated*, Schweizerbart'sche Verlagsbuchandlung, Germany, 57-78.

Apotria, T.G., Snedden, W.T., Spang, J.H., & Wiltschko, D.V. 1992. Kinematic models of deformation at an oblique ramp. In: McClay, K. (ed.) *Thrust Tectonics*. Chapman and Hall, London.

Blay, P., Cosgrove J.W., & Summers, J.M. 1977. An experimental investigation of the development of structures in multilayers under the influence of gravity. *J. Geo. Soc. London* **133**, 329-342.

Braun, J. 1993. Three-dimensional numerical modeling of compressional orogenies: thrust geometry and oblique convergence. *Geology* **21**, 153-156.

Burks, R.J. 1981. Alleghenian deformation and metamorphism in southwestern Narragansett Basin, Rhode Island. Unpublished M.S., University of Texas, Austin, Texas.

Burks, R.J. 1985. Incremental and finite strains within ductile shear zones, Narragansett Basin, Rhode Island. Unpublished Ph.D., University of Texas, Austin, Texas.

Campbell, J.D. En echelon folding. *Economic Geology* **53**, 448-472.

Carter, N. 1976. Steady state flow of rocks. *Rev. Geophys. Space Phys.* **14,** 301-360.

Cazier, E.C. 1987. Late Paleozoic tectonic evolution of the Norfolk Basin, southeastern massachusetts. *J. Geology* **95**, 55-73.

Cobbold, P.R. 1976. Fold shapes as functions of progressive strain. *Phil. Trans. Roy. Soc. London* **A283**, 129-138.

Cobbold, P.R., Cosgrove, J., & Summers, J.M. 1971. Development of internal structures in deformed anisotropic rocks. *Tectonophysics* **12**, 23-53.

Cogswell, J. & Mosher, S. 1994. Late stage Alleghanian wrenching of the southewestern Narragansett Basin, Rhode Island. *Am. J. Sci.* **294**, 861-901.

Colletta, B., Letouzey, J. Pinedo, R., Ballard, J.F. & Bale, P. 1991. Computerized X-ray tomography analysis of sandbox models: examples of thin-skinned thrust systems. *Geology* **19**, 1063-1067.

Davidson, A. 1984. Identification of ductile shear zones in the southwestern Grenville Province of the Canadian Shield. *In*: A. Kroner and R. Greiling (eds.), *Precambrian Tectonics Illustrated*. E. Schweizerbartsche Verlagsbuchhandlung, Stuttgart.

Davis, D., Suppe, J. and Dahlen, F. 1983. Mechanics of Fold-and-Thrust Belts and Accretionary Wedges. *J. Geophys. Res.* **88B2**, 1153-1172.

de Lamotte, D.F., Guezou, J.C., and Averbuch, O. 1995. Distinguishing lateral folds in thrust-systems; examples from Corbieres (SW France) and Betic Cordilleras (SE Spain). *J. Struct. Geol.***17**, 233-244.

de Ronde, C.E. & de Wit, M.J. 1994. Tectonic history of the Barberton greenstone belt, South Africa: 490 million years of Archean crustal evolution. *Tectonics* **13**, 983-1005.

de Sitter, L.U. 1952. Plissement croise dans let Haut-Atlas. *Geol. Mijnbouw* **14**, 277-282.

Dewey, J. 1965. Nature and origin of kink-bands. *Tectonophysics* **1**, 459-494.

Dixon, J. & Summers, J. 1985. Recent developments in centrifuge modelling of tectonic processes: Equipment, model construction techniques and rheology of model materials. *J. Struct. Geol.* **7**, 83-102.

Dreier, R.B. 1985. The Blackstone series: Evidence for Precambrian Avalonian and Permian Alleghanian Tectonism in Southeastern New England. Unpublished Ph.D., University of Texas, Austin, Texas.

Dubey, A.K. & Cobbold, P.R. 1977. Noncylindrical flexural slip folds in nature and experiment. *Tectonophysics* **38**, 223-239.

Dubey, A.K. 1984. Superimposed buckle folding in multilayers: Interference patterns and simultaneous development with transcurrent faults. *Geoscience Journal* **5**, 59-72.

Elliott, D. 1983. The construction of balanced cross-sections. *J. Struct. Geol.* **5**, 101.

Farrens, C.M. 1982. Styles of deformation in the southeastern Narragansett Basin, Rhode Island and Massachusetts. Unpublished M.S., University of Texas, Austin, Texas.

Fisher, N.I., Lewis, T., Embleton, B.J.J. 1987. *Statistical analysis of spherical data.* London: Cambridge University Press. 329 p.

Fletcher, R.C. 1991. Three-dimensional folding of an embedded viscous layer in pure shear. *J. Struct. Geol* . **13**, 87-96.

Flinn, D. 1962. On folding during three-dimensional progressive deformation. *Geol.Soc. Lon.Quart.J.* **118**, 385-433.

Fowler, T.J. 1989. Superposed folding in the Rockley district, Lachlan Fold Belt, New South Wales. *Australian J. of Earth Sci.* **36**, 451-468.

Geiser, P.A. 1988. The role of kinematics in the construction and analysis of geological cross sections in deformed terranes. In: Mitra, G. and Wojtal, S., (eds.) Geometries and mechanisms of thrusting, with special reference to the Appalachians. *Geol.Soci.of America Sp. Paper* **222**, 47-76.

Ghosh , S.K. & Ramberg, H. 1968. Buckling experiments on intersecting fold patterns. *Tectonophysics* **5**, 89-105.

Ghosh, S.K. & Sengupta, S. 1984. Successive development of noncylindrical folds in progressive deformation. *J. Struct. Geol.* **6**, 703-709.

Ghosh, S.K. 1970. A theoretical study of intersecting fold patterns. *Tectonophysics* **9**, 559-569.

Ghosh, S.K. 1974. Strain distribution in superposed buckling folds and the problem of reorientation of early lineations. *Tectonophysics* **21**, 249-272.

Ghosh, S.K., Mandal, N, Sengupta, S., Deb, S. & Khan, D. 1992. Modes of superposed buckling in single layers controlled by initial tightness of early folds. *J. Struct. Geol.* **14**, 381-394.

Ghosh, S.K., Mandal, N, Sengupta, S., Deb, S. & Khan, D. 1993. Superposed buckling in multilayers. *J. Struct. Geol.* **15**, 95-111.

Glen, R.A. 1990. Formation and inversion of transtensional basins in the western part of the Lachan Fold Belt, Australia, with emphasis on the Cobar Basin. *J. Struct. Geol.* **12,** 601-620.

Gratier, J.P., Guillier, B., Delorme, A., & Odonne, F. 1991. Restoration and balance of a folded and faulted surface by best-fitting of finite elements: principle and applications. *J. Struct. Geol.* **13**, 111-115.

Grujic, D. 1993. The influence of initial fold geometry on Type 1 and Type 2 interference patterns: an experimental approach. *J. Struct. Geol.* **15**, 293-307.

Guterman, V.G. 1981. Model studies of gravitational gliding tectonics. *Tectonophysics* **65**, 111-126.

Harrison, J.C., Fox, F.G. & Okulitch, A.V. 1991. Late-Devonian - Early Carboniferous deformation of the Parry Islands and Canrobert Hills fold belts, Bathurst and Melville islands, *In* Ch. 12 of *Geology of the Innuitian Orogen and Arctic Platform of Canada and Greenland*, H.P. Trettin (ed.) Geological Society of America, The Geology of North America, v.E.

Henderson, C. M. & Mosher, S. 1983. Narragansett Basin, RI: Role of intrabasinal horsts and grabens in Alleghanian Deformation. *Geol. Soc. Am. Abst. with Programs* **15**, 129.

Hermes, O.D., Gromet, L.P., Murray, D.P., (compilers), Skehan, J.W., and Mosher S. (major contributors). 1994. Bedrock Geologic Map of Rhode Island, Rhode Island Map Series No. 1.

Honea, E. & Johnson, A. 1976. A theory of concentric, kink and sinusoidal folding and of nonoclinical flexuring of compressible, elastic multilayers. *Tectonophysics* **30**, 197-239.

Hubbert., M. King, 1937. Theory of scale models as applied to the study of geologic structures. *Bull. Geol. Soc. Am.* **48**, 1459-1520.

Hudleston, P.J. 1973. The analysis and interpretation of minor folds developed in the Moine rocks of Monar, Scotland. *Tectonophysics* **17**, 89-132.

Hudleston, P.J. and Stephansson, O. 1973. Layer shortening and fold-shape development in the buckling of single layers. *Tectonophysics* **17**, 299-321.

Jackson, M.P.A., Talbot, C.J, & Cornelius, R.R. 1988. Centrifuge modeling of the effects of aggradation and progradation on syndepositional salt structures: *University of Texas at Austin Bureau of Economic Geology Report of Investigations* **173**, 93 p.

Julivert, M. & Marcos, A. 1973. Superimposed folding under flexural conditions in the Cantabrian Zone (Hercynian Cordillera, Northwest Spain). *Am. J. Sci.* **273**, 353-375.

Julivert, M. 1986. Aerial balancing and estimate of areal reduction in a thin-skinned fold and thrust belt (Cantabrian Zone, Northwest Spain). *J. Struct. Geol.* **8**, 407-414.

Kamb, W.B. 1959. Ice petrofabric observations from Blue Glacier, Washington, in relation to theory and experiment. *J. Geophys. Res.* **64**, 1891-1909.

Kano, K., Kosaka, K., Murata A., & Yani, S. 1990. Intra-arc deformations with vertical rotation axes: the case of the pre-Middle Miocene terranes of Southwest Japan. *Tectonophysics* **176**, 333-354.

Kerr, J.W. 1977. Cornwallis fold Belt and the mechanism of basement uplift. *Can. J. Earth. Sci.* **14,** 1374-1401.

Kveton, K.J. 1994. 3D geometry and kinematic development of a lateral ramp that links in and out-of sequence thrusts in the Absaroka Thrust System, WY. Geological Society of America 1994 Annual Meeting, *Abstracts with Programs*, **26**, 185.

Lan, L. & Hudleston, P. 1991. Finite-element models of buckle folds in non-linear materials. *Tectonophysics* **199**, 1-12.

Lisle, R.J., Styles, P. & S.J. Freeth. 1990. Fold interference structures: the influence of layer competence contrast. *Tectonophysics* **172**, 197-200.

Marques, F.G. & Cobbold, P.R. 1995. Development of highly non-cylindrical folds around rigid ellipsoidal inclusions in bulk simple shear regimes: natural examples and experimental modelling. *J. Struct. Geol.* **17**, 589-602.

Marshak, S. & Tabor, J. 1989. Structure of the Kingston orocline in the Appalachian fold-thrust belt, New York. *Bull. Geol. Soc. Am.* **101**. 683-701.

Marshak, S. Wilkerson, M.S. & Hsui, A.T. 1992. Generation of curved fold-thrust belts: Insight from simple physical and analytical models. In: McClay, K. (ed.) *Thrust Tectonics*. Chapman and Hall, London.

McClay, K. R. 1976. The rheology of plasticine. *Tectonophysics* **33**, T7-T15.

McCoss, A.M. 1988. Restoration of transpression/transtension by generating the three-dimensional segmented helical loci of deformed lines across structure contour maps. *J. Struct. Geo.* **10**, 109-120.

McDonough, M.R. & Simony P.S. 1989. Valemount strain zone: A dextral oblique-slip thrust system linking the Rocky Mountain and Omineca belts of the southeastern Canadian Cordillera. *Geology* **17**, 237-240.

Mosher, S. & Berryhill, A. 1991. Structural analysis of progressive deformation within complex transcurrent shear zone systems: southern Narragansett Basin, Rhode Island. *J. Struct. Geol.* **13**, 1991.

Mosher, S. & Helper, M.A. 1988 Interpretation of polydeformed terranes. Chapter 16 in *Basic Methods of Structural Geology*, Marshak, S. and Mitra, G. (eds.) Prentice-Hall, 361-384.

Mosher, S. 1978. Pressure solution as a deformation mechanism for the Purgatory Conglomerate, Rhode Island. Unpublished Ph. D., University of Illinois, Urbana, Illinois.

Mosher, S. 1983. Kinematic history of the Narragansett Basin, Massachusetts and Rhode Island: Constraints on late Paleozoic plate reconstructions. *Tectonics* **2**, 327-244.

Neurath, C. & Smith, R.B 1982. The effect of material properties on growth rates of folding and boudinage: experiments with wax models. *J. Struct. Geol.* **4**, 215-229.

O'Driscoll , E.S. 1964. Interference patterns from inclined shear fold systems. *Bull. Cana. petr. geol.* **12**, 279-310.

O'Driscoll, E.S. 1962. Experimental patterns in superposed similar folding. *J. Alberta Soc. Pet. Geol.* **10**, 145-167.

Odonne, F. & Vialon, P. 1987. Hinge migration as a mechanism of superimposed folding. *J. Struct. Geol.* **9**, 835-844.

Okulitch, A.V., & Trettin, H.P. 1991. Late Cretaceous - Early Tertiary deformation, Arctic Islands; Chapter 17 In: *Geology of the Innuitian Orogen and Arctic Platform of Canada and Greenland,* H.P. Trettin (ed.) Geological Society of America, The Geology of North America v.E.

Okulitch, A.V., Packard, J.J. & Zolnai, A.I. 1991. Late Silurian - Early Devonian deformation of the Boothia Uplift. In: Chapter 12 of *Geology of the Innuitian Orogen and Arctic Platform of Canada and Greenland,* H.P. Trettin (ed.) Geological Society of America, The Geology of North America v.E.

Pares, J.M., Van der Voo, R., Stamatakos, J., Perez-Estaun, A. 1994. Remagnetizations and postfolding oroclinal rotations in the Canabrian/Asturian arc, northern Spain. *Tectonics* **13**, 1461-1471.

Parrish, D.K., Krivz, A. & Carter, N.L. 1976. Finite-element folds of similar geometry. *Tectonophysics* **32**, 183-207.

Perez-Estaun, A., Bastida, F., Alonso, J., Marquinez, J., Aller, J., Alvarez-Marron, J., Marcos, A. & Pulgar, J. 1988. A thin-skinned tectonics model for an arcuate fold and thrust belt: The Cantabrian zone (Variscan Ibero-Amorican Arc). *Tectonics* **7**, 517-537.

Perrin, M., Oltra, P., & S. Coquillart. 1988. Progress in the study and modelling of similar fold interferences. *J. Struct. Geol.* **10**, 593-605.

Pfiffner, O.A. & Ramsay, J.G. 1982. Constraints on geological strain rates: arguments from finite strain states of naturally deformed rocks. *J. geophys. Res.* **87**, 311-321.

Powell, C. McA. 1984. Terminal fold-belt deformation: Relationship of mid-Carboniferous megakinks in the Tasman fold belt to coeval thrusts in cratonic Australia. *Geology* **12**, 546-549.

Powell, C.McA., Cole, J.P, & Cudahy, T.J. 1985. Megakinking in the Lachlan Fold Belt, Australia. *J. Struct. Geol.* **7**, 281-300.

Raj, S. 1984. Study of interference patterns produced by fold superposition at moderate and high angles to the early fold trend in model experiments and their application to analogous structures in a lesser Himalayan terrain in Simla hills. *Geosciences J.* **5**, 25-34.

Ramberg, H. 1959. Evolution of ptygmatic folding. *Norsk Geologisk Tidsskrift* **39**, 99-152.

Ramberg, H. 1964. Selective buckling of composite layers with contrasted rheological properties; a theory for simultaneous formation of several orders of folds. *Tectonophysics* **1**, 307-341.

Ramberg, H. 1967. *Gravity, Deformation and the Earth's Crust; as Studied by Centrifuge Models*. Academic Press, London.

Ramberg, H. 1970. Folding of laterally compressed multilayers in the field of gravity, I. *Physics of Earth and Planetary Interiors* **2**, 203-232.

Ramberg, H. 1981. *Gravity, Deformation and the Earth's Crust.* Second edition. Academic Press, London.

Ramsay, J. G. 1967. *The Folding and Fracturing of Rocks*. McGraw-Hill, New York.

Ramsay, J.G. 1962. Interference patterns produced by the superposition of folds of similar type. *J. Geol.* **60**, 466-481.

Ramsay, J.G. 1965. Structural investigations in the Barberton Mountain Land, Eastern Transvaal. *Trans. Geol. Soc. S. Africa* **66**, 353-401.

Reck, B. & Mosher, S. 1987. Timing of intrusion of the Narragansett Pier Granite relative to deformation in the southwestern Narragansett Basin, Rhode Island. *J. Geology* **96**, 677-692.

Reynolds, D.L. & Holmes, A. 1954. The superposition of Caledonoid folds on an older fold-system in the Dalradians of Malin Head, Co. Donegal. *Geol. Mag.* **91**, 417-433.

Rixon, , L., Bucknell, W.R., & Rickard, M.J. 1983. Megakink folds and related structures in the Upper Devonian Merrimbula Group, South Coast, N.S.W. *J. Geol. Soc. Aust.* **30**, 277-293.

Rouby, D., Cobbold, P.R. Szatmari, P., Demercian, S., Coelho D. & Rici, J.A. 1993. Least-squares palinspastic restoration of regions of normal faulting - apllication to the Campos basin (Brazil). *Tectonophysics* **221**, 439-452.

Rouby, D., Cobbold, P.R. Szatmari, P., Demercian, S., Coelho D. & Rici, J.A. 1993. Restoration in plan view of faulted Upper Cretaceous and Oligocene horizons and its bearing on the history of salt tectonics in the Campos Basin (Brazil). *Tectonophysics* **228**, 435-445.

Scheidegger, A.E. 1965. On the statistics of the orientation of bedding planes, grain axes, and similar sedimentological data. *U.S.G.S. Prof. Paper* **525-C**, 164-167.

Schultz-Ela, D. 1988. Application of a three-dimensional finite-element method to strain field analyses. *J. Struct. Geo.* **10**, 263-272.

Schwerdtner, W.M, Torrance, J.G. & van Berkel, J.T. 1989. Pattern of apparent total strain in the bedded anhydrite cap of a folded salt wall. *Can. J. Earth Sci.* **26**, 983-992.

Schwerdtner, W.M. & van Berkel, J.T. 1991. The origin of fold abutments in the map pattern of the westernmost Grenville Province, central Ontario. *Precambrian Res.* **49**, 39-59.

Skehan, J.W., Rast, N. & Mosher, S. 1986. Paleoenvironmental and tectonic controls of sedimentation in coal-forming basins of southeastern New England. In: Lyons, P.C. & Rice, C.L. (eds.) Paleoenvironmental and Tectonic controls in Coal-Forming Basins of the United States. *Geological Soc. Am. Special Paper* **210**, 9-30.

Skjernaa, L. 1975. Experiments on superimposed buckle folding. *Tectonophysics* **27**, 255-270.

Smith, J.V. & Marshall, B. Patterns of folding and fold interference in oblique contraction of layered rocks of the inverted Cobar Basin, Australia. *Tectonophysics* **215**, 319-334.

Smith, R.B. 1977. Formation of folds, boudinage, and mullions in non-Newtonian materials. *Bull. Geol. Soc. Am.* **88**, 312-320.

Smith, R.B. 1979. The folding of a strongly non-Newtonian layer. *Am. J. Sci.* **279**, 272-287.

Snoke, A.W. & Mosher S. 1989. The Alleghanian Orogeny as manifested in the Appalachian internides. In: Hatcher, R.D, Thomas, W.A. & Viele, G.W. (eds.). The Appalachian-Ouachita orogen in the United States: Boulder, Colorado, G.S. A., The Geology of North America v. F-2, 288-318.

Stauffer, M. R. 1988. Fold interference structures and coaptation folds. *Tectonophysics* **149**, 339-343.

Stauffer, M.R. & Mukherjee, A. 1971. Superimposed deformations in the Missi Meta-sedimentary Rocks near Flin Flon, Manitoba. *Can. J. Earth Sci* **8**, 217-242.

Stewart, A.J. 1987. Fault reactivation and superimposed folding in a Proterozoic sandstone-volcanic sequence, Davenport Province, central Australia. *J. Struct. Geol.* **9**, 441-455.

Stewart, S.A. 1993. Fold interference structures in thrust systems. *Tectonophysics* **225**, 449-456.

Thiessen, R. 1986. Two-dimensional refold interference patterns. *J. Struct. Geol.* **8**, 563-573.

Thiessen, R.L. & Means, W.D. 1980. Classification of fold interference patterns: a re-examination. *J. Struct. Geol.* **2**, 311-326.

Thomas, K.J. 1981. Deformation and metamorphism in the central Narragansett Basin of Rhode Island. Unpublished M.S., University of Texas, Austin, Texas.

Treagus, J.E. & Treagus, S.H. 1981. Folds and the strain ellipsoid: a general model. *J. Struct. Geol* **3**, 1-17.

Tull, J.F. 1984. Polyphase late Palaeozoic deformation in the southeastern foreland and northwestern Piedmont of the Alabama Appalachians. *J. Struct. Geol.* **6**, 223-234.

Turcotte, D.L. & Schubert, G. 1982. *Geodynamics: Applications of Continuum Physics to Geological Problems*. John Wiley & Sons, New York.

van Berkel, J.T., Schwerdtner, W.M. & Torrance, J.G. 1984. Wall-and-basin structure: an intriguing tectonic prototype in the central Sverdrup Basin, Canadian Arctic Archipelago. *Bull. Can. Pet. Geol.* **32**, 343-358.

Von Winterfield & Oncken. 1995. Non-plane strain in section balancing: calculation of restoration parameters. *J. Struct. Geol.* **17**, 447-450.

Watkinson, A.J. 1981. Patterns of fold interference: influence of early fold shapes. *J. Struct. Geol.* **3**, 19-23.

Watkinson, A.J. & Thiessen, R.L. 1988. Geometric models of folding at Loch Monar, Scotland, using computer simulation. *Tectonophysics* **149**, 1-15.

Watkinson, A.J. and Cobbold, P.R. 1981. Axial directions of folds in rocks with linear/planar fabrics. *J. Struct. Geol.* **3**, 211-217.

Watson, G.S. 1966. The satistics of orientation data. *J. Geology* **74**, 786-797.

Weijermars, R. & Schmeling, H. 1986. Scaling of Newtonian and non-Newtonian fluid dynamics without inertia for quantitative modelling of rock flow due to gravity (including the concept of rheological similarity). *Physics of the Earth and Planetary Interiors* **43**, 316-330.

Weijermars, R. 1986. Flow behaviour and physical chemistry of bouncing putties and related polymers in view of tectonic laboratory applications. *Tectonophysics* **124**, 325-358.

Weiss, L.E. 1959. Geometry of superposed folding. *Bull. Geol. Soc. Am.* **70,** 91-106.

Wellington, S.L. & Vinegar, H.J. X-Ray computerized tomography. *J. Pet. Tech.* **39**, 885-898.

Wilcox, R.E., Harding T.P., & Seely, D.R. 1973. Basic Wrench Tectonics. *Bull. Am. Assoc. Pet. Geol.* **57**, 74-96.

Wilkerson, M., Marshak, S., & Bosworth, W. 1992. Computerized tomographic analysis of displacement trajectories and three-dimensional fold geometry above oblique thrust ramps. *Geology* **20**, 439-442.

Wilkerson, M., Medwedeff, D., & Marshak, S. 1991. Geometrical modeling of fault-related folds: a pseudo-three-dimensional approach. *J. Struct. Geol.* **13**, 801-812.

Williams, G.D. & Chapman, T.J. 1980. The geometrical classification of noncylindrical folds. *J. Struct. Geo.* **3**, 181-185.

Williams, P. F. 1985. Multiply deformed terrains - problems of correlation. *J. Struct. Geol.* **7**, 269-280.

Wintsch, R.P. & Sutter, J.F. 1986. A tectonic model for the Late Paleozoic of southeastern New England. *J. Geology*. **94**, 459-472.

Woodcock, N.H. & Naylor, M.A. 1983. Randomness testing in three-dimensional orientation data. *J. Struct. Geo.* **5**, 539-548.

Woodcock, N.H. 1977. Specification of fabric shapes using an eigenvalue method. *Bull. Geol. Soc. Am.* **88**, 1231-1236.

The vita has been removed from the digitized version of this document.